Department of Chemistry
Physical Chemistry

Tm^{3+}-doped $NaYF_4$ nanoparticles: upconversion properties and bioimaging

Doctoral thesis

in fulfilment of the requirements for the degree

"doctor rerum naturalium"
(Dr. rer. nat.)

in the scientific discipline "Physical Chemistry"

submitted to the

Faculty of Science

of the University of Potsdam

by

Anna López de Guereñu

Potsdam, 18. August 2020

Hauptbetreuer: Prof. Dr. Michael Kumke
Betreuer: Prof. Dr. Andreas Herrmann
Gutachter: Prof. Dr. Niko Hildebrandt

Published online on the
Publication Server of the University of Potsdam:
https://doi.org/10.25932/publishup-47559
https://nbn-resolving.org/urn:nbn:de:kobv:517-opus4-475593

Zusammenfassung

der Arbeit mit dem Titel:

Tm^{3+}-doped $NaYF_4$ nanoparticles: upconversion properties and bioimaging

eingereicht von Anna López de Guereñu, April 2020, an der Universität Potsdam.

In letzter Zeit hat sich die Integration von hochkonvertierenden Nanopartikeln (UCNP) in industriellen, biomedizinischen und wissenschaftlichen Anwendungen aufgrund der außergewöhnlichen photophysikalischen Eigenschaften, die UCNP bieten, zunehmend beschleunigt. Einige der vielversprechendsten Anwendungen liegen auf dem Gebiet der Medizin und des Bioimaging, der Bildgebung in biologischen Proben, unter anderem aufgrund vieler Vorteile wie einer tieferen Gewebedurchdringung, einem verringerten optischen Hintergrund, der Möglichkeit einer mehrfarbigen Bildgebung und einer geringeren Toxizität im Vergleich zu vielen bekannten Luminophoren. Einige Fragen, die nicht nur die grundlegenden photophysikalischen Prozesse betreffen, sondern auch die Wechselwirkung der UCNP mit anderen Lumineszenzreportern, die häufig für das Bioimaging verwendet werden, und die Wechselwirkung mit biologischen Medien bleiben jedoch offen. Diese Themen waren die Hauptmotivation für die vorgestellte Arbeit.

Diese Doktorarbeit untersuchte verschiedene Aspekte verschiedener Eigenschaften und Möglichkeiten für die Bioanwendung von Yb^{3+},Tm^{3+}-dotierten $NaYF_4$-hochkonvertierenden Nanopartikeln. Zunächst wurde der Einfluss verschiedener Gd^{3+}-Dotierungen auf die Struktur und das Hochkonvertierungsverhalten der Nanokristalle untersucht. Der Alterungsprozess des UCNP in Cyclohexan wurde über 24 Monate an Proben mit unterschiedlichen Gd^{3+}-Dotierungskonzentrationen untersucht. Strukturinformationen wurden mittels Röntgenbeugung (XRD), Transmissionselektronenmikroskopie (TEM) und dynamischer Lichtstreuung (DLS) gesammelt und in Bezug auf die spektroskopischen Ergebnisse diskutiert, die durch Multiparameter-Hochkonversion-Lumineszenz-Experimenten bei verschiedenen Temperaturen (von 4 K bis 295 K) erhalten wurden. Zeitaufgelöste und stationäre Emissionsspektren, die über diesen weiten Temperaturbereich aufgezeichnet wurden, ermöglichten ein tieferes Verständnis der photophysikalischen Prozesse und ihrer Abhängigkeit von strukturellen Änderungen des UCNP.

Ein neues Protokoll unter Verwendung eines im Handel erhältlichen hochsiedenden Lösungsmittels ermöglichte eine schnellere und kontrolliertere Herstellung von sehr kleinen und homogenen UCNP mit besseren photophysikalischen Eigenschaften. Weiterhin wurden die Vorteile einer passivierenden $NaYF_4$-Hülle gezeigt.

Der Förster-Resonanzenergietransfer (FRET) zwischen vier verschiedenen Spezies der $NaYF_4$:Yb^{3+},Tm^{3+} UCNP (synthetisiert unter Verwendung des verbesserten Protokolls) und einem kleinen organischen Farbstoff wurde untersucht. Der Einfluss der UCNP-Zusammensetzung und die Nähe von Tm^{3+}-Ionen (Donoren im FRET-Prozess) zu Akzeptorfarbstoffmolekülen wurden untersucht. Die effizienteste

Hochkonversionslumineszenz wurde bei dem UCNP mit einer schützenden inerten Hülle beobachtet. Die UCNP mit den nur in der Schale dotierten Tm^{3+}-Ionen leuchteten am schlechtesten, zeigten jedoch den effizientesten Energietransfer.

Im letzten Teil wurden zwei Oberflächenmodifizierungsstrategien angewendet, um die UCNP wasserlöslich zu machen. Dadurch wurde es gleichzeitig möglich, die UCNP mittels einer ungiftigen kupferfreien Klickreaktion mit den Liposomen zu verbinden, die als Modelle für weitere Zellexperimente dienten. Die Ergebnisse wurden mit einem konfokalen Mikroskopsystem untersucht, das durch weniger bekannte Abwärtsumwandlungseigenschaften von Yb^{3+},Tm^{3+}-dotiertem UCNP ermöglicht wurde. Vorläufige Antikörperfärbungstests wurden unter Verwendung von zwei primären Antikörpern und einem farbstoffmarkierten sekundären Antikörper an MDCK-II-Zellen durchgeführt.

Abstract

of the work titled:

Tm^{3+}-doped $NaYF_4$ nanoparticles: upconversion properties and bioimaging

submitted by Anna López de Guereñu, April 2020, at University of Potsdam.

Lately, the integration of upconverting nanoparticles (UCNP) in industrial, biomedical and scientific applications has been increasingly accelerating, owing to the exceptional photophysical properties that UCNP offer. Some of the most promising applications lie in the field of medicine and bioimaging due to such advantages as, among others, deeper tissue penetration, reduced optical background, possibility for multicolor imaging, and lower toxicity, compared to many known luminophores. However, some questions regarding not only the fundamental photophysical processes, but also the interaction of the UCNP with other luminescent reporters frequently used for bioimaging and the interaction with biological media remain unanswered. These issues were the primary motivation for the presented work.

This PhD thesis investigated several aspects of various properties and possibilities for bioapplications of Yb^{3+},Tm^{3+}-doped $NaYF_4$ upconverting nanoparticles. First, the effect of Gd^{3+} doping on the structure and upconverting behaviour of the nanocrystals was assessed. The ageing process of the UCNP in cyclohexane was studied over 24 months on the samples with different Gd^{3+} doping concentrations. Structural information was gathered by means of X-ray diff raction (XRD), transmission electron microscopy (TEM), dynamic light scattering (DLS), and discussed in relation to spectroscopic results, obtained through multiparameter upconversion luminescence studies at various temperatures (from 4 K to 295 K). Time-resolved and steady-state emission spectra recorded over this ample temperature range allowed for a deeper understanding of photophysical processes and their dependence on structural changes of UCNP.

A new protocol using a commercially available high boiling solvent allowed for faster and more controlled production of very small and homogeneous UCNP with better photophysical properties, and the advantages of a passivating $NaYF_4$ shell were shown.

Förster resonance energy transfer (FRET) between four different species of $NaYF_4$: Yb^{3+}, Tm^{3+} UCNP (synthesized using the improved protocol) and a small organic dye was studied. The influence of UCNP composition and the proximity of Tm^{3+} ions (donors in the process of FRET) to acceptor dye molecules have been assessed. The brightest upconversion luminescence was observed in the UCNP with a protective inert shell. UCNP with Tm^{3+} ions only in the shell were the least bright, but showed the most efficient energy transfer.

In the final part, two surface modification strategies were applied to make UCNP soluble in water, which simultaneously allowed for linking them via a non-toxic copper-free click reaction to the liposomes, which served as models for further cell experiments. The results were assessed on a confocal microscope system, which was made possible by lesser known

downshifting properties of Yb^{3+}, Tm^{3+}-doped UCNP. Preliminary antibody-staining tests using two primary and one dye-labelled secondary antibodies were performed on MDCK-II cells.

Table of contents

1 Introduction

1.1 ***Why upconversion?***

Upconversion luminescence (UCL) is a process of excitation of a solid-state material or a molecular system with lower-energy photons followed by emission of higher-energy photons (anti-Stokes-shifted luminescence) via intermediate excited electronic states, which makes it different from other optical multiphoton processes, e.g. multiphoton fluorescence and second (third, etc.) harmonic generation, which involve virtual electronic states and require much higher excitation power densities [1], [2]. Upconversion (UC) processes can be classified into triplet–triplet annihilation based UC, which normally uses matching triplet states of two different dye molecules as intermediate excited states, and lanthanide (Ln^{3+})-based UC using emissive Ln^{3+} ions [1], [3]. Usually, Ln^{3+}-based upconversion materials consist of a (single or multiple) Ln^{3+} ion-doped inorganic crystalline (or glass) matrix, e.g. metal oxide, fluoride, or phosphate. Most commonly used lanthanide ions include Yb^{3+}, Er^{3+}, Tm^{3+}, Ho^{3+}, Nd^{3+}, and Gd^{3+}[1], [4].

Although the process of UC in bulk materials (e.g., glasses and micrometer-sized particles), which involves multiple electronic transitions of the absorbing and emitting Ln^{3+} ions affected by ion–lattice interactions, has been studied since the middle of the previous century, it's only in the recent years that Ln^{3+}-doped upconverting nanoparticles (UCNP) have become recognized as a new class of luminescent probes for life and material sciences [1].

A particular advantage of UCNP is the emission at shorter wavelengths (visible or near-infrared) under near-infrared (NIR) excitation (anti-Stokes luminescence), where intrinsic biological fluorophores are not excited and light scattering is minimal [5], [6]. UCNP make for excellent luminescent probes that can be detected with very low optical background interference even in complex biological systems such as body fluids. Due to extremely long luminescence lifetimes (tens to hundreds of μs range), Ln^{3+}-based materials can be detected at higher penetration depths and with no background interference with time-gated spectroscopy to separate them from the short lifetimes (ns range) of conventional fluorophores [6], [7]. UCNP have many more advantages as luminescent reports, including sharp luminescence bands at tunable wavelengths and a possibility for multicolor imaging, low toxicity, the absence of blinking, chemical inertness, large anti-Stokes shifts, and outstanding photostability [7], [8]. The properties of UCNP and their advantages are summarized in Table 1.

1.2 Upconverting nanoparticles: fundamentals and possible applications

In the past decades, a lot of progress has been made in synthesis and tuning of properties of Ln^{3+}-doped UCNP. Synthesis conditions have been optimized, optimal structures and dopant concentrations have been sought out, standard protocols have been established. The influence of size, shape, crystalline phase, and dopant concentrations of UCNP have been performed by multiple researchers [9]–[14]. However, full understanding of the intrinsic processes, and hence, the influence of dopant concentration and shape/size on the luminescent properties of UCNP is still far from complete.

Table 1. Summary of the spectroscopic properties of upconverting nanoparticles and their advantages for photophysical and biological applications [5]–[8].

Feature of the UCNP	Advantages and possible applications
Near-infrared (NIR) excitation (976 nm)	Low light scattering, background-free bioassays, deep tissue imaging
Anti-Stokes emission	No cross-talk, excitation and detection wavelengths are well separated
Long luminescence lifetimes (tens to hundreds μs)	Time-gated emission measurements → higher penetration depths, no background interference
No photobleaching or blinking	Long-term imaging, single-particle applications
Multiple narrow emission bands in the UV/Vis/ NIR regions	Multicolor imaging, internal standard for energy transfer applications
Chemically inert	Possibility of prolonged storage
Low toxicity	Bioimaging

In Figure 4, an energy level diagram (a) with respective luminescence bands (b) of the upconversion mechanism in β-$NaYF_4$:Yb^{3+}, Tm^{3+} UCNP is shown. Absorption of light at 976 nm promotes the sensitizer ion Yb^{3+} from its ground state $^2F_{7/2}$ to the excited state $^2F_{5/2}$. This transition is reversible, and Yb^{3+} can emit near-infrared (NIR) light. The absorbed energy can nevertheless be transferred from the sensitizer Yb^{3+} to the activator Tm^{3+}. Once Tm^{3+} is excited, it can be pumped into higher-energy states by sequential energy transfers from excited Yb^{3+}. Radiative relaxation of Tm^{3+} leads to the emission of blue (~470 nm), NIR (800 nm), and (with lower intensity) UV and red (~360 nm and ~680 nm) light [1].

Among the applications of UCNP that have been gaining an increasing amount of attention in the past years is the resonant energy transfer (RET or FRET, for Förster resonance energy transfer), a non-radiative phenomenon based on Coulombic interactions, where the energy is transferred from an excited donor (D) fluorophore to an acceptor (A) fluorophore by means of intermolecular dipole–dipole coupling [15]. The efficiency of FRET process depends on the

D-A distance with an inverse 6th-power law, thus, it is frequently used to determine the distance between molecules on a nanometer scale: to monitor conformational changes in biomolecules or to quantitatively determine a binding interaction between two molecules, processes connected to a change in relevant distance [16], [17]. This method presents a particular interest due to the high sensitivity (even on a single molecule level) to distance alteration [18].

Using UCNP in FRET-based assays increases the complexity of the resulting energy scheme: UCNP are a system with an inner energy transfer process of its own, and introducing another agent into this system increases the complexity of the involved processes manifold and decreases the overall efficiency. However, due to particular interest in UCNP as FRET donors due to their exceptional photophysical properties (long luminescence lifetimes, no blinking, etc.), this phenomenon needs to be studied, while the current understanding of the underlying processes is still far from complete.

1.3 Upconverting nanoparticles as biological reporters

Due to a deeper understanding of nanomaterials achieved over the last decades, an expansion of their applications in science, technology and medicine has been on the rise ever since. Luminescent nanoparticles complement already existing organic chromophores in luminescence-based analytical chemistry due to such drawbacks of the latter as the photobleaching, ns-fluorescence lifetimes, and chemical instability [15]. Among the most popular are semiconductor quantum dots (QD), which are claimed to be photostable, bright, with sharp emission lines, which can be tailored by adjusting the size of the QD (size quantization effect), and allow to establish multiparameter detection schemes [8], [19]. Despite their advantages, QD also have some drawbacks limiting their broader application, such as toxicity, chemical instability (dissolution), and “blinking” (i.e., random fluctuations in QD photoluminescence) [20], [21].

Another popular option are graphene quantum dots, which have tunable optical properties, high brightness and photostability. They are more biocompatible than QD, which gives them an advantage for biomedical applications. However, application of graphene QD for biosensing is limited by short luminescence lifetimes, excitation-dependent effects of photoluminescence and a lack of control over their dimensions and surface chemistry [8], [15].

Due to aforementioned intrinsic optical and photophysical properties, UCNP have become an attractive option for biological sensing, diagnostics and phototherapy. The main requirements for the UCNP for bioapplications usually include homogeneity in shape and size, smaller crystal dimensions ($\leq$ 10 nm), and colloidal stability in aqueous media. There is a plethora of surface modification methods to achieve the needed design of the UCNP surface for various applications [22]. As-synthesized UCNP are normally hydrophobic, thus, the ligand is meant to improve the biocompatibility of UCNP and at the same time protect it from the aqueous media [23]. Ideally, it also provides a potential for labelling of the UCNP with specifically tailored groups [24].

Despite the great variety of known modification procedures, there are still some issues to be addressed. Some common problems include instability in aqueous environments, aggregation and precipitation, batch-to-batch variability, and low quantum yields.

Some common reported UCNP-assisted assays include, among others, detection of nucleic acids, proteins, hormones, common metabolites such as glucose, and toxins [25], [26], [27] [28]. The sensitivity of UCNP in most of these assays was higher or comparable with the commonly used dyes and other reporters, and the possibility for creating multimodal UCNP-based probes has allowed for simultaneous detection of various substances.

UCNP have successfully been implemented for imaging, namely, targeted *in vivo* imaging of cells and tissues [29]–[31], multi-color and multi-modal imaging in rats and mice [32], [33]–[35], and theranostics [36], [37], [38]. In many cases less sample volume was needed for the experiment compared to more commonly used luminescent probes, and the accumulation of the UCNP was not critical or even not present. However, one of the complications associated with the application of UCNP for bioimaging was the lack of commercial systems, hence, most research groups needed to develop their own instruments, specifically modified for the desired applications.

Accessing the toxicity of UCNP still presents a challenge, however, due to their structural complexity. Nanoparticles show biological and environmental behaviors as a result of a combination of various intrinsic properties, e.g., chemical composition, surface chemistry, physical parameters (size, shape, structure, agglomeration etc.), environmental factors (pH, ionic strength, dissolution rate, and temperature), and presence of other components or electromagnetic fields [39].

Although typically considered chemically inert due to their photochemical and thermal stability, some studies on UCNP behaviour in biological systems have indicated the possibility of inflammation in cells after prolonged exposure of nanocrystals to biological conditions. This shows the necessity to improve the surface/shell design of UCNP and the need to keep this aspects in consideration when performing *in vivo* experiments with UCNP [39]. *In vivo* studies usually demonstrate no adverse effects and rapid removal of UCNP from living organisms, although some have indicated accumulation of UCNP in liver and spleen of mice over the course of some weeks, which, however, didn't cause any symptoms of toxicity[40] [33] [41]. All of the aforementioned problems need to be addressed, but nevertheless, UCNP still present very promising luminescent probes for bioimaging and bioapplications due to their unique photophysical properties, multimodality, stability and biocompatibility.

1.4 Aim and Thesis Overview

Given various advantages of UCNP as luminescent reporters and the current state of progress and research carried out on the subject, this thesis dedicated special attention to four different issues that have still not been studied and addressed in the literature to the utmost. In short:

(i) the first objective was to gain a deeper insight into the influence of dopant (Gd^{3+}) concentration on the structural and luminescent properties of Yb^{3+},Tm^{3+}-doped $NaYF_4$-based UCNP;

(ii) establish a synthesis protocol that would result in unidimensional and bright UCNP, and allow to precisely control the size and the crystalline phase of the particles;
(iii) achieve an understanding of the influence of the D-A distance and UCNP architecture and composition on FRET process between the UCNP and an organic dye;
(iv) and, lastly, create water soluble and colloidally stable UCNP with the possibility for further chemical modification of the surface and introduce them to biological systems.

The nanoparticles used for the experiments were based on the $NaYF_4$ lattice and doped with Yb^{3+} as sensitizer and Tm^{3+} as activator unless specified otherwise. The choice of Tm^{3+} as the activator ion was motivated by the fact that one of its most prominent luminescence bands is observed at 800 nm, which is very fortunately within the biooptical window, allowing for background-free detection of its luminescence and high penetration depth into biological matrices.

A short description of the subsections of this dissertation is provided for the purpose of a rapid overview.

Fundamentals

This chapter presents an introduction to the process of upconversion. A literature review on different approaches and requirements to produce high quality upconverting nanoparticles was presented. The mechanism of FRET was discussed. Surface modification strategies and different applications of UCNP in biological assays and imaging were overviewed.

Experimental and characterization methods

Here, the instrumentation and the implemented techniques were described as well as the synthesis protocols and equations.

Results and discussion

This chapter consists of five parts:
1. In the first one, the solvothermal synthesis procedure of Yb^{3+}, Tm^{3+}, Gd^{3+}-doped $NaYF_4$-based UCNP and its optimization was described.
2. In the second part, the influence of Gd^{3+} content (10-50%) on the structural and luminescent properties of $NaYF_4$-based UCNP was studied in detail. The ageing process of UCNP stored in cyclohexane over the course of 24 months was also examined based on the samples with different Gd^{3+} content, creating a four-dimensional variation of parameters.
3. In part three, an upgraded synthesis route utilizing Therminol®66, a commercially available high boiling solvent, resulting in sub-10 nm, highly uniform and bright UCNP, was described. The same protocol was used to create core-shell $NaYF_4$-based UCNP and their advantages over core UCNP were discussed in detail.
4. In the fourth part, the process of energy transfer between Tm^{3+}-doped upconverting nanoparticles and an organic dye was studied on the example of four different UCNP architectures. The possibility of FRET between UCNP and the dye attached to their surface

is contemplated, and investigations of the upconversion behaviour of the four different UCNP species was presented.

5. In the last part, two surface functionalization procedures were developed to produce hydrophilic UCNP: using phospholipids and a custom block copolymer. Copper free click chemistry, a cycloaddition of an azide group to cyclooctynes, was tested for the resulting hydrophilic UCNP, using dye-labelled liposomes as models for cells. Confocal imaging was used to assess the yield of the click reaction and to observe the UCNP in biological conditions. The lesser known downshifting properties of Yb^{3+}, Tm^3-doped UCNP with traces of Er^{3+} were described and used for on-site imaging on a conventional microscopy setup. And, finally, the interactions of water-soluble UCNP with cells were examined on the confocal microscope system, and the principles of the antibody staining using primary and secondary antibodies on MDCK-II cells were tested.

Conclusion and perspectives

In the final chapter, the closing discussion and outlook of the performed work are presented.

2 Fundamentals

2.1 Basics of upconversion

2.1.1 Brief history and introduction into the process of upconversion

The process of upconversion (UC) in solid state materials was first discussed in literature in the 1960s [42], [43]. Before that, the emission energies for all known anti-Stokes emissions exceeded the excitation energies by only a few hundred cm^{-1}. Among the known processes at the time were the anti-Stokes emission for the so-called thermal bands, the Raman effect for the anti-Stokes sidebands, thermoluminescence, and superexcitation, or using excited-state absorption (ESA) to raise an already excited electron to an even higher level. All of the above were characterized by rather weak emissions[43].

It continued to be just a curious phenomenon with limited practical applications, until, after the introduction of solid state lasers, it became recognized as a potential basis for an efficient nonlinear laser excitation scheme [44]. In the mid-1970s the first reports of efficient upconversion in co-doped materials were published, which led to an ever increasing interest, the discovery of high efficiency upconversion in nanomaterials, and later a realisation that upconverting nanomaterials have various applications across many fields [2]-[45].

Upconversion refers to nonlinear optical processes characterized by the successive absorption of two or more lower energy photons (usually in the near infra-red spectral range) followed by the emission of the output radiation at a shorter wavelength (higher energy) than the pump wavelength (e.g. ultraviolet, visible or NIR) [45]. For the UC processes, emission is found to exceed excitation energies by 2000-20000 cm^{-1}, which is a basic violation of the Stokes law. The process of upconversion was first reported in 1961, by W. Kaiser and C. G.B. Garrett for non-linear two-photon optical processes on an example of Eu^{3+}-doped CaF_2 crystals [46], and for excited state absorption by J. Porter in La:$PrCl_3$ [47]. In 1966, F. Auzel suggested energy

transfer upconversion between RE ions, both of which are in an excited state at the initial step of energy transfer [48].

2.1.2 Possible UC mechanisms

A number of different mechanisms can be involved in the process of UC (alone or in combination), which can be divided into the following broad classes: excited state absorption (ESA), energy transfer upconversion (ETU), formerly known as APTE (for addition de photon par transferts d'energie) [49], cooperative upconversion between two ions or between a pair of ions and a third one, and photon avalanche (PA). All of the above involve the sequential absorption of two or more photons. Thus, UC processes are different from the multiphoton process where the absorption of photons occurs simultaneously [43], [45].

Out of the aforementioned UC mechanisms, the ETU process is not only the most efficient, but also requires a lower excitation power density [50]. ESA is the least efficient UC process, while efficient upconversion in PA is possible with metastable intermediate levels acting as a storage reservoir for pump energy. Let's look at those mechanisms in more detail.

In **ESA**, a single ion gets excited by successively absorbing several pump photons (Figure 1, a). If excitation energy is resonant with the transition from ground level (G) to excited metastable level (E1), photon absorption occurs which leads to population of E1 from G (a process called ground state absorption (GSA)). The second pump photon promotes the population of the upper emitting state (E2) from E1 and leads to upconversion emission, corresponding to the E2-G optical transition.

In **ETU** the metastable level is also populated by two sequentially absorbed photons. However, the excitation is realized through the energy transfer between two neighbouring ions (Figure 1,b). Said ions can absorb a pump photon of the same energy, populating the metastable level E1. A non-radiative energy transfer process promotes one of the ions to upper emitting state E2, and the other ion relaxes to ground state (G). Thus, in the ETU process the UC efficiency depends on the average distance between the neighbouring dopant ions which is determined by the dopant concentration.

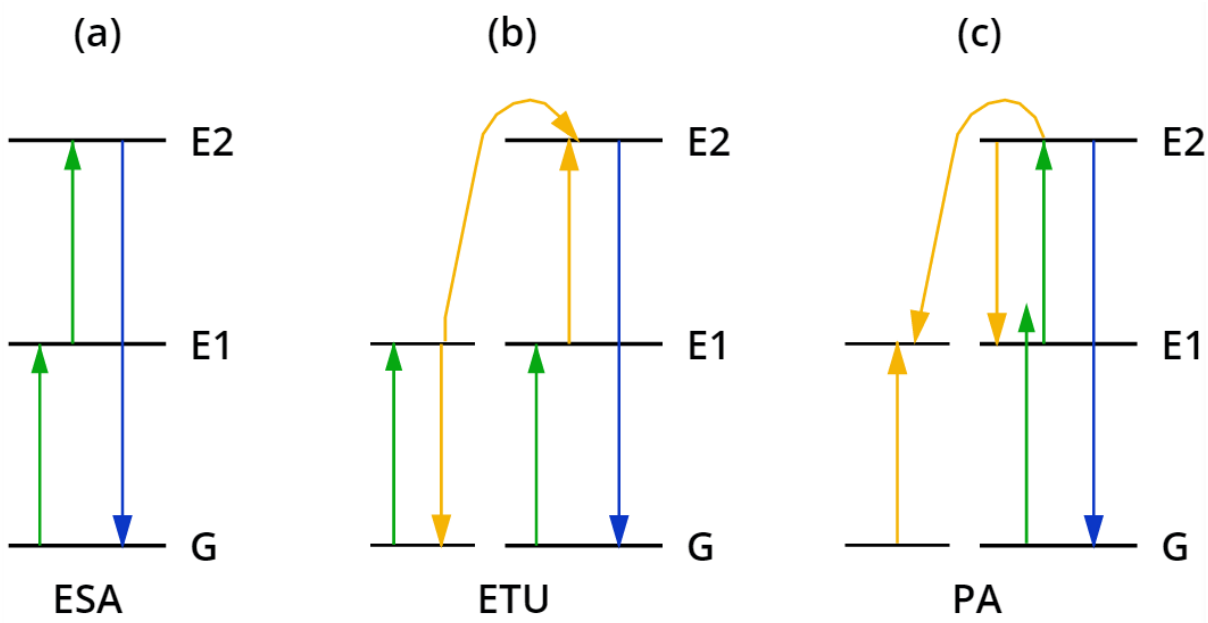

Figure 1. Schematic representation of principal UC processes: (a) excited state absorption, (b) energy transfer upconversion, (c) photon avalanche. The green, yellow, and blue arrows represent photon excitation, energy transfer, and emission processes, respectively.

The process of **PA** requires a pump intensity above a certain threshold value. Firstly, E1 is populated by non-resonant weak GSA, then resonant ESA populates the upper visible-emitting level E2 (Figure 1, c). When the metastable level is populated, the excited ion transfers energy via the cross-relaxation process (or ion pair relaxation) to a neighboring ion in ground state, thus, both ions occupy the intermediate level E1. Then the two ions readily populate level E2 and initiate further cross-relaxation, exponentially increasing E2 population by ESA, which leads to strong UC emission as an avalanche process [45].

Presently used non-linear emitters often implicate upconversion systems based on the ETU mechanism. One of such systems is lanthanide (Ln^{3+})-doped upconverting nanoparticles (UCNP) that are composed of a crystalline host and Ln^{3+} dopants added to the host lattice in low concentrations acting as localized luminescent centers. In the process of sensitized luminescence, one dopant ion gets excited by a non-radiative energy transfer from another dopant ion and moves to a higher energetic state. The ion that accepts the energy and emits the radiation is called activator or acceptor (A), and the ion that donates the energy is called sensitizer or donor (D). Although most lanthanide-doped crystalline host materials exhibit UC, efficient upconversion is only observed in a small number of well selected dopant–host combinations.

2.1.3 Requirements for successful UC materials: D and A

Lanthanide ions usually exist as trivalent ions (Ln^{3+}) and are associated with the filling of the 4f-shell. Their multiple metastable levels make Ln^{3+} potentially attractive for UC. 4f electrons of Ln^{3+} are shielded by the filled $5s^2$ and $5p^6$ sub-shells, and thus they show weak electron–phonon coupling that is responsible for sharp and narrow f–f transition bands. Besides, the f–f transitions are symmetry forbidden, which leads to low transition probabilities and long-lived

excited states (up to 0.1 s). Such ions as Er^{3+}, Tm^{3+}, Pr^{3+} and Ho^{3+} not only possess ladder-like energy levels, but also the energy difference between their excited and intermediate levels is small enough to facilitate photon absorption and energy transfer required in the process of UC, which makes them practically applicable as activators [51]. Out of the mentioned ions, Er^{3+} and Tm^{3+} comprise the most efficient UC nanocrystals since they have relatively large energy gaps and thus low probabilities of non-radiative transitions. The distance between two neighboring activator ions is an important parameter to consider, since high doping concentration leads to cross-relaxation non-radiative energy loss and non-radiative energy migration to surface quenchers. Hence, the concentration of A should be kept low and carefully adjusted. Another important parameter is the absorption cross-section of the ions, which is rather low for most Ln^{3+} activators in the NIR region, leading to low pump efficiency.

In order to partly allow the f-f transitions, activator ions should be embedded in a host matrix with an asymmetrical crystal field, and accompanied by sensitizing ions that absorb the incoming photons and transfer the energy to the A ions.

Co-doping a sensitizer ion with a sufficient absorption cross-section in the NIR region tends to enhance the efficiency of UC. Yb^{3+} serves as a particularly advantageous sensitizer for several reasons. Firstly, it has a very simple energy level scheme (Figure 4). Secondly, the energy of the $^2F_{7/2}$ - $^2F_{5/2}$ electronic transition is in resonance with 976 nm radiation and has a reasonably large absorption cross-section (ϵ_{974} = 2.03) [52]. Thirdly, the energy gap of the $^2F_{7/2}$ - $^2F_{5/2}$ transition overlaps with many f–f transitions of typically used A ions, permitting efficient (quasi)resonant energy transfer from Yb^{3+} to other ions [28].

2.1.4 Requirements for successful UC materials: host material

Appropriate host material is an essential choice to make in the synthesis of Ln^{3+}-doped UCNP with required optical properties. The lattice structure of the host determines the spatial positioning of the dopants, while the anionic environment has an impact on the strength of the dopants crystal field and its ability to allow the Laporte-forbidden f-f transitions. Host materials generally require good chemical stability, transparency to the excitation light and UC emission, close lattice matches to dopant ions and low phonon energies [53], [54].

Some non-radiative processes that decrease the UC efficiency include cross-relaxation between two neighbouring Ln^{3+} ions or a Ln^{3+} and impurities in the host and phonon quenching (multiple phonons "bridge" the energy gap between excited and ground states and carry excited electrons to the ground state through non-radiative energy transfer). To maximize the luminescence quantum yield, host lattice should have low phonon energies: according to the energy gap law, if the gap between the dopants energy states exceeds 6 phonon energies, the dominating process is radiative relaxation, otherwise non-radiative pathways will dominate [28].

Phonon energy can be reduced through the minimization of lattice defects. Host lattice spacing should match the spacing of the dopants, thus, inorganic salts of all Ln^{3+} as well as Ca^{2+} and Ba^{2+} or Ti^{4+} and Zr^{4+} are often used as hosts. However, such materials show crystal defects, i.e. lattice vacancies, which compromises their optical properties. Na^{2+}, Ca^{2+}, and Y^{3+}-based materials resist the formation of vacancies and lattice stresses and have closely matched ionic

radii to Ln^{3+} ions, which makes the fluoride-based salts of aforementioned ions most attractive and used lattice material. To date, $NaYF_4$ doped with Yb^{3+} and Tm^{3+} or Er^{3+} is the most commonly used combination [55].

However, the crystalline phase and size of the host material also have an effect on the process of UC and optical properties. $NaYF_4$-based UCNP exist either in cubic (α-$NaYF_4$) or hexagonal (β-$NaYF_4$) crystal phase (Figure 2). It has been repeatedly shown that the $NaYF_4$ based materials with hexagonal crystal lattice show a much higher UC efficiency compared to analogous materials in cubic phase. This phenomenon can be explained by the fact that β-$NaYF_4$ has lower symmetry, thus, the crystal field around dopant ions is less symmetrical, which increases the probability of Laporte forbidden f-f transitions due to the increase of electronic coupling between 4f energy levels [28], [56], [57].

Another factor which can facilitate 4f-4f transitions is the increase in the crystal field strength around the dopant ion. This can be achieved by decreasing the ionic radii of one of the cations in the lattice [55]. However, an increase in asymmetry can lead not only to an increased luminescence efficiency of the dopant ion, but also to elevated phonon energies, which leads to non-radiative multiphonon relaxation to lower energy levels. Thus, the host lattice, dopant ions and their concentrations should be carefully selected for efficient UC.

Particle size has also been reported to affect the luminescent properties of the UCNP, from emission enhancement to influencing the relative emission intensity of luminescence bands [58]. However, it has been attributed to surface effects rather than quantum confinement effects due to the small Bohr radius of the exciton in the lanthanide-doped nanocrystals. The emission spectrum of the UCNP is a sum of emissions from dopant ions on the surface and in the bulk of the particles. In small UCNP the concentration of surface dopants is higher than in larger ones, and thus, variation in emission color or intensity can be achieved through size (and hence concentration of surface dopants) control [45].

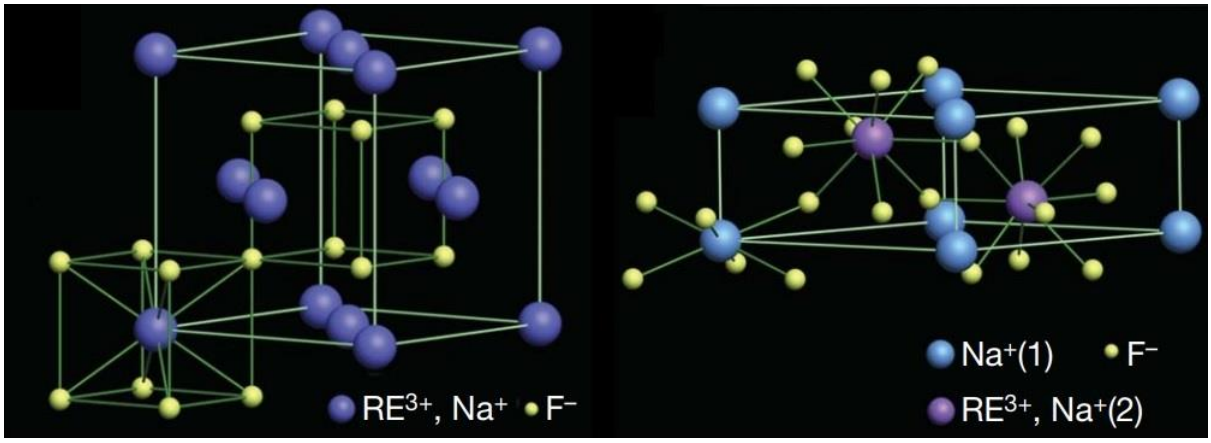

Figure 2. Schematic representation of cubic- and hexagonal-phase of $NaYF_4$, respectively. In the cubic phase, equal numbers of F^- cubes contain cations and vacancies. In the hexagonal phase, the order of F^- ions allows two types of cation sites: either occupied by Na^+ or randomly occupied by Na^+ and Re^{3+}[59].

This thesis will focus on Yb^{3+}, Tm^{3+}-doped β-$NaYF_4$ nanocrystals. These UCNP are typically covered with an organic capping ligand, here oleic acid (OA), which improves their colloidal

stability. Upon 980 nm excitation, they show their strongest emission bands around 451, 481 (blue) and 800 nm (NIR), the latter fitting nicely in the window (700–1000 nm) for optical measurements of most biological tissues (Figure 3).

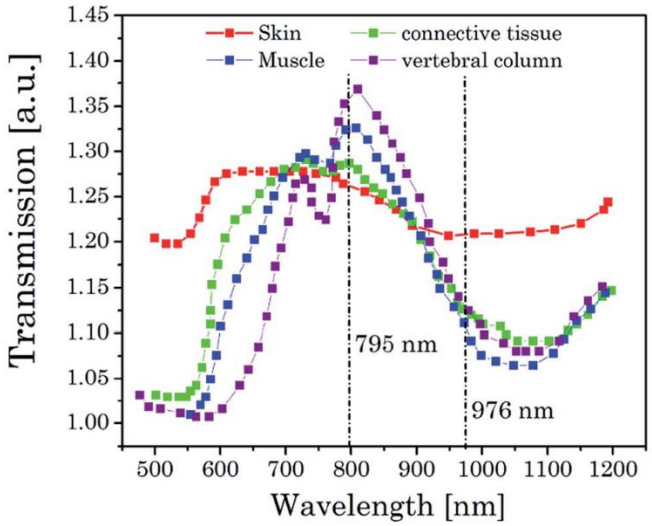

Figure 3. Transmission spectra of different biological tissue in a spectral range of 500–1200 nm [60].

2.1.5 Optical properties, emission spectra

Optimal doping concentrations for achieving the highest UC efficiency values of Yb^{3+}, Tm^{3+}-doped UCNP are quite hard to estimate: their particle size and excitation power density dependent (de)population behaviors are yet to be fully understood. There also are many possible cross-relaxation processes between Tm^{3+} ions that can happen simultaneously with ETU from Yb^{3+} to Tm^{3+} (Figure 4).

In Yb^{3+}, Tm^{3+}-doped UCNP, upconversion emission bands at 451, 481, 646, and 800 nm can be ascribed to the $^1D_2 \rightarrow {}^3F_4$, $^1G_4 \rightarrow {}^3H_6$, $^1G_4 \rightarrow {}^3F_4$, and $^3H_4 \rightarrow {}^3H_6$ transitions, respectively. There are additional upconversion emissions in the UV region at 345 and 365 nm that can be assigned to the $^3P_2 \rightarrow {}^3F_4$ and $^1D_2 \rightarrow {}^3H_6$ transitions. For shortness, we will address the most prominent $^1D_2 \rightarrow {}^3F_4$ (451 nm), $^1G_4 \rightarrow {}^3H_6$ (481 nm) and $^3H_4 \rightarrow {}^3H_6$ (800 nm) as B1, B2 (for blue) and NIR (for near infra-red) bands, respectively. Usually, the UC emission intensity at 800 nm is the highest in Yb^{3+}, Tm^{3+}-doped UCNPs [44]. Zhang et al. have demonstrated that the relative intensity of the B1 and B2 against NIR decreases with the increase of Tm^{3+} concentration. This can be explained by the shortening of the Tm^{3+}- Tm^{3+} distance and enhancement of the cross-relaxation between $^1G_4 \rightarrow {}^3H_4$ and $^3F_4 \rightarrow {}^3F_2$ as a result. Hence, the population of $^1G_4$ would decrease, leading to the quenching of B1 and B2 emission, and the increase of population of $^3H_4$, resulting in the enhanced NIR emission [61].

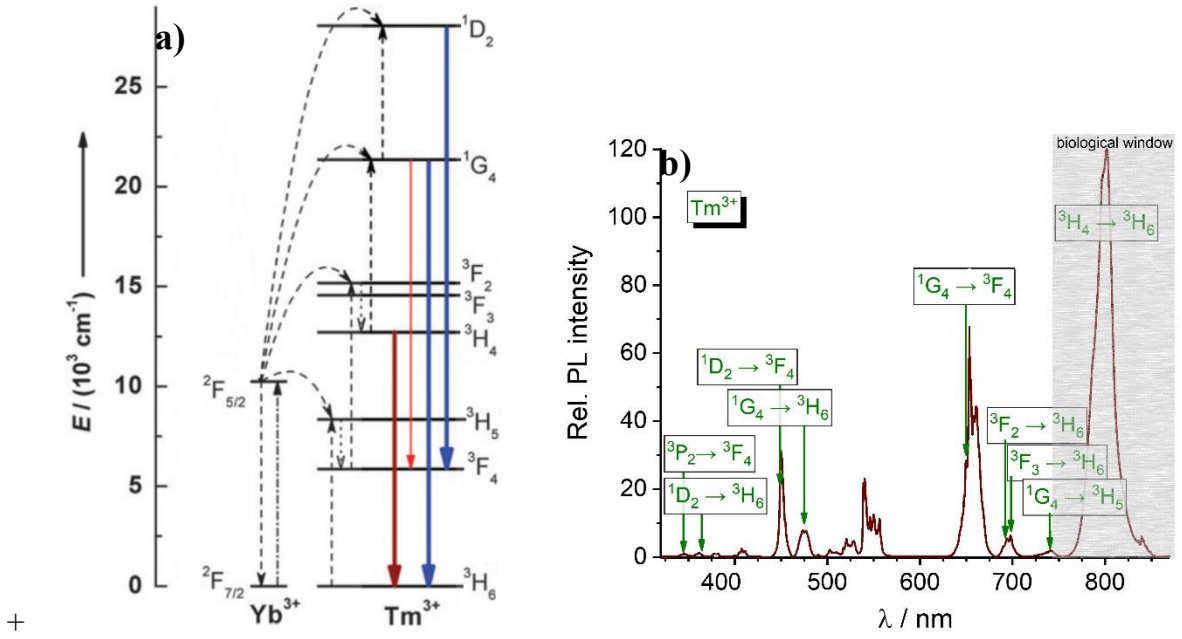

Figure 4. (a) Proposed energy transfer mechanisms showing the UC processes in Tm^{3+}, Yb^{3+}-doped crystals under 980 nm excitation adapted from [45]. The dashed-dotted, dashed, dotted, and full arrows represent photon excitation, energy transfer, multiphonon relaxation, and emission processes, respectively. Only visible and NIR emissions are shown. (b) Typical Tm^{3+} emission spectra with respective transitions assigned for each peak. The most prominent bands are at 451 nm ($^1D_2 \rightarrow {}^3F_4$), 481 nm ($^1G_4 \rightarrow {}^3H_6$) and 800 nm ($^3H_4 \rightarrow {}^3H_6$); B1, B2 (for blue) and NIR (for near infra-red) bands, respectively

As of now, there's no single compelling model that would describe all the processes of population and depopulation of Yb^{3+}, Tm^{3+}-doped crystals. Several models have been proposed to explain the population of higher ($^1G_4$ and $^1D_2$) energy levels of Tm^{3+}: three and four ETU steps to populate $^1G_4$ and $^1D_2$, respectively [62]; population only by CR processes, such as ($^3F_2 \rightarrow {}^3H_6$; $^3H_4 \rightarrow {}^1D_2$), ($^1G_4 \rightarrow {}^3F_4$; $^3H_4 \rightarrow {}^1D_2$) and ($^1G_4 \rightarrow {}^1D_2$; $^3H_4 \rightarrow {}^3F_4$) [63]; or a mixture of ETU and different CR processes, i.e. ($^1G_4 \rightarrow {}^3H_4$; $^3F_4 \rightarrow {}^2F_{2/3}$), ($^1G_4 \rightarrow {}^3F_{2/3}$; $^3H_5 \rightarrow {}^3F_{2/3}$) and ($^3H_4 \rightarrow {}^3F_4$; $^3H_6 \rightarrow {}^3F_4$) [64]. Thus, it can be assumed that for different Tm^{3+} UC emission bands, highest efficiency can be achieved by different doping concentrations.

2.1.6 Core-shell approach

Dopants at the surface of UCNP can be quenched by additional non-radiative relaxation pathways. Mostly this happens due to multiphonon relaxation through interactions with the high-energy vibrational modes of hydroxy- and amine-functionalities of capping ligands, solvent molecules and weakly bound surface impurities. Quenching is usually ascribed to the lack of effective physical protection of the host lattice [28], [65]. Thus, UCNP with small radii and high surface to volume ratio show lower UC efficiencies than respective bulk materials [53]. In case of higher dopant concentration, energy propagation can occur from the ions inside the UCNP through neighbouring ions to the surface, where energy gets released non-radiatively [45].

One of the most elegant and efficient strategies to combat these phenomena and enhance the brightness of UCNP is the design of core–shell structures able to protect the lanthanide ions from non-radiative quenching as well as to promote energy transfer among the different components to favour the upconversion mechanisms [66].

Besides that, a shell can also serve as an excellent way to combine different functional units into a single nanoparticle. For example, incompatible dopant ions can be spatially confined in separate layers of a core–shell nanoparticle to eliminate short-range cross-relaxations that quench luminescence. A long-range energy migration process could be used to bridge desired energy transfers across the core–shell interface [67]. Various shell structures have been reported in literature: Wang et al used CaF_2 to protect rare-earth ions from leaking and ensure biological safety [68], Zhong et al used a multi-shell $NaYF_4$ based structure to allow excitation at 800 nm with the use of Nd^{3+} and implemented a "transition layer" to suppress relaxation [69], Li et al. have developed a layer-by-layer strategy to allow the growth of multiple shells with tuneable properties [70]. Multicolor emissions, magnetic and radioactive properties can be achieved by tuning of the core-shell structures.

However, these applications are out of scope for this Ph.D. thesis, so we will rather focus on "passivating" shells designed to protect Ln^{3+} dopants from quenching.

In general, there are three methods for the fabrication of core–shell UCNP architectures: seed-mediated shell growth, self-focusing by Ostwald ripening, and surface cation-exchange [28], [71]. The cation exchange process involves the replacement of the ions native to the UCNP by the ions present in solution [72]. This approach allows to precisely tune the shell size and to obtain ultra-small UCNP, since there's no change in the particle diameter after the shell addition.

Epitaxial growth of inorganic nanocrystals can lead to generation of core-shell or hybrid structures, depending on the material. A good way to assure a homogeneous inorganic shell is using isotropic "seed crystals" with small lattice mismatches between the shell and the core. Usually, the material used for the synthesis of a passivating shell is the same as the core host lattice, but without any dopant ions. However, this method suffers from such limitations as independent nucleation and anisotropic shell growth. To overcome this, an independent fabrication of core and shell with purification after each step should be performed. This can be achieved by either using small sacrificial NP, or a pre-synthesized shell precursor [70][73]. This method also allows precise control over shell thickness.

Several studies went in depth to analyze the influence of the shell thickness on the quantum yield of the UCNP. [74] studied a range of $NaYF_4$: Tm^{3+} (8%), Yb^{3+} (20%) nanoparticles, with passivating shells ranging from 1.1 nm, 6.3 nm, 8.4 nm, 25.9 nm to 29.5 nm. They found out that the 6.3 nm shell provided the highest luminescent emission intensity and luminescence lifetimes. [75] investigated the effect of the $NaLuF_4$-shell thickness of β-$NaYF_4$:Yb^{3+} (33%), Er^{3+} (5%) core−shell UCNPs on the upconversion luminescence quantum yield. The shell thickness was increased from 0.5 to 12 nm in 10 steps, and the luminescence quantum yields were compared. It was shown that the quantum yield increased with the increase of shell thickness, but after reaching ~ 4% at 4 nm, there was almost no further increase in UC

efficiency. [76] have also studied the relationship between the shell thickness and quantum yield of $NaGdF_4$: Yb^{3+} (20%), Er^{3+} (2%) UCNP with shells up to 10 nm, and have demonstrated that optimal shell thickness for combined visible and short wave infra-red (SWIR) imaging was 5 nm. Based on the aforementioned studies, one could conclude that the optimal shell thickness of several nm provides a good balance between preservation of smaller UCNP sizes and homogeneity and improving the UC efficiency by eliminating the surface quenching effects.

2.2 Förster resonance energy transfer (FRET)

2.2.1 Basics of FRET

Energy can be transferred from one chromophore to the other via different mechanisms, for example: resonance energy transfer, reabsorption, complex formation, and collision quenching. Förster resonance energy transfer (FRET) describes the energy transfer between a donor (D) chromophore in its electronic excited state to an acceptor (A) chromophore through non-radiative dipole–dipole coupling [77]. The transmission of an energy quantum from its absorption site to the site of its utilization, happens non-radiatively, via a resonance interaction between the two chromophores, over distances much larger than interatomic. There is also no conversion to thermal energy and no kinetic collision of the donor and the acceptor. In order for the resonance energy transfer to occur, the following conditions must be met: (i) the distance between D and A should be in the range of several nm (this parameter is individual for every D-A couple and will be discussed in more detail), (ii) there should be a spectral overlap between the emission of D and the absorbance of A, (iii) D and A must have strong electronic transitions in the UV, visible, or IR, (iv) the emission of the D has to have a reasonably high quantum yield, and (v) the orientation factor (κ^2), the orientation factor between the two fluorophore dipoles determined by the transition dipole moment orientations of the donor and acceptor species, should not be too small [78].

To better understand the D-A distance criteria, let's take a closer look at it. Förster presented D as a spatially close group of electrical oscillators producing an electrical field around thyself. The space of that field consists of four zones: the contact zone (<1 nm), the near zone (1-10 nm), the intermediate zone (10-100 nm), and the far zone (>100 nm) (sometimes reduced to intermediate, near and far zones) [79]. FRET only happens in the near zone, while on distances less than 1 nm there's a competing charge transfer-mediated mechanism (Dexter type), involving molecular overlap, and a chance of complex formation between D and A [80]. Besides, Förster's theory fails at such small distances due to the breakdown of the ideal dipole approximation [81].

In the far zone, i.e. further than 10 nm, Förster's theory doesn't apply due to the higher electric field contributions that can't be ignored like they can be in the near field. On larger distances, reabsorption by A can also take place.

Now let's go through the basics of the Förster theory.

In general, the following three equations sum up the conclusion of the theory:

$$\eta_{FRET} = \frac{k_{FRET}}{k_{FRET} + 1/\tau_D} = \frac{R_0^6}{R_0^6 + r^6} \quad (1)$$

$$k_{FRET} = \frac{1}{\tau_D}\left(\frac{R_0^6}{r^6}\right) \quad (2)$$

$$R_0^6 = \frac{9(\ln 10)\kappa^2 \Phi_D J}{128\pi^5 n^4 N_a} \quad (3)$$

Here, k_{FRET} is the rate of energy transfer,

τ_D is the luminescence lifetime of D in the absence of A,

r is the distance between D and A,

R_0 is the Förster distance, or the D–A distance at which $k_{FRET} = 1/\tau_D$, meaning that at this distance, the probability of the excited D to fluoresce is equal to the probability of transfer of energy to the A,

η_{FRET} is the efficiency of energy transfer,

J is the overlap integral,

κ^2 is the orientation factor,

Φ_D is the quantum yield of the donor fluorescence in the absence of acceptor,

n is the refractive index of the medium,

$N_A = 6{,}0221415 \cdot 10^{23}$ per mole.

Kappa squared, κ^2, is the dipole orientation factor. Its value varies between 0 and 4 and can be described with the formula:

$$\kappa^2 = \cos\theta_T - 3\cos\theta_D \cos\theta_A \quad (4)$$

Here, θ_D is the angle between the D emission transition dipole moment and the line that connects D and A, θ_A is the angle between the A absorption transition dipole moment and the line that connects D and A, and θ_T is the angle between the D emission transition moment and the A absorption transition moment.

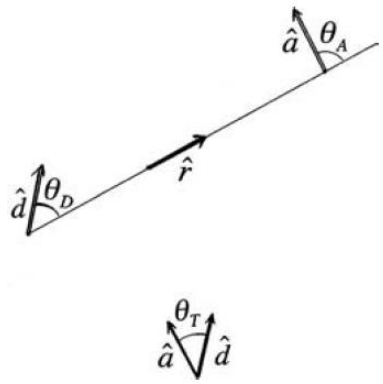

Figure 5. Representation of $\boldsymbol{\theta_D}$, $\boldsymbol{\theta_A}$, and $\boldsymbol{\theta_T}$ angles and the unit vectors $\boldsymbol{d}$, $\boldsymbol{a}$, and $\boldsymbol{r}$ [78].

Here, unit vectors are the following: $\hat{\boldsymbol{d}}$ goes along the donor transition dipole moment, $\hat{\boldsymbol{a}}$ along the acceptor transition dipole moment, and $\hat{\boldsymbol{r}}$ along the line from the donor to the acceptor. $\hat{\boldsymbol{d}} \cdot \hat{\boldsymbol{r}} = \boldsymbol{cos\theta_D}$, $\hat{\boldsymbol{a}} \cdot \hat{\boldsymbol{r}} = \boldsymbol{cos\theta_A}$, $\hat{\boldsymbol{a}} \cdot \hat{\boldsymbol{d}} = \boldsymbol{cos\theta_T}$.

Spectral overlap integral, the overlap integral between the area-normalized emission spectrum of the D and the absorption spectrum of the A, depends on both of the aforementioned spectra. Of several ways to calculate the overlap integral, the wavelength form is used the most frequently:

$$\boldsymbol{J = \int f_D(\lambda)\varepsilon_A(\lambda)\lambda^4 d\lambda} \tag{5}$$

Here, $\boldsymbol{\lambda}$ is the wavelength of the light (nm), $\boldsymbol{\varepsilon_A}$ is the molar extinction coefficient of the acceptor, (M^{-1} cm^{-1}), and $\boldsymbol{f_D(\lambda)}$ is the area-normalized fluorescence spectrum of the D [78].

In ideal dipole approximation (IDA), the donor is approximated as a group of oscillating charges contained within a sphere with a radius R_D and its center located in the center of this sphere. The acceptor, in turn, is also approximated as a sphere of oscillating charges around its center and with radius R_A. Thus, in the near zone, the distance between the D and the A is much larger than both R_D and R_A, and the IDA states that the electromagnetic interaction between D and A is a dipole–dipole interaction, and all interactions due to higher multipoles can be ignored [82]. D and A are considered oscillating (transition) dipoles.

In classic Förster theory, D and A are visualized as a group of coupled electrical oscillators. If the light can excite the donor, then D oscillators in an external electromagnetic field produced by that light will oscillate and cause their own electromagnetic field. Oscillators of the A often won't be sensitive to the electromagnetic field caused by the light, but may respond to the electric field from the D oscillators [78].

The approximation can be expressed as the following equation:

$$W_A = \begin{cases} 0 & , \text{if } \nu_D - \nu_A < \frac{-1}{2t} \\ \frac{q_e^2 E_D^2}{8m_E} \times t^2 & , \text{if } \frac{-1}{2t} < \nu_D - \nu_A < \frac{1}{2t} \\ 0 & , \text{if } \nu_D - \nu_A > \frac{1}{2t} \end{cases} \quad (6)$$

Here, W_A is the energy of the A dipole at the time t as a result of its interaction with the D field, ν_D is the frequency of the donor field, ν_A is the frequency of the acceptor field, E_D is the amplitude of the D electric field, t is the amount of time the electric field lasts, starting from 0.

For the resonance to occur, the electric field of the D should move in the direction that shares at least one component with the direction of the A field. The energy W_A depends on the frequency difference $\nu_D - \nu_A$ and has a strong maximum at $\nu_D - \nu_A = 0$, and weaker secondary maxima at other values. The approximation made by Förster suggested replacing this resonance wave by a sharp rectangular peak (resonance or nothing approximation) [78], [83]. The value of this peak strongly increases with time, while the width decreases. If the time doubles, the value at the peak increases four times, but the width decreases twofold.

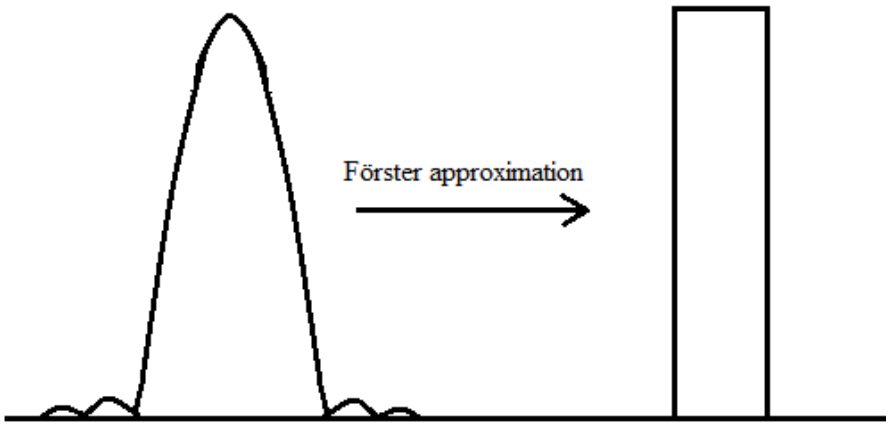

Figure 6. A schematic representation of Förster approximation. The energy of A is plotted vertically and the frequency - horizontally. Centers of both peaks correspond to the frequency of D being equal to the frequency of A [78].

2.2.2 Determination of FRET efficiency

The efficiency of FRET determines the relationship between the Förster distance of a D-A pair with the actual distance between D and A. It can be calculated using the quenching of the D, the sensitization of the A, or both of the factors, as well as by photobleaching of D or A. Efficiency of FRET can be calculated using Equation 1.

2.3 UCNP in bioapplications

2.3.1 Surface Modification of UCNP

Over the past decades a deeper understanding of nanomaterials has been achieved, which led to an expansion of their applications not only in science, but also in technology and medicine. Theranostics, an approach that combines analytical and therapeutic applications of nanoparticles to create individualized therapies for different diseases, presents a particular interest [24], [84].
UCNP appear to be attractive for such applications as diagnostics and phototherapy due to their intrinsic optical and photophysical properties listed in Table 1 and section 1.2.

There are a lot of available surface modification methods for achieving the desired design of the UCNP surface with different physico-chemical, biocompatible, and pharmacological properties, for various applications [22]. As-synthesized UCNP usually are hydrophobic, capped with, e.g. oleic acid, thus, the role of the ligand is to improve the biocompatibility of UCNP and simultaneously to protect it from the aqueous media [23]. Ideally, the ligand provides the hydrophilicity and a potential for labelling of the UCNP with specifically tailored groups to achieve desired physical, chemical or biological properties without compromising the initial photophysical properties of the UCNP [24].

Some common problems that can arise during the process of surface modification include instability in aqueous environments, aggregation and precipitation, batch-to-batch variability, and low quantum yields.

There are several ways to modify the surface of the UCNP: first, oxidation of ligands that already are on the surface of the UCNP using an oxidizer, e.g., ozone or Lemieux-von Rudloff reagent. In case of OA-capped UCNP, the double bond can be used to create carboxylates, aldehydes or epoxides [28], [71], [85]. Unfortunately, ligand oxidation is not used that frequently, because the solubility of the resulting of UCNP is insufficient, and the resulting functionalities are not very diverse [86]. [87] found out that using Lemieux-von Rudloff reagent for oxidation of oleate ligands for more than 2 h led to formation of luminescence-quenching MnO_2 and difficult to eliminate byproducts.

The second method is ligand exchange, where the hydrophobic ligands are replaced with hydrophilic ones with a higher affinity to the surface of the UCNP [88]. Usually the ligands on the as-synthesized UCNP are pretty labile and dynamically bind and unbind to the nanoparticle surface. Also, special measures should be taken to avoid aggregation and precipitation [89].
The usual UCNP capping agents, OA or oleylamine, are monodentate, and can be replaced by another monodentate ligands such as polyethylene glycol (PEG) or its modifications, which requires a molar excess of the desired ligand to shift the equilibrium towards the desired ligand. To improve the colloidal stability by reducing the rates of desorption of the ligand from the UCNP surface, polydentate ligands (e.g., citrate or alendronate) can be used [6], [28].

For example, in [90], the effect of different surface ligands on the photophysical properties of β- Yb^{3+},Er^{3+}-doped UCNP was studied in two groups of modified particles: by adding a layer on top of the OA capping and by replacing the oleate with a new ligand by means of ligand

exchange. Among the applied ligands were BF_4^-, trisodium citrate, polyacrylic acid (PAA), poly(isobutylene-alt-maleic anhydride) modified with dodecylamine (PMA) and its further modifications, and silica. All of them presented great colloidal stability, but their luminescence intensity in water dropped significantly compared to the original hydrophobic non-modified particles. Besides, all of the particles with an additional layer on top of OA presented a brighter green emission compared to the red one, which was not the case for the ligand exchange samples.

UCNP can also be hydrophilized by adding a layer of amphiphilic polymers on top of the capping agent, which can make the surface of UCNP available for biolabelling. Some studies have shown that using both synthetic- and bio- amphiphilic polymers allows to create bioapplicable probes based on UCNP [89], [91]. The use of phospholipids has also been reported [28], [92].

Another strategy, also illustrated in [90], is called layer-by-layer assembly (LbL), which initially was developed for the modification of planar surfaces and later extended its use to QD, and, eventually, UCNP [93], [94]. The approach is based on sequential coating of the surface of the particles with oppositely charged ligands. The technique is suitable for virtually any type of particle, and provides precise control over the thickness and content of the coating layer. The drawbacks include the necessity to use hydrophilic UCNP as a starting material, and the demanding and time consuming procedure [95].

The next option of UCNP modification would be the silanization, which can be used to modify both hydrophilic and –phobic UCNP. Besides being stable, biocompatible and optically transparent, silica also offers a selection of biolabelling techniques due to sufficient understanding of its surface chemistry [28], [89], [96]. There are several methods of applying an even layer of silica onto the surface of the UCNP, e.g. the microemulsion method, where hydrophobic nanoparticles are modified with a silica-containing chemical, for instance, tetraethoxysilane [97]. Another frequently used method, the Stöber method, implies controlled hydrolysis of the tetraalkoxysilanes, is mostly applied to create controllable silica particles, but can be modified to create layers of silica on surfaces of nanoparticles [98]. With certain modifications of the coating procedures and chemicals, the silica layer can be modified to create a biocompatible surface that can be readily decorated with, e.g., proteins [28].

The last option of hydrophilizing of UCNP involves “stripping” them of the OA (or equivalent) hydrophobic coating by subjecting them to incubation in slightly acidic solutions (e.g. HCl solution with pH 2-4), leading to protonation of oleates [99]. The resulting particles are soluble in water, don’t change their morphology and size, don’t aggregate, and continue to present luminescence. Such particles can be used as a unique platform for further surface functionalization. The only drawback is their limited stability, as $NaYF_4$ tends to dissolve in water overtime.

2.3.2 Bioconjugation of UCNP

Bioconjugation stands for the attachment of different biomolecules (antibodies, proteins, etc.) to UCNP with a modified surface to target specific recognition sites or to provide specific and

selective interactions [91]. Although the conjugation of biomolecules onto the surface of the UCNP can be performed in different ways, for instance, direct non-covalent binding of nucleic acids (negatively charged) to the positively charged surface of UCNP [99], the most commonly used technique is covalent binding via carboxylic and amine functionalities [28]. The majority of the UCNP – biomolecule coupling reactions are inherited from common protein conjugation reactions, such as amine-*N*-hydroxysuccinimydyl-ester or thiol-maleimide coupling [100].

Carboxylic acid functionalities are particularly attractive because they not only exhibit hydrophilic properties and high co-ordination, but also link pretty easily to the amine groups that are often present in biomolecules [101], [102]. Carboxyl groups also offer benefits for storage of modified UCNP in alkaline solutions, as the terminal hydroxyl group is deprotonated [24].
Some examples of using carboxyl groups on the surface of UCNP for bioconjugation include attaching single-stranded DNA to diethylenetriaminepentaacetic acid (used as the ligand on UCNP) [103], [104] and coupling streptavidin to azelaic acid (ligand), both performed via carbodiimide chemistry [102]. Carboxyl groups can even be used for creating multimodal theranostic probes, e.g. chitosan-coated UCNP were used in photodynamic therapy, as described by [105].

UCNP ligands containing amino groups also present an attractive platform for further biofunctionalization, because they make the UCNP hydrophilic and can be easily used in the well-known carbodiimide cross-linking protocol. They are positively charged at physiological pH which can be used in certain applications.

Amine-functionalized UCNP have been reportedly coupled to proteins, biotin, foilc acid, and oligonucleotides [28], [30], [106]–[108]. Biomolecules containing thiol groups can be linked to amine-modified UCNP with the help of sulfo-SMCC (sulfosuccinimidyl 4-(N-maleimidomethyl)cyclohexane-1-carboxylate), a heterobifunctional linker that is selectively reactive towards thiols on one end and to amines on the other [89]. Another heterobifunctional linker, namely, glutaraldehyde, can be used for amine-amine coupling [109].

Other bioconjugation strategies include disulfide linkage via a disulphide exchange reaction [110], biotin-streptavidin chemistry, cross-linking agents, and click chemistry [100]. The latter stands for a reaction that is modular, high yield, wide in scope and doesn't produce any toxic byproducts [111]. Besides, it should utilize simple conditions, available reagents, no solvent or a solvent that's biocompatible, and the isolation of the product should be made simple [100]. If the reaction fits all the criteria listed above, it can be called a click reaction. Click reactions offer high orthogonal reactivity, meaning that the two species with specifically paired functional groups are exclusively bonded to each other regardless of the presence of other functional groups. At the moment, several types of reactions, including some nucleophilic substitutions, cycloadditions, nonaldol carbonyl formation, and additions to C-C bonds (e.g. epoxidation) [100].

A special kind of click chemistry reactions is copper-free click chemistry, a cycloaddition which utilizes the reactivity of an azide group, adding it to a cyclooctyne. This kind of reaction doesn't require copper catalysts, which makes it non-toxic to living cells [112]. The azide group

is a popular chemical reporter due to being small, metabolically stable, and it also usually doesn't react with natural biofunctionalities [112]. The azide also offers unique chemistries with such bioorthogonal functionalities as, e.g., phosphines and alkynes. The Staudinger ligation (the reaction of azides with triarylphosphines equipped with an ester) was the first bioorthogonal reaction ever performed in a living system [113].

The azide group can be contained within the target biomolecule, e.g. [114], where protein–protein interactions were studied in non-ribosomal peptide biosynthesis by crosslinking domains using the second-generation difluorinated cyclooctynes on one domain and an azide on the other; or [115], where a reaction between a resin-immobilized non-fluorinated cyclooctyne with an azido-peptide was performed to purify complex mixtures for proteomic analysis. Another option is reversing the polarity of this reaction, e.g. [116], where a phospholipid was conjugated to OCT cyclooctyne and inserted into live cell membranes, later imaged with azido-coumarin [113].

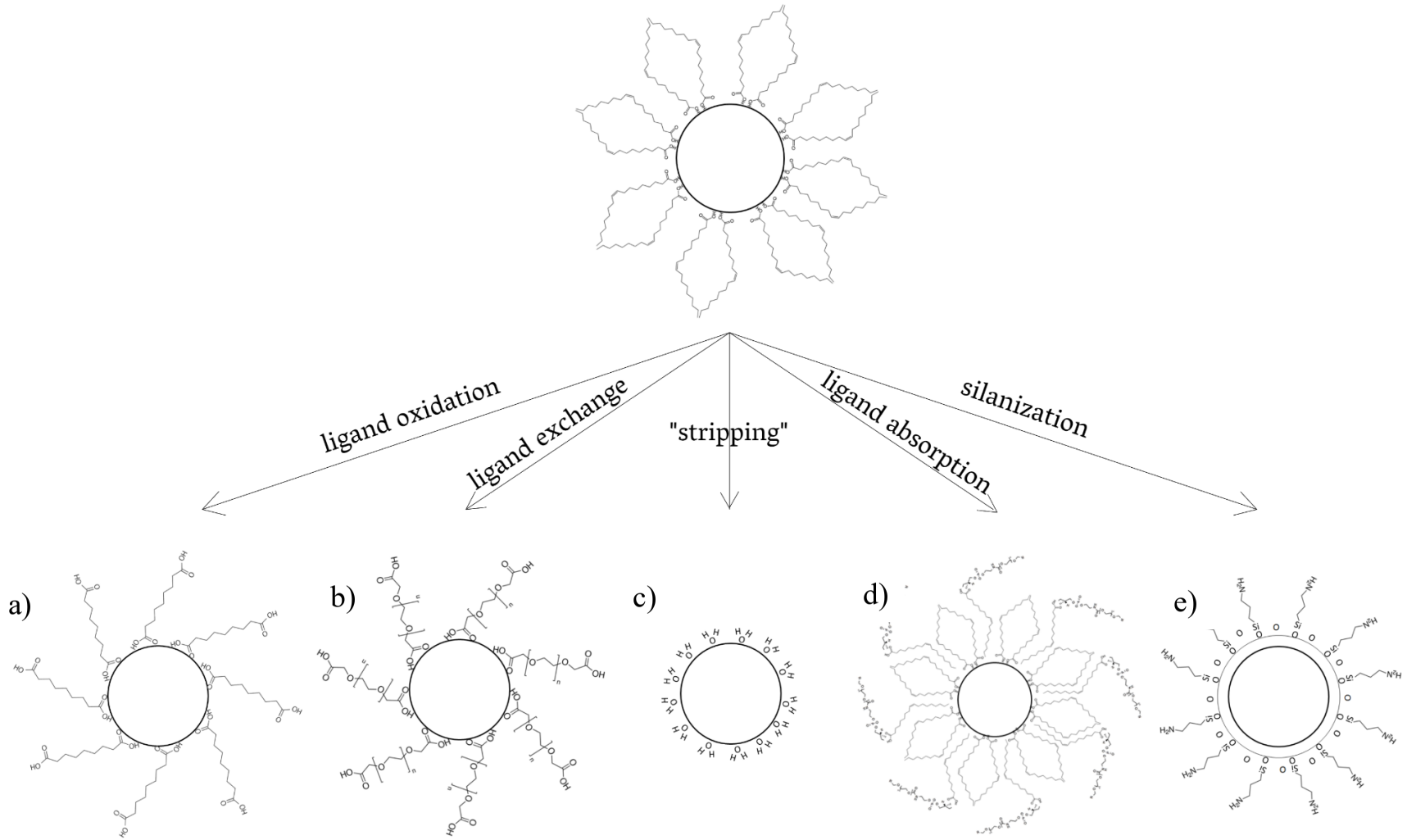

Figure 7. Examples of surface modification strategies of a hypothetical OA-capped UCNP (on top): (a) ligand oxidation of OA to azelaic acid; (b) ligand exchange of OA to PEG diacid; (c) “stripping” of the UCNP of OA to obtain ligand-free UCNP; (d) ligand absorption with PEG-phospholipids attached to the OA molecules; (e) silanization with the microemulsion strategy with further (3-aminopropyl)trimethoxysilane modification. Adapted from [28]

2.3.3 Bioassays

A bioassay is defined as a measurement of the potency of any stimulus by comparing its effect on biological material, e.g. animals, tissues, or living cells, with those of a standard product [117].

The interest in applications of UCNP *in vivo,* as well as *in vitro,* is mainly driven by their low toxicity and absorption in the NIR (or IR), as well as other outstanding properties listed in section 1.2 and Table 1.

Luminescence resonance energy transfer (LRET) assays using UCNPs as donors have been successfully implemented with organic dyes or QDs as acceptors or gold or carbon NP as quenchers with efficiencies up to 50 %, which has been significantly improved in the later studies [26], [28], [118]. The applications of UCNPs in bioassays include, but are not limited to, quantification or detection of proteins, nucleic acids, metabolites, hormones, and metal ions.

2.3.3.1 Nucleic acids

One of the earliest reported UCNP – assisted assay for nucleic acid detection compared the sensitivity of UCNP and a cyanine dye (Cy5) for detection of complementary DNA. Cy5 molecules were attached to avidin, which was, in turn, immobilized on the biotin-labelled DNA. UCNP modified with biotin were then used to label the avidin molecules. It was shown that the sensitivity of UCNP was 4 times higher than the sensitivity of the cyanine dye [119].

Some resonance energy transfer (RET)-based assays have also been reported. For instance, UCNP and an intercalated cyanine dye (SYBR Green I) as a donor-acceptor pair were used for the detection of DNA hybridization. Energy transfer only occurred after hybridization, which allowed to quantitatively measure the analyte. The limit of detection was reported to be 20 fmol, and the sensor was capable of differentiating between fully complementary target and a single base mismatched sequence [104].

Multiple luminescence bands characteristic for UCNP also found their application for dual parameter hybridization assay using two different acceptors (AlexaFluor 700 and 546). Two different DNA sequences were successfully detected with a detection limit of 28 fmol [25].

One more example of simultaneous detection is the rapid sandwich hybridization assay reported in [120], in which it was possible to detect DNA from enterovirus 71 and coxsackievirus A16. Immobilized DNA probe sequences (specific to each target) on respectively differently colored UCNP were brought in contact with capture sequences immobilized on magnetic beads upon the introduction of the target sequence, which allowed for quantification after separation and purification [28].

2.3.3.2 Proteins

Resonance energy transfer-based assays for protein detection have been reported in various studies. Among them, for example, implication of biotin-avidin chemistry for avidin detection using biotin-coated UCNP and gold NP, which approximated each other in the presence of avidin, leading to RET [107].

In [26], molecular beacon probes were implemented, locking a TAMRA dye in close proximity to UCNP, which lead to RET, for the detection of thrombin. The intensity reached 80%, and in presence of thrombin the beacon probes opened, which increased the distance between TAMRA and UCNP, and decreased the RET efficiency. The limit of detection reached 50 pM.

Another thrombin detection assay, where PAA-coated UCNP were used as donors and carbon NP as acceptors, was described in [121]. UCNP were modified with a thrombin-specific aptamer, which could bind to the surface of carbon UCNP, quenching UCNP emission by almost 90%. In the presence of thrombin, the aptamer bound to it, which led to the separation of UCNP and carbon NP, and the restoration of UCNP luminescence intensity.

Another example of UCNP applications for protein detection include a sandwich assay-based lateral flow test strip described in [122] used to simultaneously detect drugs such as amphetamine, phencyclidine, morphine and methamphetamine in human saliva, and a separate assay for the detection of *Escherichia coli*. The simultaneous detection could be achieved due to sorting and optical multiplexing, and detection limits were reported to be as low as 10^3 cfu/mL for *Escherichia coli* and 5 ng/mL for the drugs [28].

2.3.3.3 More biological targets

UCNP have been used in assays for the detection of various other substances. RET-based assays have also been used, e.g. for detection of estradiol [123] with detection limits of 0.4 nM in buffer and 0.9 nM in serum. In this assay UCNP were used as donors and a molecular dye called Oyster-556, bound to estradiol, as an acceptor. Another assay for hormone detection reported by [27] was able to recognize thyroid stimulating hormone, luteinizing hormone, and prostate specific antigen in buffer with limits of detection of 0.64 mU/L, 0.45 U/L and 0.17 ng/mL, respectively. UCNP were linked to antibodies, which were used to label the targets captured in streptavidin-coated microtiter wells.

UCNP-based RET has also been used to detect such metabolites as glucose with a detection limit of 0.025 μM, where rhodamine B isothiocyanate [124] or graphene oxide [125] were used as acceptors in pair with UCNP donors.

As an example of an assay that doesn't use RET, an aptamer-functionalized bioassay based on magnetic beads implementing UCNP as labels that detected a mycotoxin called ochratoxin A has been reported by [126]. In a following report, simultaneous detection of ochratoxin A and aflatoxin B_1, a carcinogenic compound also produced by fungi, was performed with optical multiplexing: respective antibodies for both toxins were immobilized on differently colored UCNP, while toxins were immobilized on magnetic nanobeads. Upon binding, UCNP and magnetic beads were brought together, and in case of introduction of ochratoxin A or aflatoxin B_1, a competition for sites occurred, resulting in separation of some UCNP-magnetic bead couples. The detection limit was claimed to reach 0.01 ng/mL in food samples [28].

2.4 Bioimaging using UCNP

2.4.1 Accessing the toxicity

Predicting the potential toxicity of UCNP presents a challenge due to their complexity compared, for example, to bulk materials. Nanoparticles exhibit biological and environmental behaviors that stem from a combination of such intrinsic properties as their chemical composition, surface chemistry and state, physical parameters such as size, shape, structure, agglomeration etc., environmental factors such as pH, ionic strength, dissolution rate, and temperature, and, finally, presence of other components or electromagnetic fields [39].

UCNP are typically considered chemically inert due to their photochemical and thermal stability. This is important, because the release of fluoride ions can lead to intracellular stress [127], and some Ln^{3+} ions have been linked to toxic effects [128].

Commercial $NaYF_4$:Yb^{3+}, Er^{3+} UCNP were tested for stability in acidic cellular compartments and a model system mimicking liposomal fluid in [129]. It was demonstrated that the amorphous YPO_4 forming on the surface of UCNP can lead to inflammation in cells. Another study proved the formation of Ln^{3+} phosphates upon $NaYF_4$:Yb^{3+}, Tm^{3+} UCNP aging in phosphate buffer at elevated temperatures (> 37ºC) by means of potentiometry, X-ray-photoelectron spectrometry, and fluorometry [130], [131]. These studies demonstrate the necessity to improve the surface/shell design of UCNP and the need to keep this aspects in consideration when performing *in vivo* experiments with UCNP [6].

There are also some studies that investigated the cytotoxicity of UCNP in cell lines, animals and plants. For example, in [41], the toxicity of $NaYF_4$-based UCNP in *Caenorhabaditis elegans* was accessed based on protein expression, life span, reproduction and growth rate. No adverse effects were observed, but the survival rate showed some effect at the end of the life cycle [28].

A study on the biodistribution in major organs showed that the majority of UCNP were naturally eliminated within a week [132]. Another study observed the blood circulation and biodistribution of UCNP in tumor induced mice and discovered that throughout the period of 40 days there is some accumulation in organs like spleen and liver, which, however, did not provoke any apparent signs of toxicity [33].

Another study on mice, however, suggested that after accumulating in liver and spleen, the UCNP leave these organs within three weeks. There was some accumulation in the intestinal tract, but within 115 days after injection only trace amounts were detected. The animals also didn't show any alteration in their physiological behavior compared to the control group [40].

2.4.2 Instrumentation

In order to implement UCNP in imaging, instruments that would comply with their specific photophysical properties should be developed [129]. The main challenge that is presented emerges from the non-linear power dependency of the upconversion luminescence intensity

due to the anti-Stokes multiphotonic absorption. That makes UCNP incompatible with the majority of the conventional fluorescence imaging systems [6].

Usually, a continuous wave 980-nm diode laser is used to attain optimal excitation power density and profile. A possible downside of such lasers, however, is the possibility of overheating the sample, which can be overcome by using a pulsed laser or by focusing the excitation light on a very small area [6].

Due to the lack of commercial systems, most research groups develop their own instruments, specifically modified for the desired applications. For example, in cellular studies, e.g., organelle staining, confocal microscopy is often implied for depth profiling of the UCNP emission. That allows to localize UCNP with high precision, for example, in nucleus staining experiments it allows to distinguish between the UCNP adsorbed on the nuclear membrane and those inside the nucleus [133]. Another study [29] used two external adjustable lasers coupled with fiber optics as excitation source, and an electron multiplying charge coupled device (EMCCD) as a detector, and the images taken by the EMCCD were superimposed with those taken at ambient light to localize the areas in the animals where UCNP have accumulated [28].

An interesting design was described in [134], [135]: optical tweezers were created to trap and manipulate individual UCNP, and later used them for temperature sensing around single cancer cells.

Unfortunately, many of those instruments are lacking proper characterization regarding the excitation power density and beam profile, which presents a problem when comparing findings of different groups to each other and makes it difficult to define the optimal settings [6].

2.4.3 Multi-color, targeted and multi-modal imaging

Targeted *in vivo* imaging using UCNP has been investigated by several research groups [29]–[31], and the importance of surface ligands for these processes has been underlined. For example, positively charged UCNP showed the most effective cellular uptake, followed by neutral and negatively charged UCNPs, which corresponds well with the fact that cell surface is normally negatively charged [136].

Various luminescence bands and the possibility to tune the emission color by varying the composition of Ln^{3+}-doped UCNP offers a possibility for multi-color imaging. For instance, a minimally invasive technique for monitoring lymphatic drainage in rats with the help of polyethylene glycol-modified UCNP emitting in red, blue and green has been described in [32]. UCNP of different colors were injected into different areas and imaged after 120 minutes, detecting their migration to the proximate lymph nodes. The sample volume didn't exceed 20 µL.

Multimodal imaging using UCNP (i.e., combination of UC luminescence with MRI or tomography) has also been studied [33]–[35]. In one study, UCNP containing a radioisotope ^{153}Sm and functionalized with polyphosphoric surface ligands were introduced into the blood stream of mice. Blood circulation time detected for those UCNP by means of both UCNP luminescence and single photon emission computed tomography was several times longer than

usual. In the study, UCNP were detected in the main arteries and the heart within half an hour after injection (against usual several minutes), and accumulated in liver and spleen only after that time [137].

2.4.4 Theranostics

Theranostics stand for the combination of diagnostics and therapy, and is a popular concept in cancer treatment: it implies simultaneous detection of a tumor, treatment and monitoring of the treatment process. Some groups have already reported using of UCNP for such applications.

In [138], thiol-PEG-amine coated core-shell UCNP were decorated with an HIV protein Tat, which is effective at nuclear translocation of recombinant fusion proteins, and later an anticancer drug doxorubicin was attached onto UCNP via physical adsorption. Nuclear delivery of these UCNP was tested on HeLa cells and tracked by a combination of MRI, upconversion luminescence, and fluorescent dyes. It was shown that doxorubicin alone entered the nucleus up to 6 times slower than with the presence of TAT. With this method, real-time monitoring of doxorubicin's action is possible.

UCNP can be used for photoinduced chemical release [36], [37], as in the study [38], where UCNP with a mesoporous silica shell bearing chlorambucil, a chemotherapy medication, were implemented to selectively release the drug in tumor-bearing mice.

Photodynamic therapy, minimally invasive and minimally toxic treatment for some types of cancers, can also implement UCNP. In [139], mice were injected with melanoma cells together with UCNP with two silica shells. In the second shell, two photosensitizers with absorption bands overlapping with the emission bands of UCNP, were doped, which produced singlet oxygen upon excitation at 976 nm. It was shown that the tumor development in mice with injected UCNP was much lower than that of the control group, which meant that UCNP can be used as both drug delivery and drug activating agent.

Despite the progress that has been made in the last decades in the design and bioapplications of UCNP, there are still a lot of issues to resolve. Namely, the upconversion luminescence efficiency, which usually doesn't exceed 1% for the majority of UCNP, presents a limitation for the applications, and requires the development of novel lattices. Precise basic characterization methods of the molar mass, extinction coefficients, and absolute quantum yield are also still to be developed. RET schemes including UCNP have been gaining increasing interest, but the precise mechanism of the process is yet to be completely understood. The surface modification procedures are numerous and require some organizing and consolidation. The multiplexing capacity of UCNP has been studied very fragmentarily, and there's a great potential for exploration and possible applications of this feature for detecting multiple analytes. Thirdly, the rapid uptake of UCNP by spleen and liver still remains a challenge for *in vivo* imaging. And lastly, in order to introduce UCNP to the market as medical or clinical agents, more systematic toxicity studies should be carried out.

That being said, UCNP are very promising as luminescent probes for bioimaging and bioapplications due to their unique photophysical properties, multimodality, stability and biocompatibility. They present a worthy alternative to such background-free detection systems

as radionuclides. RET-UCNP systems will also present a great potential for background-free assays upon achieving a better comprehension of the phenomenon [6], [28].

3 Experimental and characterization methods

3.1 Chemicals and Materials

3.1.1 List of used chemicals

All chemicals and organic solvents used in this work were of highest available grade and were used without further purification. All syntheses and analyses were performed using double distilled (DD) water with resistivity 18.2 MΩ·cm (25°C) obtained from Milli-Q® Advantage A10 Water Purification System (Merck, Germany), unless specified otherwise.

Chemical name	Company	Purity
1,2-dioleoyl-sn-glycero-3-phosphocholine (DOPC)	Avanti Polar Lipids	> 99%
18:0 azidoethyl phosphatidylcholine	Merck	99%
1-Octadecene	Merck	≥ 91.0 %
3-(N-Morpholino)propanesulfonic acid (MOPS)	Sigma-Aldrich	≥99%
3-(N-Morpholino)propanesulfonic acid, 4-Morpholinepropanesulfonic acid (MOPS)	Merck	≥ 99.5% (titration)
Acetone	VWR Chemicals	99.5%
Ammonium fluoride	Sigma-Aldrich	≥ 99.0 %
Cyclohexane	Sigma-Aldrich	99.5%
DSPE-PEG(2000)-DBCO	Avanti Polar Lipids	> 99%
Ethanol	Carl Roth	99.5%
Gadolinium(III) chloride hexahydrate	Sigma-Aldrich	> 99.9 %
Hydrochloric acid (HCl)	Merck	ACS reagent
L-α-phosphatidylcholine (Egg-PC)	Avanti Polar Lipids	> 99%
Oleic Acid	Sigma-Aldrich	90%
Sodium hydroxide	Carl Roth	99%
Therminol®66	FRAGOL GmbH+Co. KG	90%
Thulium (III) chloride hexahydrate	Sigma-Aldrich	> 99.9 %
Vybrant™ DiD Cell-Labeling Solution (DiD dye)	Thermo Fischer Scientific	99%

Ytterbium (III) chloride hexahydrate	Alfa Aesar	> 99.9 %
Yttrium (III) chloride hexahydrate	Sigma-Aldrich	> 99.9 %

3.1.2 Synthesis of Gd^{3+}-doped Upconverting Nanoparticles

Upconverting nanoparticles (UCNP) were synthesized by the thermal decomposition method, in which oleic acid (OA) was used as a capping agent and 1-Octadecene was used as a solvent [140]. In this method, lanthanide chlorides are added to a mixture of high boiling octadecene and oleic acid (volume ratio 3:2). To study the influence of different lanthanide ratios, the overall amount of lanthanide ions (Y^{3+}, Yb^{3+}, Tm^{3+} and Gd^{3+}) was kept constant (2 mmol), while Y^{3+} ions were replaced by Gd^{3+} ions. In a typical procedure, YCl_3 (30-70 % mol), $GdCl_3$ (10-50 % mol), $YbCl_3$ (18% mol), $TmCl_3$ (2 % mol), OA (15.6 ml) and 1-Octadecene (36 ml) were mixed together in a 50 ml 3-neck flask. After a clear solution was formed, the suspension is gradually heated to 145 °C under evacuation, which results in generating of Ln^{3+} oleates, and then cooled down to 45ºC. NaOH (0.3 g) and NH_4F (0.2 g) were added to the mixture under a counter stream of argon (Ar), which induced nanocrystal growth, and the solution was stirred until the precipitate dissolved. The reaction mixture was then rapidly heated to 310ºC min under gentle Ar flow to prevent the oxidation process. At these high temperatures, the process of Ostwald ripening (90 minutes) leads to the formation of highly crystalline nanoparticles (Figure 8): smaller particles dissolve, which supports the growth of larger particles. Heating was performed using an oil bath and a magnetic stirrer with a heating plate (Heidolph MR Hei-End, Germany) and temperature was controlled using a mercury-in-glass thermometer (Labortherm-N, Germany). Subsequently, the solution was cooled down to room temperature and the resulting UCNP were precipitated in 15 ml of ethanol, centrifuged (8000 rpm for 20 min, from Sigma Laborzentrifugen 2-15, Sigma, Germany) and then washed 3 times with ethanol. Finally, the UCNP were dispersed in 15 mL of cyclohexane for further use.

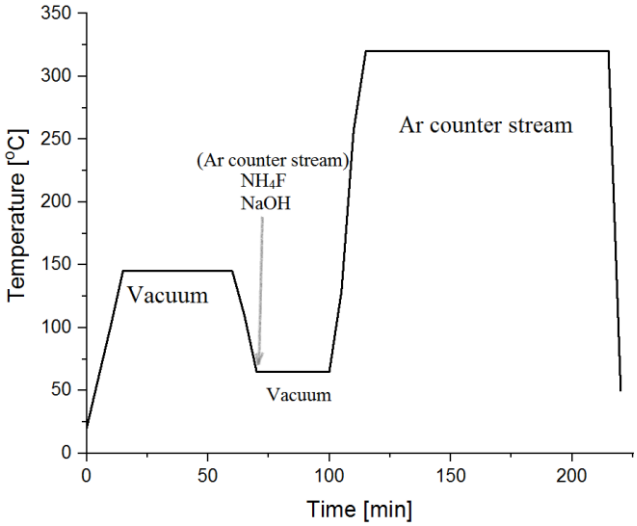

Figure 8. Reaction temperature profile as a function of time of the $NaYF_4$: Yb^{3+}, Tm^{3+}, Gd^{3+} UCNP synthesis.

3.1.3 *Synthesis of $NaYF_4:Yb^{3+},Tm^{3+}$ Upconverting Nanoparticles with Therminol®66 as a co-solvent*

All metal chlorides (YCl_3 (0.8 mmol); $YbCl_3$ (0.19 mmol) $TmCl_3$ (0.01 mmol)), $ErCl_3$ (0.005 mmol) OA (8 mL, 37.8 mmol) and Therminol®66 (12 mL) (volume ratio of Therminol®66 to OA was kept 3:2) were transferred into a 50-mL-three-necked-flask. The suspension was gradually heated to 145 °C under evacuation, generating Ln^{3+} oleates. After evacuating for 45 min at 140 °C, the reaction mixture was cooled down to 50 °C. Then, ammonium fluoride (NH_4F) (4.0 mmol) and sodium hydroxide (NaOH) (2.5 mmol) were added to the reaction mixture under a counter stream of argon (Ar) to induce nanocrystal growth. The flask was evacuated for 30 min at 50 °C until all solids were dissolved. After the added chemicals were dissolved, the reaction mixture was rapidly (heat rate: 25 °C/min) heated under a counter stream of Ar to 320ºC and stirred for 15 minutes (Figure 9). Precise temperature control was established using an electronic laboratory regulator with thermocouple (KM-RX1003, SAF, Germany) Then, the dispersion was cooled down to approximately 50 °C using a water bath. Purification was performed by adding 50 mL ethanol to the reaction mixture. The dispersion was divided equally into two centrifuge tubes (50 mL) and the particles were precipitated by centrifugation at 3100 g for 6-10 min. The precipitates were united and washed two additional times with ethanol (25 mL each time). The purified core-nanoparticle precipitates were re-dispersed in cyclohexane (15 mL to 20 mL).

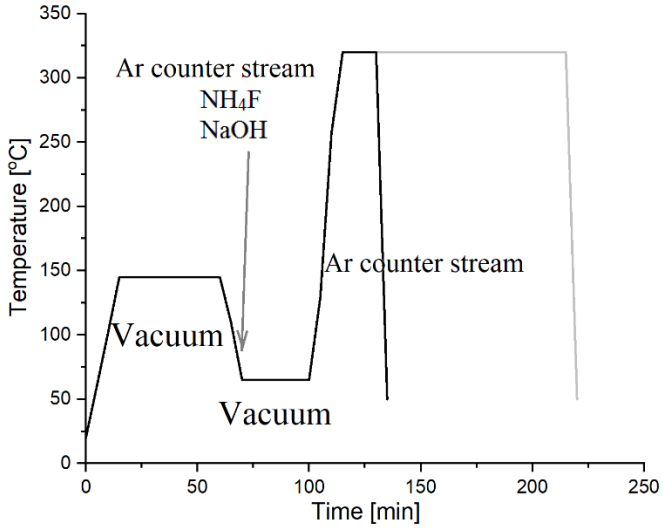

Figure 9. Reaction temperature profile as a function of time of the $NaYF_4:Yb^{3+},Tm^{3+}$ UCNP synthesis with Therminol® 66 as a co-solvent (black line). The older reaction profile (synthesis with octadecene as co-solvent) is shown in grey.

3.1.4 *Synthesis of shell precursor materials*

Metal chlorides (YCl_3; $YbCl_3$, $TmCl_3$) (depending on the shell type), OA (12.6 mmol, 4 mL) and Therminol®66 (8 mL) were transferred into a 50 mL-three-necked-flask, and heated to 140 °C for 45 min under vacuum. Then, reaction mixture was cooled down to 50 °C, sodium oleate (2.5 mmol) and ammonium fluoride (4 mmol) were added and evacuated while stirring at 50 °C for 30 min until no solids were left. The flask was then vented with Argon and the precursor material was stored in a refrigerator.

3.1.5 Synthesis of core-shell-UCNPs

60 mg of core-UCNPs dispersed in cyclohexane, OA (25.2 mmol, 8 mL) and Therminol (12 mL) were transferred into a 50-mL-three-necked-flask. Cyclohexane was removed by evacuation and heating to 75 °C for 30 min. The reaction mixture was vented with Argon, heated up to 305 °C (heat rate: 25 °C/min) and the shell-precursor material was added via slow injection method using a syringe pump (infusion rate: 2 mL/h, from Cole-Parmer® 200 Touch Screen Series Syringe Pumps). As soon as the syringe was empty, the temperature was maintained at 305 °C for additional 5 min. The reaction mixture was cooled down to approximately 75 °C using a water bath. Purification was performed by adding 50 mL ethanol. The particles were precipitated by centrifugation at 3100 g for 6-10 min. Purification was performed by washing two additional times with ethanol.

3.1.6 Synthesis of DBD-labelled fatty acid (DBD-6)

5-(8-decanoylbenzo[1,2-d:4,5-d′]bis-([1.3]dioxole)-4-yl)-5-oxopentanoic acid (DBD-6) was synthesized and kindly provided to us by L. John from the group of prof. P. Wessig of the Organic Chemistry Department of University of Potsdam. A schematic representation of the synthesis route is presented in Figure 10 [8].

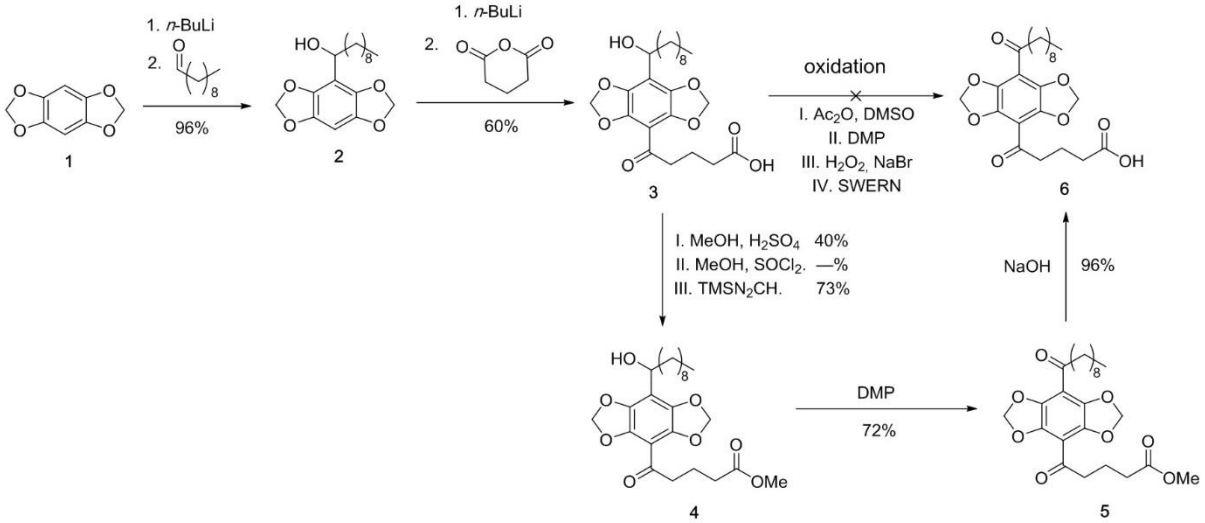

Figure 10. Synthesis of DBD- 6 [8].

3.1.7 Ligand exchange with DBD-6

For the ligand exchange reaction, the dye (2.5 mg) was dispersed in 10 mL cyclohexane. Respective volumes of UCNP solutions in cyclohexane were added and the mixture was incubated for 24 hours under vigorous stirring (600 rpm).

3.1.8 CMP-functionalization of UCNP

Before applying the polymer to the surface of UCNP, they needed to be stripped off oleic acid. For that, an aliquot of UCNP (e.g. 20 mg), was dispersed in 4 mL Milli-Q H_2O with pH 2 set with 0.1 M HCl. The mixture was sonicated (Sonorex Super RK 510 H, Bandelin, Germany)

for 1 h, then 12 mL of acetone was added to precipitate the nanoparticles and the mixture was centrifuged for 6 minutes at 3100 g. The precipitate has been washed twice with acetone and thereafter dispersed in 5 mL of MOPS buffer (pH 7.4, 0.1 M).

The ligand-free UCNP were then transferred to a plastic syringe (Braun Inject 10 mL), and slowly added dropwise into the polymer (CMP) solution in MOPS buffer (pH 7.4, 0.1 M) (10 mg polymer in 10 mL buffer) under vigorous stirring (600 rpm). The mixture was centrifuged for 6 minutes at 3100 g and thereafter washed with MOPS (pH 7.4) and DD H_2O. Finally, the precipitate was redispersed in 8 mL MOPS buffer (pH 7.4, 0.1 M).

3.1.9 Functionalizing of UCNP with phospholipids

Phospholipids were introduced to the OA-capped UCNP to create a single layer of lipids, where the hydrophobic tails of the lipid are oriented towards the hydrophobic OA-capped capped surface of the UCNP, and the hydrophilic parts face outside, rendering the resulting UCNP hydrophilic. For that, an aliquot of the UCNP (10 µL) was dried under the flow of nitrogen in a small glass vial, which was rotated to create a thin film on the walls of the vial. Then, 15 µL of DOPC lipid in ethanol and 15 µL of ethanol were added to the vial and mixed using a vortexer (PV-1, Grant Bio, United Kingdom). Thereafter, 500 µL of MOPS buffer (pH 7.4, 0.1 M) was introduced and the mixture was ultrasonicated for about 1-2 minutes. The resulting liposome-modified UCNP were stable in MOPS (pH 7.4) for up to 2 days, and could be stored for several weeks in the fridge without losing their colloidal properties (but it was necessary to repeat the sonication step before the experiment).

3.1.10 Preparation of the liposomes

The liposomes were prepared using L-α-phosphatidylcholine (Egg-PC), Vybrant™ DiD Cell-Labeling Solution (DiD dye) and (optionally) DSPE-PEG(2000)-DBCO. For the control sample, ethanol stock solutions of the DiD dye (4.82 µL, 7.9mM) and Egg-PC (62.5 µL, 24 mM) were added to a glass vial and dried under the flow of nitrogen to form a thin film on the walls. Afterwards, 300 mL of PBS buffer (pH 7.4) were added to the vial and vortexed until a milky solution was obtained. Thereafter, the solution was sonicated until clearing up, indicating the formation of the liposomes. For the sample used for click chemistry, the procedure was the same, except using 62 µL of Egg-PC and 5 µL of DBCO (3.25 µM). For the experiments the solutions were diluted according to the purpose of the experiment.

3.1.11 Copper-free click-chemistry bonding between the liposomes and UCNP

The reaction was performed according to the procedure described in [141]–[143]. Liposome samples labelled with DBCO or control samples without DBCO were incubated with N_3-containing CMP- or PL-coated UCNP for 1 to 2 hours in a plastic Eppendorf tube at room temperature and under mild shaking.

3.1.12 Cell preparation

HEK cells from the 293T line (ACC 305; DMSZ, Braunschweig, Germany) were cultured in Dulbecco's Modified Eagle Medium (DMEM) with the addition of fetal bovine serum (10%)

and l-glutamine (1%) and passaged every 3 d and no more than 10 times. All solutions, buffers, and media used for cell culture were purchased from PAN-Biotech (Aidenbach, Germany). 6 × 10^5 cells were seeded in 35-mm dishes (CellVis, Mountain View, CA) with optical glass bottoms 24 h before transfection. Madin-Darby canine kidney (MDCK) cells were seeded in 35 mm glass-bottom petri dishes 24 h before experiments were conducted, and allowed to grow to 80% confluency in full growth medium (10% fetal calf serum). The cells were transfected using TurboFect (Thermo Fisher Scientific, Waltham, MA) according to the manufacturer's protocol and used for microscopy starting at 2–4 h post-transfection.

3.2 Characterization methods

3.2.1 X-Ray diffraction

To study the crystal structure and the phase content of UCNP, X-ray powder diffraction (XRD) patterns were collected using a D5005 instrument (Siemens AG, Munich, Germany) in a range of 3-70°/2θ with divergence aperture, scattering ray aperture and graphite monochromatized CuKα radiation (λ = 0.15406 nm). The scanning step was 0.02°/2θ with a counting time of 4 s per step.

3.2.2 Transmission Electron Microscopy

Two transmission electron microscopes were used to estimate the size and morphology of the UCNP. The first one, JEM 1011 transmission electron microscope (Jeol Ltd, Tokyo, Japan) (TEM) using a wolfram hairpin cathode, an accelerating voltage of 80 kV and a molybdenum panel. The measurements were recorded using a side-mounted Olympus Mega View G2 (Olympus Germany GmbH, Hamburg, Germany).

The second microscope used was Tecnai G2 20, from FEI/Thermo Fisher Scientific) at an acceleration voltage of 200 kV. Samples were prepared by dropping diluted dispersions on carbon-coated copper grids (400 mesh). Particle counting was performed using ImageSP Viewer software.

3.2.3 Dynamic light scattering (DLS)

The hydrodynamic diameters of UCNP were determined by dynamic light scattering (DLS) using a Zetasizer Nano ZS (Malvern Instruments Ltd, Herrenberg, Germany) at 25°C with a detection angle of 173°. A He–Ne laser at 632.8 nm with P = 25mW was used as a light source.

3.2.4 UV/Vis absorption measurements / Spectrophotometry (Perkin-Elmer)

The UV/Vis absorption measurements of DBD-6 dye in cyclohexane were performed in a 1-cm quartz cuvette with a volume of 3 mL using a Lambda 750 UV/VIS Spectrometer from PerkinElmer. The absorption was scanned from 300 nm to 550 nm using a slit width and step width of 1 nm and recorded by operating UV WinLab Software (version 5.2.0). The baseline was corrected by measuring of absorption of neat cyclohexane.

3.2.5 Steady-state and time-resolved upconversion luminescence measurements at room temperature

Steady state and time resolved upconversion luminescence measurements were carried out at room temperature. The UCNP were excited at 976 nm using a wavelength tunable pulsed Nd:YAG laser (Quanta Ray, Spectra-Physics, Mountain View, CA) combined with an OPO system (GWU-Lasertechnik Vertriebsges.mbH, Erftstadt, Germany) operating at 10 Hz as excitation light source. All upconversion luminescence spectra were recorded using an intensified CCD-camera (iStar DH720-18V-73, Andor Technology, Belfast, Great Britain) coupled to a spectrograph (Shamrock SR 303i, Andor Tehcnology, Belfast, Great Britain)

equipped with a 600 L/mm grating. Time resolved luminescence spectra were recorded by applying a "boxcar" technique in which the amplitude $\boldsymbol{A_i}$ is converted to "true amplitude" $\boldsymbol{F_i}$ because of the dependence of $\boldsymbol{A_i}$ on the detection gate width $\mathbf{t_{gate}}$ [144]. Equation 7 shows this relation:

$$\boldsymbol{F_i} = \frac{\boldsymbol{A_i}}{\boldsymbol{\tau_i}\left(\mathbf{1} - \mathbf{e}^{-\frac{\mathbf{t_{gate}}}{\tau_i}}\right)} \tag{7}$$

where $\boldsymbol{F_i}$ is the coefficient by gate width $\mathbf{t_{gate}}$ correction, $\boldsymbol{A_i}$ is the experimental coefficient (amplitude of the fit function), $\mathbf{t_{gate}}$ is the detection gate width (duration of the photoluminescence emission recording), and $\boldsymbol{\tau_i}$ is the luminescence decay time of the i component. For fitting of recorded luminescence decay curves Equation 8 was used:

$$\boldsymbol{I}(\mathbf{t}) = \boldsymbol{y_0} + \boldsymbol{A_1}\mathbf{e}^{-\boldsymbol{k_1}\mathbf{t}} + \boldsymbol{A_2}\mathbf{e}^{-\boldsymbol{k_2}\mathbf{t}} \tag{8}$$

where $\boldsymbol{k_i} = \frac{\mathbf{1}}{\boldsymbol{\tau_i}}$ is the rate constant , $\boldsymbol{I}(\mathbf{t})$ is the luminescence intensity in dependence on time $\mathbf{t}$, $\boldsymbol{y_0}$ is the offset of the fitting function and accounts for background signal contribution, and $\boldsymbol{\tau_i}$ is the luminescence decay time of the i component.

The relative fractions $\boldsymbol{f_i}$ were calculated using the following equation:

$$\boldsymbol{f_i} = \frac{\boldsymbol{F_i}\,\boldsymbol{\tau_i}}{\sum_k \boldsymbol{F_k}\boldsymbol{\tau_k}} \tag{9}$$

3.2.6 Power-dependent measurements

To regulate the laser excitation power, a continuously variable neutral density filter (Ø100 mm, OD: 0.04 - 2.0, ThorLabs, New Jersey, US) was used. UC emission spectra of UCNP were measured with an intensity step of 5 mV (or 2 mV step at intensity powers lower than 10mV).

The results were plotted on Log Intensity – Log Power Density (P) plots and the number of absorbed NIR photons (n) per visible emitted photon were calculated from the slope of the linear least-squares curve through the data points (according to Equation 10) [9]:

$$\boldsymbol{I_{UC}} \sim \boldsymbol{I_{IR}^n} \tag{10}$$

Here, $\boldsymbol{I_{uc}}$ is the UC luminescence intensity and $\boldsymbol{I_{IR}}$ is the excitation power.

3.2.7 Low-Temperature Upconversion Measurements

The temperature-dependent steady-state upconversion luminescence measurements were recorded using a continuous wave fiber coupled laser diode working at 1000 mW (SHE-SP-975-160-FS-SMA, Laser 2000 GmbH, Wessling, Germany) coupled to a shutter in order to avoid the heating of the sample. In order to perform low-temperature luminescence measurements in a range of 4 K < T < 293 K, the UCNP colloidal solutions or powders were sealed inside glass tubes and placed on a copper sample holder in a vacuum chamber attached to a cold plate of a closed cycle liquid helium cryostat. The cryostat system consisted of a

helium compressor unit (Sumitomo Heavy Industries Ltd., Markt Indersdorf, Germany), a vacuum pump (Leybold vacuum Turbolab 80, Oerlikon, Köln, Germany) for the sample chamber, and a temperature controller (331 temperature controller, Lake Shore, Westerville, OH). The excitation light was focused directly on the samples. The upconversion luminescence emission was recorded using a lense system set in front of a fiber connected spectrograph (Shamrock SR-303i, Andor Technology, Belfast, Great Britain) equipped with an intensified CCD camera (iStar DH 720 18 V 73, Andor Technology, Belfast, Great Britain).

3.2.8 Estimation of the number of DBD-6 molecules per UCNP

To estimate the number of DBD-6 molecules per one UCNP, the dye absorption values of the supernatant solution were measured in samples with a fixed concentration of DBD-6 and decreasing concentrations of the UCNP.

The DBD-6 dye was dissolved in cyclohexane (0.02 mg/mL). To each 1 ml sample of the dye, 1.5 mL of UCNP with decreasing concentration (0.92; 0.46; 0.23; 0.092, and 0 mg/mL) was added. The mixtures were stirred overnight and centrifuged at 1500 g for 3 min. In the supernatant the absorption of the dye was measured and used to determine the amount of DBD-6 bound to the UCNP.

The following formula was used to estimate the number of dye molecules per UCNP:

$$\boldsymbol{n} = \frac{\frac{(c_0 - c_d) * v}{M_d} * N_a}{\eta(UCNP)}, \tag{11}$$

where c_0 is the starting concentration of the dye, c_d is the concentration of the dye in the supernatant, v is sample volume, M_d is the molar mass of the dye (434 g/mol), N_a is Avogadro constant ($6.02*10^{23}$), and $\eta_{(UCNP)}$ is the number of UCNP added to the sample, which was calculated according to [145]. Assuming that our UCNP are roughly spherical in shape, we used the following formula to calculate the mass of one UCNP:

$$m = \rho \pi r^3, \tag{12}$$

where ρ (g/cm^3) is the density of UCNP [145], and r is the average radius of one UCNP. Number of UCNP in one sample was calculated as the ratio between the mass of UCNP added to the sample to the mass of one UCNP.

Correction using control samples without the dye and baseline correction with pure cyclohexane were performed. UCNP concentration was held equal and constant for all spectral measurements of all samples.

3.2.9 Förster resonance energy transfer (FRET)

The Förster distance range of non-radiative energy transfer was estimated using the Equation 13 [78], [118]:

$$R_0 = 0.02108(\kappa^2 \Phi n^{-4} J)^{1/6} \tag{13}$$

where $\kappa^2 = 0.67$ (for dynamic averaging, which could be questioned in case of the donor being a part of a capping ligand) is the dipole orientation factor, Φ is the quantum yield of the donor, $n = 1.42$ is the refractive index of cyclohexane, and J (M^{-1} $cm^{-1}nm^4$) represents the spectral overlap between the area-normalized donor (Tm^{3+}) photoluminescence and acceptor (DBD-6) absorption spectra (see Equation 14):

$$\boldsymbol{J = \int_{430}^{500} f(Tm^{3+})\varepsilon_{DBD-6}\lambda^4 d\lambda} \quad (14)$$

3.2.10 Confocal imaging

Confocal imaging of the cells, liposomes, and UCNP was performed on a Zeiss LSM780 system (Carl Zeiss, Oberkochen, Germany) using a 40×, 1.2 numerical aperture water-immersion objective. Samples were excited with a 488-nm argon laser (YFP fluorophore) or a 663-nm diode laser (Card fluorophore). For two-color measurements, fluorophores were excited and detected sequentially for different regions of the spectrum. Excitation and detection light were separated using a 488/633-nm dichroic mirror. YFP fluorescence was detected between 499 and 595 nm, and mCardinal fluorescence was detected between 654 and 740 nm.

4 Results and discussion

4.1 Optimization of the synthesis procedure and properties of Yb^{3+}, Tm^{3+}, Gd^{3+}-doped $NaYF_4$-based UCNP

Despite the recent progress in synthesis and tuning of properties of lanthanide-doped UCNP, full understanding of the dopant concentration and shape/size influence on their luminescent properties is still far from complete. Evaluation of the influence of size, shape, crystalline phase, and dopant concentrations of UCNP have been performed by multiple working groups [9]–[14]. Among various procedures and methods to control the size and shape of lanthanide-doped UCNP is the tuning of Gd^{3+} concentration: doping of certain amounts of Gd^{3+} into the lattice seems to increase the prevalence of hexagonal crystal phase of UCNP and to decrease the size of UCNP without negative effects on the upconversion efficiency [10], [146], [147]. Thus, this chapter will focus on the effects of various doping concentrations of Gd^{3+} on the photophysical properties of $NaYF_4$:Yb^{3+},Tm^{3+} UCNP and the development of these properties with time.

A one-pot thermal decomposition method with oleic acid as a capping agent was used to synthesize the UCNP, as described in chapter 3.1.2 [140].

$NaYF_4$:Yb^{3+}(18 mol%),Tm^{3+}(2% mol) nanoparticles were synthesized with an addition of 10, 20, 30, 40 and 50 mol% Gd^{3+}, respectively. Gd^{3+} ions replace Y^{3+} ions in the crystal lattice of UCNP. The photophysical properties of the resulting 5 species of UCNP were investigated to determine the influence of Gd^{3+} content.

Stability of $NaYF_4$-based UCNP in water has been a subject of study for several research groups and anisotropic structural disintegration of the UCNPs over time has been shown [131], [148], [149]. But the behaviour of UCNP in dry phase or hydrophobic solvents, to our knowledge, has not yet been reported elsewhere. Thus, a comparison of structural and photophysical properties of $NaYF_4$: Yb^{3+}, Tm^{3+}, Gd^{3+} (10-50 mol%) right after synthesis and 24 months later has been performed. In the meantime, the UCNP were stored in cyclohexane.

4.2 *Ageing behaviour in $NaYF_4$:Yb^{3+},Tm^{3+},Gd^{3+} (10-50 mol%) UCNP stored in cyclohexane*

4.2.1 Basic characterization

The crystalline structure of as-synthesized UCNP was investigated using X-Ray powder diffraction (XRD). For $NaYF_4$, cubic (isotropic, or α-phase) and hexagonal (anisotropic, or β-phase) are known. As can be seen from Figure 11 , the XRD diffractograms have shown the presence of both phases in all UCNP samples, but the cubic phase was dominant at every Gd^{3+} concentration. The increase in Gd^{3+} concentration didn't seem to influence the phase content of UCNP, which differs from the data reported in literature for Er^{3+}-doped nanoparticles [10], [59], [150], [151]. It is now widely accepted that the increase in Gd^{3+} content in the lattice of $NaYF_4$ UCNP leads to smaller particles and a hexagonal crystal structure at high Gd^{3+} doping concentrations (up to fully replacing the Y^{3+} in the lattice).

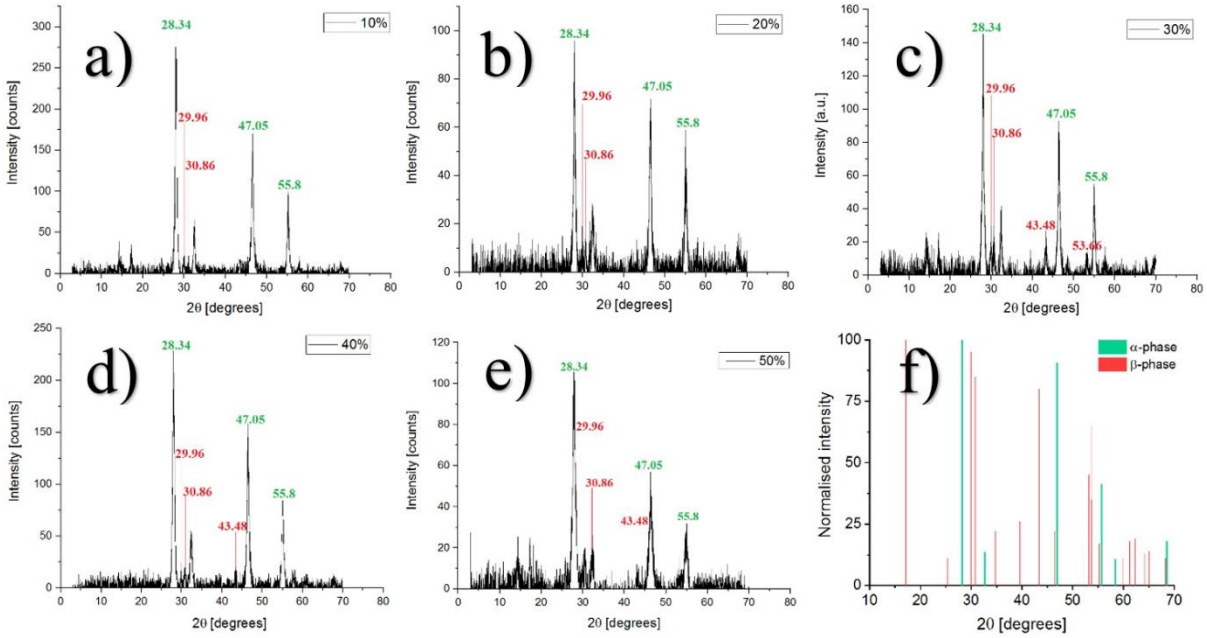

Figure 11. X-ray powder diffractograms of $NaYF_4:Yb^{3+},Tm^{3+},Gd^{3+}$ (10-50 mol%) UCNP (a-e). Reference XRD reflection data origin from JCPDs No. 01-077-2042 (-$NaYF_4$) and JCPDs No. 00-028-1192(-$NaYF_4$) (f). Green lines and numbers indicate α- and red - β- phase.

The crystalline structure of aged UCNP was also investigated using X-Ray powder diffraction (Figure 12). As with the freshly synthesized samples, both α- and β crystal phases were present in diffractograms of all UCNP samples independently from Gd^{3+} concentration with a more prominent presence of the cubic phase compared to the as-synthesized UCNP.

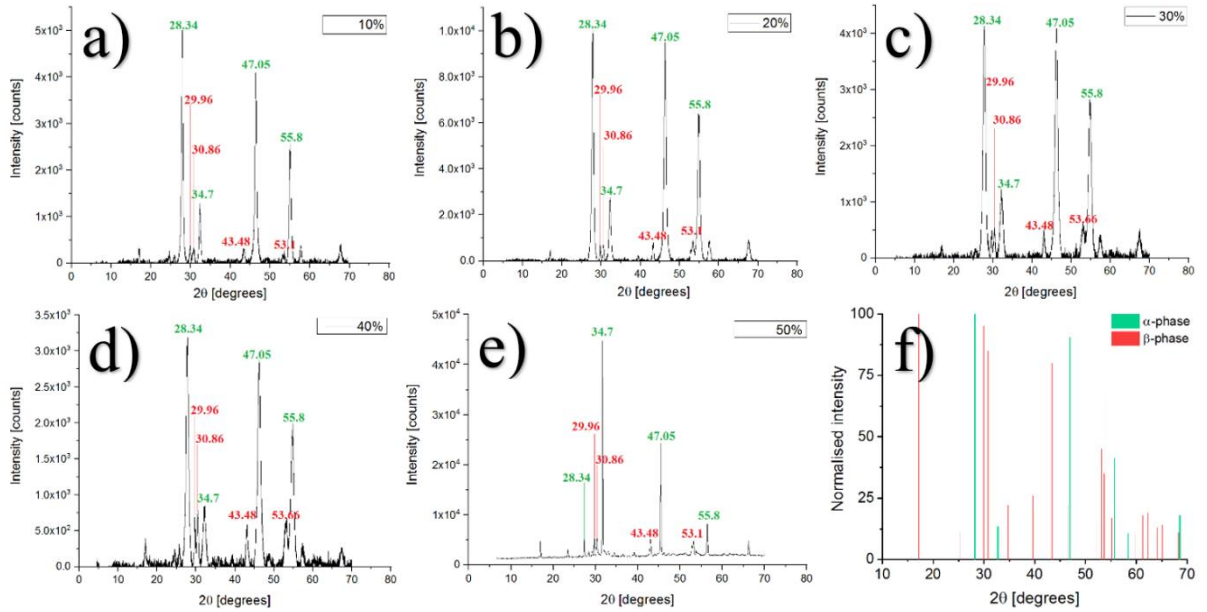

Figure 12. X-ray powder diffractograms of 24-month-old $NaYF_4:Yb^{3+},Tm^{3+},Gd^{3+}$ (10-50 mol%) UCNP (a-e). Reference XRD reflection data origin from JCPDs No. 01-077-2042 (-$NaYF_4$) and JCPDs No. 00-028-1192(-$NaYF_4$) (f). Green lines and numbers indicate α- and red - β- phase.

Transmission electron microscopy (TEM) was applied to determine the size and shape of the UCNP. The results can be seen in Figure 13: there were two sub-species in all samples except

for the Gd^{3+} (30 mol%) sample. The smaller sub-species had a round (or hexagonal) form and was more homogenous in size and shape. The larger sub-species had a shape of a 4-petal flower and was much larger and more diverse in size. In the sample with 30 mol% Gd^{3+} content, only the fine sub-species was present, and its diameter was the smallest among all samples (Table 2).

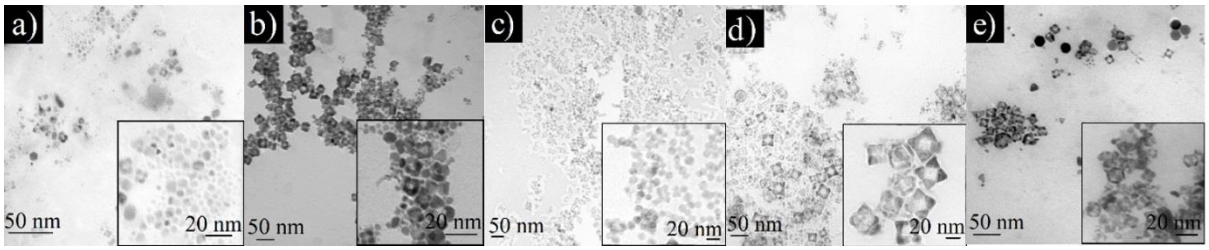

Figure 13. TEM micrographs of $NaYF_4$:Yb^{3+},Tm^{3+},Gd^{3+} (10-50 mol%) UCNP (a-e). The scale bars are 50 and 20 nm, respectively (acceleration voltage 200 kV).

Crystalline state and size of the aged UCNP were also monitored using TEM micrographs. As can be observed in Figure 14, the overview images show more clustering and aggregation of the UCNP. The particles still consisted of 2 fractions: finer, more homogenous hexagonal subspecies and larger, more diverse in size and shape, cubic sub-species. The 4-petal structures were also present after 24 months.

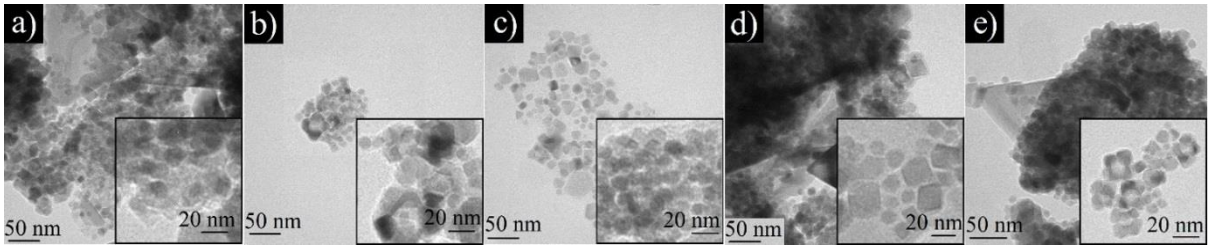

Figure 14. TEM micrographs of 24-month-old $NaYF_4$:Yb^{3+},Tm^{3+},Gd^{3+} (10-50 mol%) UCNP (a-e). The scale bars are 50 and 20 nm, respectively (acceleration voltage 200 kV).

Dynamic light scattering (DLS) measurements were conducted as an additional method to determine the sizes of studied UCNP. Data on the crystalline size obtained from XRD were also considered. To obtain nanocrystal sizes (D) from the X-ray diffractograms, Williamson-Hall equation was used:

$$\Delta q(q) = k \cdot \frac{2\pi}{D} + \varepsilon' \cdot q; \qquad q = \frac{4\pi}{\lambda} \cdot sin\theta, \tag{15}$$

where D is the diameter of the nanocrystallite, k is the shape factor of particle morphology (here 0.9), λ is the wavelength of the X-ray, ε'corresponds to variations of lattice constant of an infinite number of crystallites, θ is the Bragg angle of the diffraction peak and Δq is the full width at half maximum of the diffraction peaks as a function of q. The crystallite size D was obtained from the reciprocal of the intercept: $D = 2k\pi/\Delta q_0$.

The results are presented in Table 2. It can be seen that, given the margin of error, the crystalline sizes determined by XRD are in good agreement with the sizes of smaller sub-species calculated from TEM micrographs. The sizes determined by DLS appear to be larger, but it is

worth mentioning that the yielding diameters obtained by DLS are hydrodynamic, which means that they include the solvation shell around the particles. It may be noted that the size of the "fine" species determined by TEM correlates well with the crystallite size measured by XRD, while the "large" species correspond to the sizes determined by DLS. The explanation for this might be that the "fine" species consist of single crystals, while the multicristallite "large" ones have more impact on DLS data due to the specifics of the measurement method.

Table 2. Distributions of $NaYF_4$:Yb^{3+},Tm^{3+},Gd^{3+} (10-50 mol%) UCNP diameters as calculated from TEM micrographs, DLS and XRD analyses.

Sample		Content of Gd^{3+}, mol %				
		10	20	30	40	50
Particle size (TEM), nm	fine	23±4	23±4	13±1	17±3	23±6
	large	30±3	31±3		30±6	42±9
Particle size (DLS), nm		37±9	38±11	22±6	30±8	50±8
Crystallite size (XRD), nm		21±3	18±2	11±4	16±2	19±2

As can be seen from the data shown above, the concentration of Gd^{3+} ions in nanoparticles didn't have any linear relationship with the sizes or crystalline phase content of $NaYF_4$: Yb^{3+}, Tm^{3+}, Gd^{3+} (10-50 mol%) UCNP. The sample that was most homogeneous in size and shape contained 30 mol% Gd^{3+} ions. It also seemed to have slightly more pronounced β-phase-ascribed peaks on the X-ray diffractogram.

Table 3. Distributions of $NaYF_4$:Yb^{3+},Tm^{3+},Gd^{3+} (10-50 mol%) UCNP diameters after 24 months as calculated from TEM micrographs and XRD analyses.

Sample		Content of Gd^{3+}, mol%				
		10	20	30	40	50
Particle size (TEM), nm	fine	13±4	15±4	13±4	13±3	11±2
	large	28±3	26±3		29±4	34±4
Crystallite size (XRD), nm		17±2	16±2	12±2	15±3	16±3

As can be seen from the UCNP size distribution data obtained from XRD and TEM, compared in Table 3 after 24 months of incubation the diameters of almost all samples seemed to slightly decrease. This was especially true for the fine sub-species, the diameter of which in some samples decreased almost in half. The data obtained from XRD were in good agreement with the diameters calculated from TEM micrographs, the size of the "fine" species corresponding

to the crystallite size. The decrease in the sizes of smaller species could be caused by some Ostlwald-like ripening processes. Unfortunately, dynamic light scattering measurements could not be properly executed due to the presence of large UCNP clusters.

4.2.2 Upconversion luminescence properties

The upconversion luminescence spectra of oleic acid – capped as-synthesized $NaYF_4:Yb^{3+},Tm^{3+}$ upconverting nanoparticles dissolved in cyclohexane and upon excitation at 976 nm usually show three most prominent luminescence bands centered in 451 ($^1D_2 \rightarrow {}^3F_4$ transition, B1), 481 ($^1G_4 \rightarrow {}^3H_6$ transition, B2), and 800 ($^3H_4 \rightarrow {}^3H_6$ transition, NIR) nm.

Luminescence spectra of all the samples containing different Gd^{3+} concentrations were recorded for the aforementioned luminescence bands, a typical spectrum is shown on the example of the 30 mol% Gd^{3+} sample (Figure 15), as it had higher signal-to-noise ratio (all spectra are shown in the Supporting Information section, Figure 55).

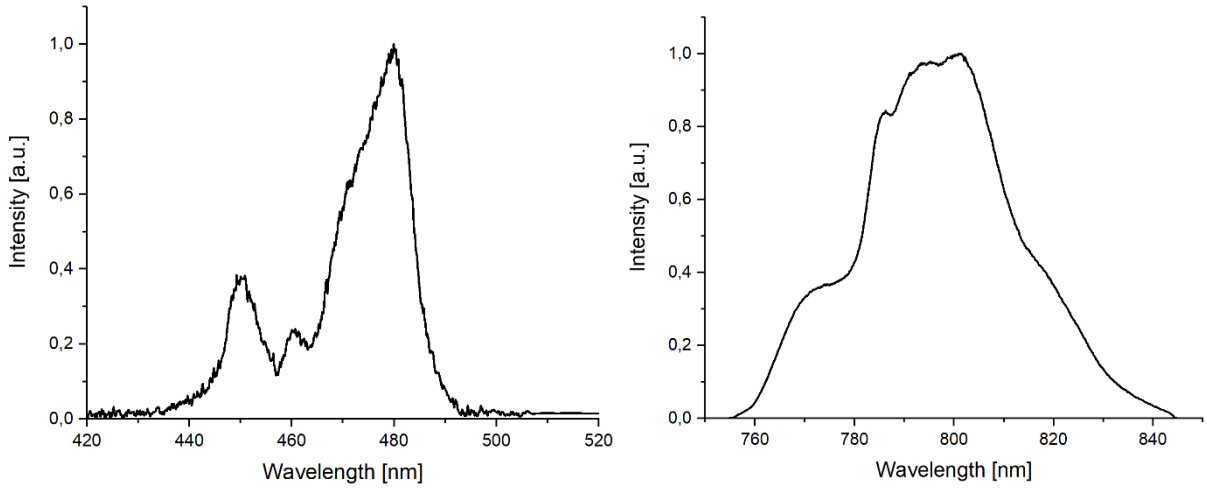

Figure 15. Upconversion emission intensities of $NaYF_4:Yb^{3+},Tm^{3+},Gd^{3+}$ (30 mol%) UCNP upon pulsed excitation (laser power 66.2 mW) at 976 nm. Blue (B1) and (B2) (left) and near-infrared (NIR) (right) emission bands are shown.

It is difficult to compare absolute intensities of the luminescence spectra between samples, as the concentration somewhat varies from sample to sample, and the experimental conditions can affect the outcome as well. Thus, a parameter that can be used to estimate the influence of the doping concentration can rather be emission band ratio. The higher signal-to-noise ratio of the 30 mol% Gd^{3+} sample could be attributed to its homogeneity in size and shape.

For all 24-month-old UCNP samples (10-50 mol% Gd^{3+}), upconversion luminescence spectra were recorded for the same luminescence bands: at 451 ($^1D_2 \rightarrow {}^3F_4$ transition, B1), 481 ($^1G_4 \rightarrow {}^3H_6$ transition, B2), and 800 ($^3H_4 \rightarrow {}^3H_6$ transition, NIR) nm. An example of such emission spectra of the of the sample with 30 mol% Gd^{3+} is shown in Figure 16 (all spectra are shown in the Supporting Information section, Figure 56).

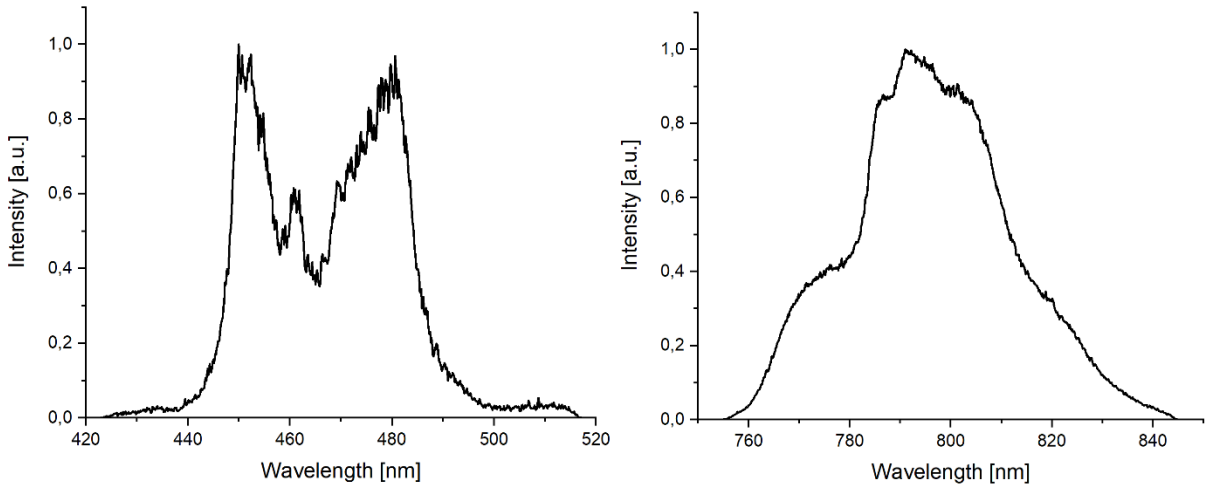

Figure 16. Upconversion emission intensities of 24-month-old $NaYF_4:Yb^{3+},Tm^{3+},Gd^{3+}$ (30 mol%) UCNP upon excitation at 976 nm upon pulsed excitation (laser power 71.4 mW). Blue (B1) and (B2) (left) and near-infrared (NIR) (right) emission bands are shown.

The signal-to-noise ratio of UCNP with 30 mol% Gd^{3+} ions still seemed to be the highest in both blue and NIR emission bands after 24 months of incubation. As in freshly synthesized UCNP, there was no linear connection between the concentration of Gd^{3+} and the upconversion efficiency of the UCNP. It can be noticed (Figure 56), that in the 30 mol% Gd^{3+} species the shape of the blue band is different from the rest of the species: the B1 band, corresponding to a 4-photon process ($^1D_2 \rightarrow {}^3F_4$), shows much higher intensity, which is also higher than the same band of the freshly synthesized UCNP 30 mol% Gd^{3+} (Figure 15). This could be due to the decrease of surface-to-volume ratio in aged UCNP due to more clustering compared to the freshly synthesized nanoparticles.

Interestingly, when the intensity ratios between the luminescence bands (B1/NIR and B2/NIR) were compared in the freshly synthesized UCNP, an almost Gaussian dependence on the Gd^{3+} content was revealed (Figure 17). The B1 band, corresponding to a 4-photon process ($^1D_2 \rightarrow {}^3F_4$), is expected to be the most sensitive to changes in content and structure of UCNP, while the 3-photon B2 ($^1G_4 \rightarrow {}^3H_6$) and 2-photon NIR ($^3H_4 \rightarrow {}^3H_6$) bands can better withstand variations in such parameters.

In 24-month-old UCNP, intensity ratios of B1 ($^1D_2 \rightarrow {}^3F_4$), and B2 ($^1G_4 \rightarrow {}^3H_6$) bands to the NIR ($^3H_4 \rightarrow {}^3H_6$) band have dropped compared to the as-synthesized UCNP. The dependence of B1 and B2 to NIR ratios on Gd^{3+} content couldn't be described by a Gauss fit anymore, but the ratios still peaked at 30 mol%. The 10 mol% and 50 mol% samples have shown the least difference between the as-synthesized and 24-month-old samples.

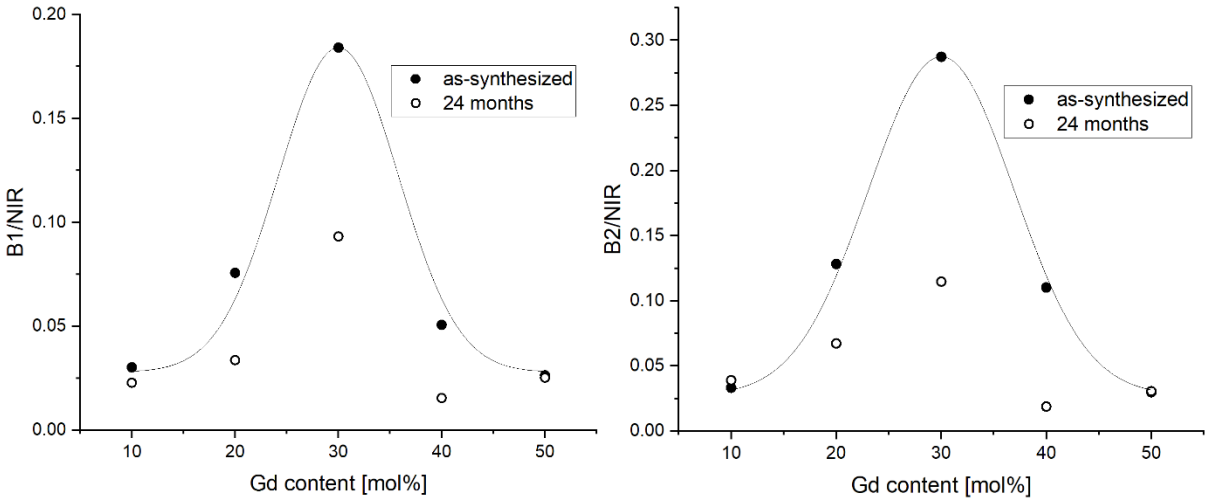

Figure 17. Intensity ratios of B1/NIR (left) and B2/NIR (right) luminescence bands of $NaYF_4:Yb^{3+},Tm^{3+},Gd^{3+}$ (10-50 mol%) UCNP upon excitation at 976 nm.

4.2.3 Luminescence decay kinetics

Subsequently, luminescence decay kinetics of the B1, B2 and NIR transitions were studied for all five $NaYF_4:Yb^{3+},Tm^{3+},Gd^{3+}$ (10-50 mol%) UCNP. The luminescence lifetimes of all UCNP were in the range of tens to hundreds of microseconds (Table 4). The data was analyzed using a biexponential decay law (Figure 18), Equation 8, and the relative fractions f_i were calculated using Equation 9.

The complex decay kinetics can be attributed to the presence of two different populations of luminescent Tm^{3+} ions: the ions located on the surface of UCNP (τ_1) are more susceptible to quenching due to surface defects and by solvent molecules with high-energy vibrations; while the ions lying in the bulk phase of the nanoparticle (τ_2) are more protected from the mentioned phenomena and usually display longer decay times [75], [152].

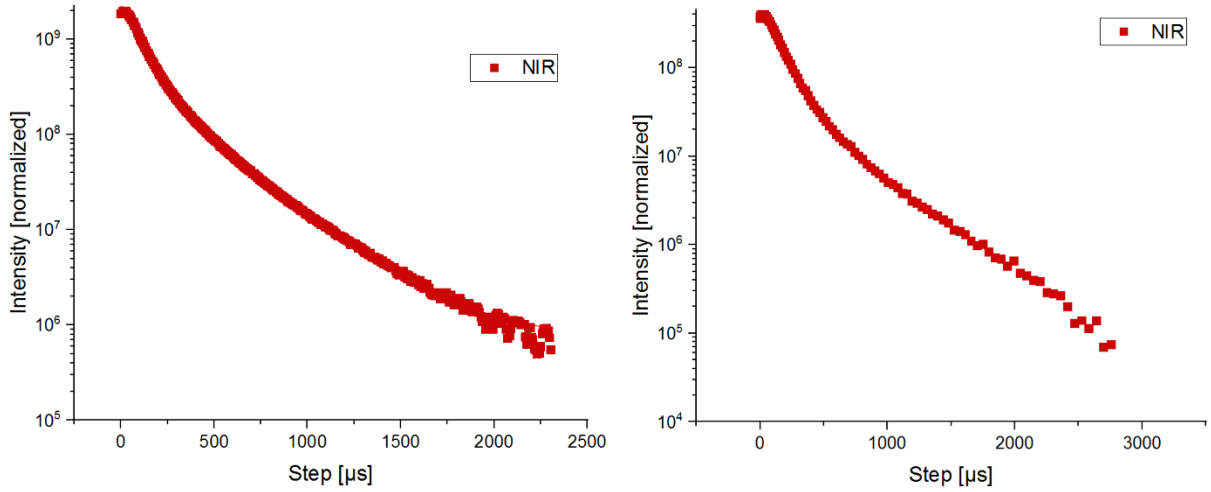

Figure 18. Normalized UC luminescence decay kinetics of the Tm^{3+} NIR emission band (800 nm) of as-synthesized (left) and 24-month-old (right) $NaYF_4:Yb^{3+},Tm^{3+},Gd^{3+}$(30 mol%) UCNP excited at 976 nm, initial delay Δt = 500 ns. The peaks were integrated within the full width at half maximum range.

On average, all samples, except the UCNP with 50 mol% of Gd^{3+}, displayed a higher fraction of the short luminescence decay component. As with the size, there was no clear trend in luminescence lifetimes with the increase of Gd^{3+} content, furthermore, particles with 30 mol% of Gd^{3+} presented relatively long lifetimes. This is somewhat surprising, since their average diameters were also the smallest, thus, the heightened surface/volume ratio would likely facilitate surface-related quenching effects. This phenomenon could probably be counterbalanced by the regularity of the 30 mol% Gd^{3+} - species crystallinity also resulting in homogeneity of size and shape of UCNP.

Table 4. Luminescence decay times with respective fractions (in parentheses) of Yb^{3+},Tm^{3+},Gd^{3+}-doped $NaYF_4$ UCNP upon 976 nm excitation (as calculated from PL decay curves, e.g., in Figure 18). τ_1 is the short component of the luminescence decay time, τ_2 is the long component and τ_{av} is the average time of luminescence decay.

Emission band with respective transition	τ, μs	Content of Gd^{3+}, mol%				
		10	20	30	40	50
451 nm $^1D_2 \rightarrow {}^3F_4$	τ_1	49 (90%)	47 (67%)	63 (69%)	52 (89%)	28 (47%)
	τ_2	155 (10%)	166 (33%)	216 (31%)	175 (11%)	178 (53%)
	τ_{av}	**61**	**87**	**110**	**66**	**109**
481 nm $^1G_4 \rightarrow {}^3H_6$	τ_1	64 (66%)	50 (68%)	66 (64%)	57 (74%)	38 (35%)
	τ_2	176 (34%)	159 (32%)	201 (36%)	171 (26%)	296 (65%)
	τ_{av}	**102**	**85**	**115**	**87**	**206**
800 nm $^3H_4 \rightarrow {}^3H_6$	τ_1	69 (84%)	69 (84%)	85 (69%)	51 (86%)	111 (41%)
	τ_2	190 (16%)	191 (16%)	288 (31%)	136 (14%)	352 (59%)
	τ_{av}	**88**	**88**	**147**	**63**	**254**

Luminescence decay kinetic investigation was the final step of analyzing the properties of 24-month-old $NaYF_4$:Yb^{3+},Tm^{3+},Gd^{3+} (10-50 mol%) UCNP. In general, luminescence lifetimes have significantly increased, especially for the UCNP with 10 and 20 mol% of Gd^{3+} (Table 5). The changes in surface-to-volume ratios due to the clustering of UCNP could be the reason for such drastic changes. The majority of the samples (except the 30 mol% of Gd^{3+}) displayed luminescence decay behaviors best described by the biexponential decay function. The fraction of the short luminescence decay component (τ_1), attributed to the ions located on the surface of UCNP, was still higher in the majority of samples.

The attempt to analyze the resulting data using a global fit (i.e. setting common decay times τ_1 and τ_2 and only leaving the coefficients A_1 and A_2 as individual decay parameters) yielded a rather random distribution of relative fractions. Hence, we plotted average decay times τ_{av} of all samples for both as-synthesized and 24-month-old UCNP as a bar diagram according to Gd^{3+} content for better visualization (Figure 19).

Table 5. Luminescence decay times with respective fractions (in parentheses) of 24-month-old Yb^{3+},Tm^{3+},Gd^{3+}-doped $NaYF_4$ UCNP upon 976 nm excitation (as calculated from PL decay curves, e.g., Figure 18). τ_1 is the short component of the luminescence decay time, τ_2 is the long component and τ_{av} is the average time of luminescence decay.

Emission band with respective transition	τ, μs	Content of Gd^{3+}, mol%				
		10	20	30	40	50
451 nm $^1D_2 \rightarrow {}^3F_4$	τ_1	366 (88%)	251 (60%)	260	58 (79%)	48 (56%)
	τ_2	1610 (12%)	637 (40%)	260	245 (21%)	272 (44%)
	τ_{av}	**516**	**404**	**260**	**98**	**146**
481 nm $^1G_4 \rightarrow {}^3H_6$	τ_1	827 (27%)	329 (58%)	275	55 (75%)	45 (48%)
	τ_2	2077 (105%)	937 (42%)	275	174 (25%)	233 (52%)
	τ_{av}	**1338**	**585**	**275**	**84**	**142**
800 nm $^3H_4 \rightarrow {}^3H_6$	τ_1	1087 (72%)	497 (71%)	127 (79%)	29 (84%)	132 (56%)
	τ_2	3695 (28%)	1847 (29%)	432 (21%)	108 (16%)	408 (44%)
	τ_{av}	**1809**	**895**	**191**	**41**	**253**

As can be noticed in Figure 19, in as-synthesized UCNP average decay times were increasing with the increase of Gd^{3+} mol%. The trend was reversed after 24-month-long incubation. The absolute values were also much higher in the aged samples.

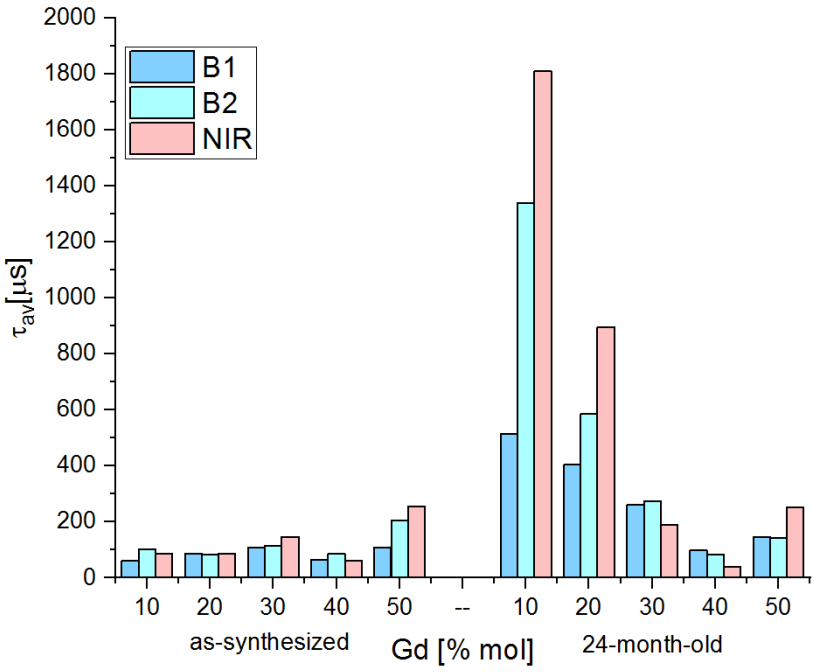

Figure 19. Average luminescence decay times of as-synthesized (left) and 24-month-old (right) $NaYF_4:Yb^{3+},Tm^{3+},Gd^{3+}$ (30 mol%) UCNP

4.2.4 Low-temperature upconversion luminescence studies

The effect of temperature change from 4 K to 290 K on the photoluminescence of the as-synthesized $NaYF_4:Yb^{3+},Tm^{3+},Gd^{3+}$ (10-50 mol%) UCNP was examined. The investigation of temperature influence on upconversion luminescence can provide more insight into the luminescence properties of UCNP. In Figure 20, emission spectra of UCNP (λ_{ex} = 976 nm) for the temperature range of 4 K < T < 290 K are presented. The observed pattern was representative for most of the studied UCNP.

As can be seen in Figure 20, the intensity of NIR emission band is much higher than B1 or B2 at any given temperature. The luminescence intensities of both emission bands are lower at room temperature and show a steady increase with cooling down from 290 K to 4 K. These results differ from the data presented in literature for similar studies on Er^{3+}-doped nanoparticles [10], [153]: for $NaYF_4:Yb^{3+},Er^{3+}$ UCNP doped with either different amounts of Gd^{3+} or Er^{3+}, all samples have shown a maximum luminescence intensity point at temperatures in the range of 50-100 K (depending on the doping concentration), followed by a decrease in luminescence intensity.

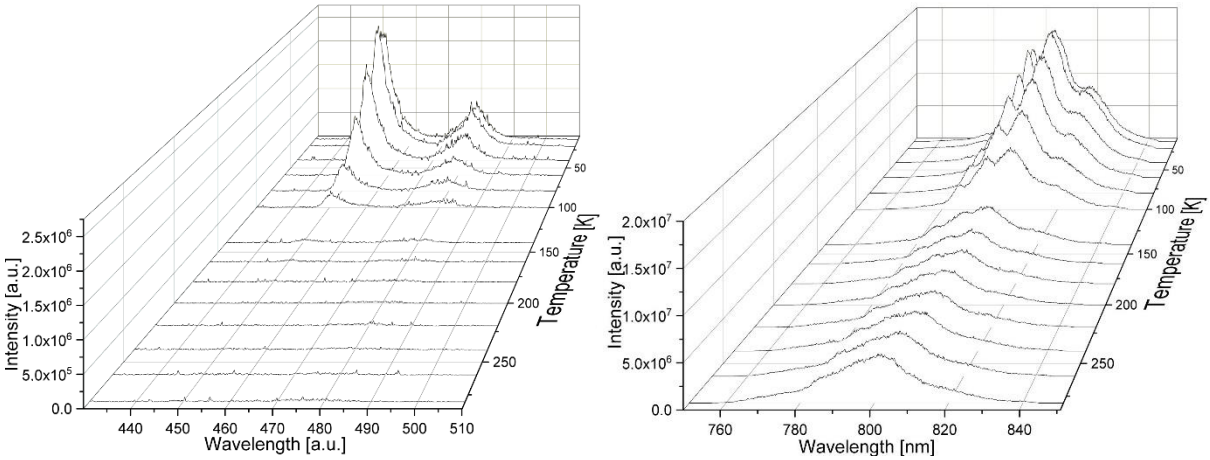

Figure 20. Temperature-dependent UC emission of as-synthesized $NaYF_4:Yb^{3+},Tm^{3+},Gd^{3+}$ (50 mol%) UCNP (λ_{ex} = 976 nm). Blue (B1) and (B2) (left) and near-infrared (NIR) (right) emission bands are shown. Continuous-wave fiber coupled laser operating at 1000mW was used to record the spectra. Initial gate delay Δt = 500 ns, gate width t_{gate} = 200 µs, step: 11 µs).

Normalized luminescence intensities of the blue (B1+B2) and NIR emission bands for $NaYF_4:Yb^{3+},Tm^{3+},Gd^{3+}$ (10-50 mol%) UCNP were plotted as a function of temperature (in the range of 4 to 290 K) (Supporting Information, Figure 57). In general, the intensity of both blue and near infra-red luminescence increased with the decrease of temperature in all examined samples. To further process these data, an Arrhenius-type equation was used [10], [154], [155]:

$$R = \frac{I_B}{I_{NIR}} = A \exp(-\frac{\Delta E}{k_B T}) \qquad (16)$$

where R is the ratio of integrated luminescence intensities originating from UCL emission bands, ΔE is the energy gap, k_B is the Boltzmann constant, T is the temperature, and A is a constant which depends on the spontaneous emission rate and the energies of the emitting states of the host material [10].

The logarithm of the intensity ratios of the UCNP luminescence bands (as an example, B and NIR as shown in Figure 21) was plotted against reciprocal temperature, and fitted to calculate the energy gap ΔE according to the Equation 16. The same has been done for the ratios B1/NIR, and B2/NIR. The resulting values of ΔE can be found in Table 6.

The resulting ΔE values were within the range of 30-40 cm^{-1} for all studied samples, and we didn't observe any clear influence of Gd^{3+} content on the energy gap values. These results can be explained by the following: in Yb^{3+} the two lowest energy field components of the $^2F_{5/2}$ multiplet are $^2F_{5/2}|0\rangle$ (~10281 cm^{-1}) and $^2F_{5/2}|1\rangle$ (~10242 cm^{-1}). Temperature-dependent emission is determined by both population and excitation cross-section of $^2F_{5/2}|0\rangle$ and $^2F_{5/2}|1\rangle$ levels of Yb^{3+}; both of those parameters depend on temperature [10], [156]. The energy difference between the two Stark levels is known from literature to be just 39 cm^{-1}.

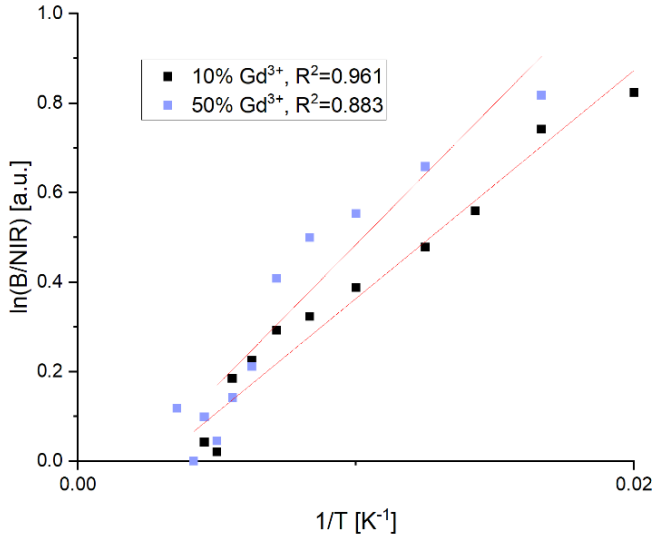

Figure 21. Analysis of temperature dependence of the logarithm of the integrated emission intensity ratio of B and NIR bands on the example of $NaYF_4:Yb^{3+},Tm^{3+},Gd^{3+}$ (10 and 50 mol%).

Table 6. Energy gap $\Delta E_{B/NIR}$ of $NaYF_4:Yb^{3+},Tm^{3+},Gd^{3+}$ (10 - 50 mol%) UCNP calculated according to Equation (16).

Gd^{3+}content, mol%	ΔE, cm^{-1}	±
10 %	42	9
20%	38	10
30%	34	10
40%	34	9
50%	37	15

The experimental values obtained from our calculations are an order of magnitude lower than the values of a ΔE reported for the emission of Er^{3+} [10], [156], [157], and lower than the expected values for Tm^{3+}, since the energy difference of the involved intermediate states is larger, but very close to the values of the energy gap of Yb^{3+} known from literature. A possible explanation for that is that, unlike in the Er^{3+}-Yb^{3+} pair, energy transfer from Yb^{3+} to Tm^{3+} is not strongly influenced by the energy field components of Yb^{3+}, as the $^3H_5$ energy level of Tm^{3+} is substantially lower than either $^2F_{5/2}|0\rangle$ or $^2F_{5/2}|1\rangle$ (unlike the $^4I_{11/2}$ level of Tm) [10]. Since the content of Yb^{3+} in all of the studied UCNP species was kept identical, it also explains why the content of Gd^{3+} had no effect on the ΔE values. Thus, we can conclude that, most likely, the energy gap values that we obtained from the experiment could rather be assigned to the excited state of Yb^{3+}rather than Tm^{3+}.

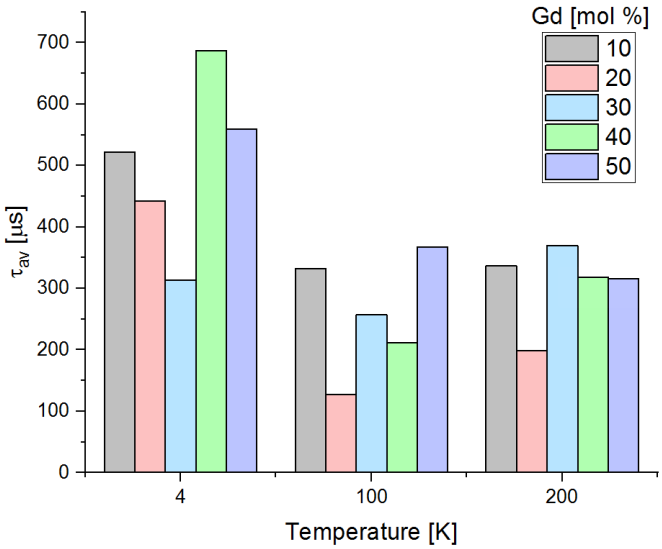

Figure 22. Luminescence decay kinetics were recorded for all as-synthesized UCNP species at 4, 100 and 200 K and analyzed using a biexponential decay law (Equation 8, Figure 18). The general trend showed a decrease of luminescence decay times with the increase of temperature.

4.2.5 Summary and conclusion

Five samples of $NaYF_4:Yb^{3+},Tm^{3+},Gd^{3+}$ (10-50 mol%) upconverting nanoparticles were synthesized using one-pot thermal decomposition method with oleic acid as a capping agent. Their photophysical properties were compared in order to get closer to the understanding of the influence of Gd^{3+} co-doping on the properties of UCNP. The UCNP showed strong upconversion luminescence upon 976 nm pulsed Nd:YAG laser excitation and luminescence lifetimes in the range from tens to hundreds of μs.

No clear trends were detected in terms of the Gd^{3+} concentration influence on the properties of UCNP. The size and shape regularity peaked at 30 mol% Gd^{3+}, which lead to higher luminescence emission intensities and longer luminescence lifetimes. No influence on the crystal state was detected via XRD. This differs from the data on Er^{3+}-doped UCNP found in literature [10], [153]: there, the increase of Gd^{3+} doping concentrations lead to the increase of β-phase in the crystal structure of UCNP up to pure hexagonal nanocrystals, which, in turn, improved their photophysical properties.

Comparison of the properties of the same UCNP series ($NaYF_4:Yb^{3+},Tm^{3+},Gd^{3+}$ (10-50 mol%)) right after the synthesis and after 24 months of storage in cyclohexane was conducted. While no drastic changes were noted in their upconversion behavior and trends in dependence on Gd^{3+} doping concentrations, there seemed to be more agglomeration of the nanoparticles and a slight decrease of the size of the "fine" fractions of UCNP. This led to longer decay times and a change in luminescence band ratios.

As a closure, it can be noted that the rather faint influence of Gd^{3+} content on the photophysical properties of $NaYF_4:Yb^{3+},Tm^{3+},Gd^{3+}$ UCNP is overpowered by other synthesis parameters such as control over temperature, reaction time and the choice of a fitting solvent. Syntheses of samples described above were performed using co-solvents and equipment that didn't allow

sufficient precision of reaction parameters such as temperature. This problem will be addressed in the following chapters.

4.3 *Improved synthesis route for sub-10 nm pure hexagonal $NaYF_4$:Yb^{3+},Tm^{3+}*

One of the recent advances in the synthesis of $NaYF_4$-based upconverting nanoparticles is the utilization of Therminol® 66 (later, just Therminol for shortness) as a reaction solvent along with oleic acid. Therminol is a high-boiling commercially available organic fluid that consists of a mixture of terphenyls, hydrogenated terphenyls, and hydrogenated polyphenyls (Figure 23), and is frequently used as a heat-transfer fluid in the industry [158] as well as for preparation of quantum dots [159], [160].

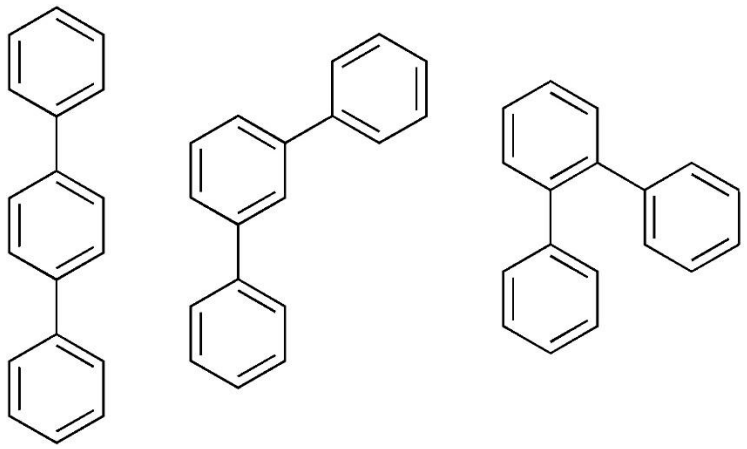

Figure 23. Molecular structures of main terphenyl isomers present in Therminol® 66.

Reaction temperature is a crucial parameter in the synthesis of UCNP: it influences the size, shape and crystal phase of the nanoparticles. In order to convert from the cubic (α-) phase to the thermodynamically stable hexagonal phase, the nanoparticles need to overcome an energy barrier, which requires temperatures above 300°C [161]. Thus, precise control over the reaction conditions is crucial for creating small, homogeneous, hexagonal nanoparticles. The use of Therminol as a co-solvent and the appliance of the LabHeat heating mantle coupled to a temperature controller allowed us to control the reaction conditions more precisely and thus, not only to reduce the reaction time to 15 minutes (instead of the 90 minutes for the same synthesis route with octadecene as a co-solvent) (Figure 9), but also to obtain highly homogeneous sub-10 nm UCNP. The procedure is explained in detail in the section 3.1.3.

As a further step to improve the photophysical properties of the UCNP, an inert, or passive, shell consisting of $NaYF_4$ without any dopants was added to the nanoparticles. This addition has been shown to make up for such shortcomings as surface quenching and low efficiency of the simple UCNP, and thus, greatly enhance their quantum yield and emission intensity [70], [162].

In order to create a "passive" $NaYF_4$ shell around the $NaYF_4$:Yb^{3+},Tm^{3+} UCNP, the earlier synthesized core UCNP were used after several rounds of washing. A solution of core UCNP in cyclohexane was transferred in 20 mL of the OA-Therminol mixture (3:2 volume ratio), heated to 75°C for 30 min under vacuum to remove the cyclohexane. After, under a constant flow of argon, the reaction temperature was elevated to 310 °C. The shell precursor solution composed of $NaYF_4$ in 3:2 Oleic Acid/Therminol was added dropwise using a peristaltic syringe pump at a rate of 2 mL/h^{-1}. The slow injection rate allowed for the decomposed shell

precursor to attach directly to the surface of nanocrystals, as the monomer concentration doesn't exceed the nucleation threshold. From here on, we will refer to the $NaYF_4:Yb^{3+},Tm^{3+}$ as core particles, and $NaYF_4:Yb^{3+},Tm^{3+}@NaYF_4$ – as core-shell UCNP.

4.3.1 Basic characterization of the resulting UCNP

The properties of the UCNP synthesized using the synthesis route involving Therminol described above resulted in high homogeneity of the sizes and shapes, and, thus, optical properties of the resulting UCNP not only within a single synthesis batch, but across different syntheses. Thus, we will describe a sample batch of as-synthesized UCNP and later use it as a reference unless a particular experiment requires a sample with different properties, in which case it will be adverted specifically.

The crystalline structure of the core-shell UCNP was studied using XRD. As can be seen from Figure 24, the particles resulted to be pure β-phase.

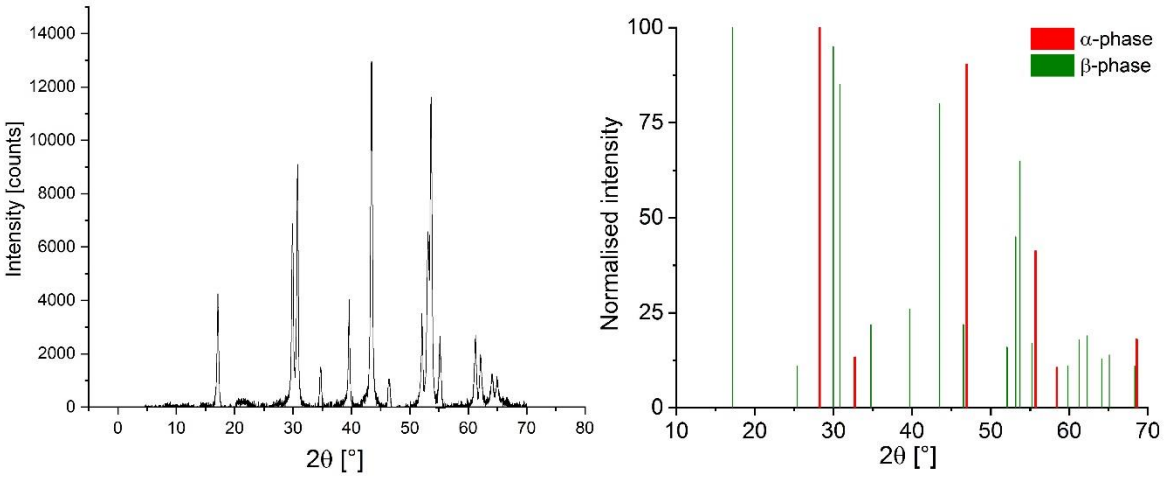

Figure 24. A sample X-ray powder diffractogram of $NaYF_4:Yb^{3+},Tm^{3+}@$ $NaYF_4$ UCNP synthesized with Therminol as a co-solvent (left). Reference XRD reflection data origin from JCPDs No. 01-077-2042 (-$NaYF_4$) and JCPDs No. 00-028-1192(-$NaYF_4$).

Transmission electron micrographs of core and core-shell UCNP with corresponding diameters are presented in Figure 25. It can be noted that the morphology of the particles after coating didn't change, which means that the shell formed evenly around the core UCNP. The addition of the passivating shell resulted in a 2.5 nm increase of UCNP diameter, thus, the thickness of the shell is just above 1 nm. The size distribution in both core- and core-shell UCNP is also quite narrow, with the error bar not exceeding 1.5 nm.

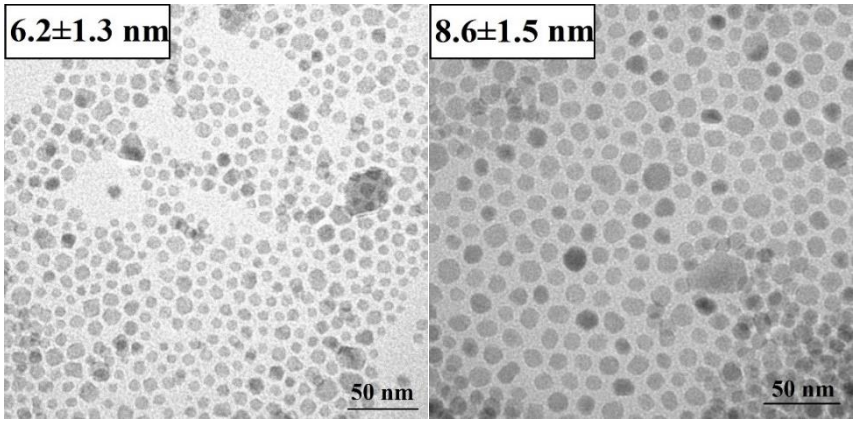

Figure 25. TEM micrographs of core ($NaYF_4$:Yb^{3+},Tm^{3+}) and core-shell ($NaYF_4$:Yb^{3+},Tm^{3+}@$NaYF_4$) UCNP. The scale bar is 50 nm.

4.3.2 Upconversion luminescence properties

The upconversion luminescence spectra of $NaYF_4$:Yb^{3+},Tm^{3+} and $NaYF_4$:Yb^{3+},Tm^{3+}@$NaYF_4$ upconverting nanoparticles capped with oleic acid and dissolved in cyclohexane was recorded upon excitation at 976 nm for three luminescence bands: 451 ($^1D_2 \rightarrow {}^3F_4$ transition, B1), 481 ($^1G_4 \rightarrow {}^3H_6$ transition, B2), and 800 ($^3H_4 \rightarrow {}^3H_6$ transition, NIR) nm.

As mentioned in chapter 4.2.2, it is difficult to compare luminescence intensities between samples, as such parameters as excitation laser power and concentration of the sample influence the result of each measurement, and it is not always possible to correct for all of these parameters. Here, we normalized luminescence spectra of core- and core-shell UCNP to concentration ($mg \cdot mL^{-1}$) and performed the measurements on the same day with the same excitation compared to each other. The results can be seen in Figure 26: the intensity of both blue and the NIR emission bands are significantly higher in core-shell nanoparticles. Interestingly, different emission bands show different increase in intensity: the lowest difference was observed in the band at 481 nm ($^1G_4 \rightarrow {}^3H_6$ transition), which corresponds to a 3-photon process. The 4-photon transition at 451 nm ($^1D_2 \rightarrow {}^3F_4$) and the 2-photon $^3H_4 \rightarrow {}^3H_6$ transition at 800 nm were more affected by the addition of the shell (Figure 27).

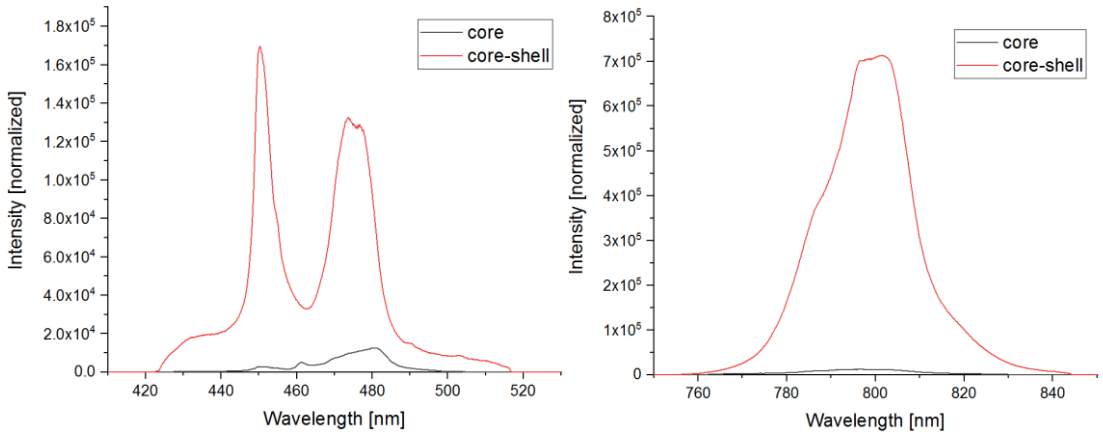

Figure 26. Upconversion emission intensities of $NaYF_4$:Yb^{3+},Tm^{3+} core and core-shell UCNP upon pulsed excitation at 976 nm (laser power 63.7 mW). Sample concentrations and measurement conditions were kept similar for both samples. Blue (B1) and (B2) (left) and near-infrared (NIR) (right) emission bands are shown.

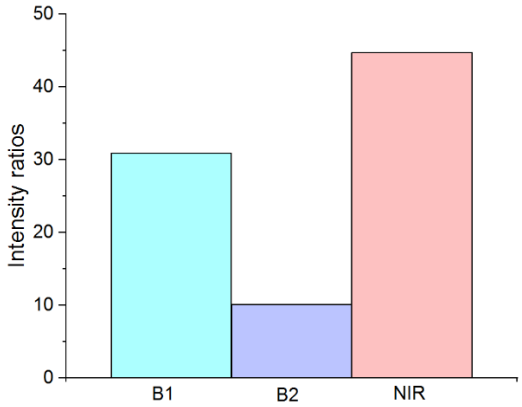

Figure 27. Core-shell to core UCNP luminescence band intensity ratios for B1 (451nm) B2 (481 nm) and NIR (800 nm) emission bands.

Similar to the previous chapter, the intensity ratios between the luminescence bands (B1/NIR and B2/NIR) were compared in core-and core-shell UCNP (Figure 28). The most drastic difference after the addition of the shell was observed in the B2/NIR ratio, which is explained by the simultaneous intensity rise in the 451 nm ($^1D_2 \rightarrow {}^3F_4$) and 800 nm ($^3H_4 \rightarrow {}^3H_6$) bands after the addition of the passivating shell, which was higher in comparison to the rise of the 481 nm ($^1G_4 \rightarrow {}^3H_6$) band.

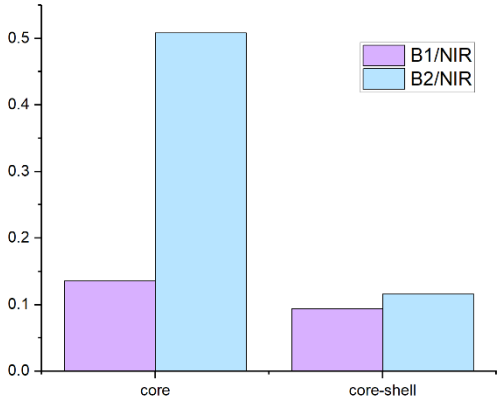

Figure 28. Intensity ratios of B1/NIR (purple) and B2/NIR (blue) luminescence bands of core- and core-shell $NaYF_4:Yb^{3+},Tm^{3+}$ UCNP upon excitation at 976 nm.

As the next step of the basic characterization of the UCNP synthesized via the improved method, the luminescence decay kinetics of both core and core-shell $NaYF_4$-based nanoparticles were studied.

Using a biexponential decay law (Equation 8), the decay curves (example in Figure 29) were fitted to obtain the luminescence decay times of UCNP as described in the previous chapter (4.2.3).

It can be seen from Table 7 that the luminescence decay times of the resulting UCNP are higher than those of the UCNP synthesized via the older synthesis route and co-doped with Gd^{3+} (Table 4).They averaged at about 1-2 hundreds of µs. Also, the addition of the shell increased the luminescence lifetimes by ~50%. The B1 luminescence band associated with a 4-photon

transition ($^1D_2 \rightarrow {}^3F_4$) showed the lowest decay time values, while the decay times of the three-photon (481 nm) and 2-photon (800 nm) bands were very similar.

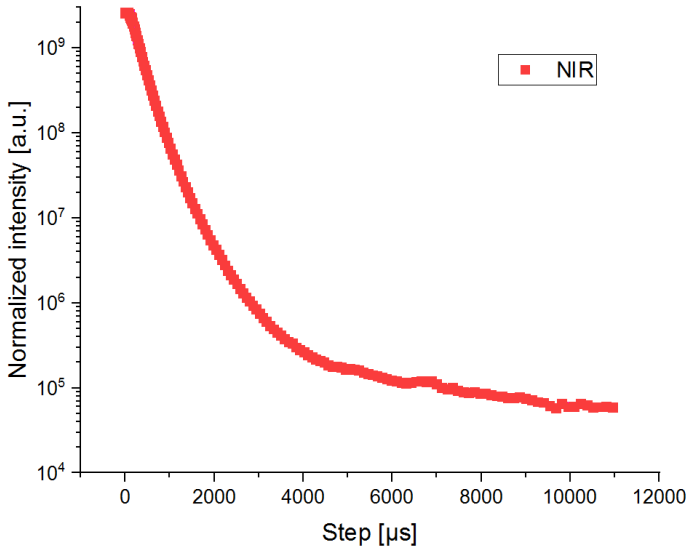

Figure 29. Normalized UC luminescence decay kinetics of the Tm^{3+} NIR emission band (800 nm) of core-shell $NaYF_4:Yb^{3+},Tm^{3+}@NaYF_4$ UCNP excited at 976 nm, initial delay Δt = 500 ns.

Table 7. Luminescence decay times with respective fractions (in parentheses) calculated as shown in Equation 9 of Yb^{3+}, Tm^{3+}-doped $NaYF_4$ UCNP upon 976 nm excitation (as calculated from PL decay curves, e.g., in Figure 29). τ_1 is the short component of the luminescence decay time, τ_2 is the long component and τ_{av} is the average time of luminescence decay.

Emission band with respective transition	τ, µs	$NaYF_4:Yb^{3+},Tm^{3+}$ (core)	$NaYF_4:Yb^{3+},Tm^{3+}@NaYF_4$ (core-shell)
451 nm $^1D_2 \rightarrow {}^3F_4$	τ_1	67 (82%)	106 (75%)
	τ_2	273 (18%)	319 (25%)
	τ_{av}	**104**	**159**
481 nm $^1G_4 \rightarrow {}^3H_6$	τ_1	117 (76%)	176 (72%)
	τ_2	350 (24%)	419 (28%)
	τ_{av}	**173**	**245**
800 nm $^3H_4 \rightarrow {}^3H_6$	τ_1	62 (63%)	205 (86%)
	τ_2	332 (37%)	471 (14%)
	τ_{av}	**162**	**241**

Thus, the set of performed studies of the UCNP resulting from the new synthesis approach with Therminol as a co-solvent has shown that the physicochemical and photophysical properties have significantly improved compared to the Gd^{3+}-doped UCNP synthesized using the previous procedure. The new UCNP have shown high homogeneity, pure hexagonal structure, higher intensity of Tm^{3+} luminescence, and hence, higher efficiency of the upconversion process, and longer luminescence lifetimes. Addition of a passivating $NaYF_4$ shell has proven to increase the upconversion intensity and luminescence lifetimes due to the protection of emitting ions from surface quenching processes, while preserving the hexagonal structure and size and shape regularity of the UCNP. We were able to achieve a shell thickness of less than 2 nm, keeping the size of the resulting core-shell UCNP under 10 nm.

From the results described above, it can be assumed that in the process of UCNP synthesis control over temperature is one of the most crucial parameters to consider. With establishing a protocol where a precise and constant control of the reaction conditions was possible, we were able to achieve the production of the UCNP with the desired properties, which was more difficult with the procedure discussed in the previous chapter even with Gd^{3+} co-doping.

As the final step of the characterization of core and core-shell UCNP, the variations in integrated intensities of the B1, B2 and NIR emission bands were analyzed as a function of applied excitation power density (P). The upconversion quantum yield depends on the power density of the excitation beam, because UC is a non-linear multiphoton process. At lower excitation power, the emission intensity (I) is proportional to P^n, where the slope value (n) should indicate the number of photons involved in the process of UC (on a log-log plot, n is the slope of the linear least-squares curve through the data points). With the increase of excitation power, however, the intermediate excited states become saturated, and n tends to reduce to 1 [163].

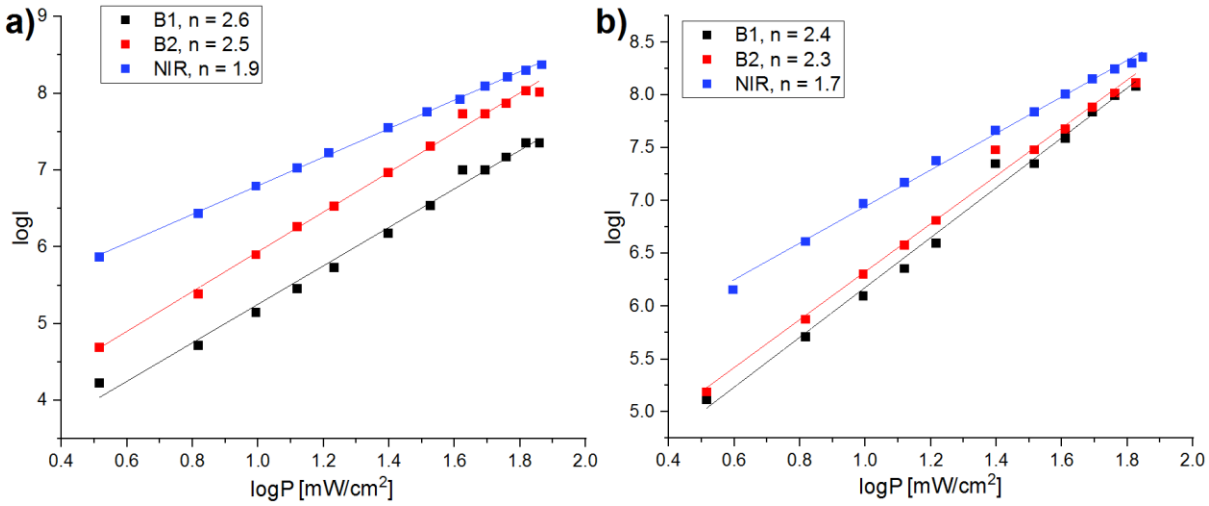

Figure 30. Power dependence (Log Intensity – Log Power Density (P) plot) of B1, B2 and NIR Tm^{3+} transitions of core (a) and core-shell (b) UCNP upon pulsed excitation at 976 nm.

The results of these studies have shown that at λ_{ex} = 976 nm, in core UCNP, for B1 and B2 transitions ($^1D_2 \rightarrow {}^3F_4$ and $^1G_4 \rightarrow {}^3H_6$, respectively) the slope numbers could suggest three-

photon processes (although for B2, a 2-photon process could be attributed as well), while the slope number of the NIR transition ($^3H_4 \rightarrow {}^3H_6$) was hinting at a 2-photon process. After the addition of a passivating shell, neither of the numbers of photons attributed to each transition showed significant changes (Figure 30). There was no evidence of saturation of the excited states in any of the samples, which is in accordance with other studies at similar excitation powers [163].

4.4 Studying the energy transfer between Tm^{3+}-doped upconverting nanoparticles (UCNP) and an organic (DBD-6) dye[1]

Förster resonance energy transfer (FRET), according to Theodor Förster (1946), is a non-radiative phenomenon based on Coulombic interaction, where the energy is transferred from an excited donor (D) fluorophore to an acceptor (A) fluorophore by means of intermolecular dipole–dipole coupling [15]. The efficiency of FRET process depends on the D-A distance with an inverse 6th-power law. This distance sensitivity makes FRET a very suitable technology for the detection of near-field interaction between molecules [164].

Thus, it is frequently used to determine the distance between molecules on a nanometer scale: to monitor conformational changes in biomolecules or to quantitatively determine a binding interaction between two molecules, for instance, antigen-antibody interactions [16], [17]. These applications are possible because both are connected to a change in relevant distance. This distance alteration can be monitored with high sensitivity (even on a single molecule level) in real time, which makes its application even more valuable [18].

To create a FRET-based sensing scheme, it is mandatory to introduce a pair of suitable chromophores with matched photophysical properties. In order for the energy transfer process to be effective, the spectral match (expressed as the spectral overlap integral between D emission and A absorption) (Equation 5), the orientation of the transition dipole moments between D and A (orientation factor κ^2) (Equation 4), and the emission quantum yield of the D must be large [78].

Organic chromophores, often chosen as participants of the FRET process, are characterized by a set of drawbacks, such as: photobleaching, short fluorescence lifetimes (just several nanoseconds), and chemical instability. In a search for a fluorophore that would overcome the aforementioned challenges, luminescent nanoparticles have emerged as powerful competitors for organic dyes [15]. For instance, semiconductor quantum dots (Qdots) show superior photostability, high brightness, and sharp emission lines, but also suffer from photoblinking, which nevertheless allows them to be successfully integrated in FRET-based sensing schemes serving as D or A.

UCNP present a specific interest as participants in the process of FRET. Not only are UCNP non-toxic, non-blinking, and chemically inert, but they also present a system with an inner energy transfer process of its own. This can present a challenge by lowering the overall efficiency of the process, but is easily overpowered by their advantages, such as low background fluorescence, large anti-Stokes shifts, long (up to hundreds of μs) luminescence lifetimes and outstanding photostability. Thus, UCNP are promising and particularly interesting donor emitters in FRET systems [55], [165].

For this reason, the interest in FRET applications involving UCNP is steadily growing, but there're still a lot of questions to be answered. In most studies the energy transfer process is

[1] This chapter contains excerpts and images from the publication: López de Guereñu A., Bastian P., Wessig P., John L., Kumke M. U. **Energy Transfer Between Tm-doped Upconverting nanoparticles (UCNP) and a Small Organic Dye with Large Stokes Shift.** Biosensors 2019, 9, 9; doi:10.3390/bios9010009.

partially based on FRET, but it also often contains contributions from reabsorption [166], [167]. Some studies with in-depth investigation of UCNP in FRET applications have been recently published, and the influence of various factors such as size [168], structure [169] and dye/UCNP ratio [170] were discussed. The optimal UCNP size for the highest (up to 60%) FRET efficiency established by [168] to be 21 nm, while with different (higher and lower) surface-to volume ratios the competition with non-radiative surface deactivation impaired the efficiency. They used sulfo-rhodamine B and Rose Bengal as dye models. The study of [170] has dived into the complexity of the dye-UCNP FRET systems, and established the optimal Rhodamine B dye concentration of 6.6 % eq. per monomer used for UCNP coating. Finally, the [169] study underlined the importance of time-resolved measurements for FRET investigation, and established active core and inert core-active shell UCNPs to have the highest FRET efficiency among the studied samples.

Here, we studied the FRET process between four types of $NaYF_4:Yb^{3+},Tm^{3+}$ UCNP (used as donors in the process of FRET) and a DBD-based dye (as a FRET acceptor). The activator (Tm^{3+}) was either doped in the core or the shell of the nanoparticles and the dye was attached to the surface of UCNP via a ligand exchange process.

4.4.1 Synthesis and characterization of DBD-labelled fatty acid (DBD-6)

[1,3]dioxolo [4,5-f]- [1,3]benzodioxole (DBD)-based fluorophores have been first reported by the group of P. Wessig of the Organic Chemistry department of the University of Potsdam in the year 2011. DBD-based dyes are a new class of fluorescent dyes characterized by large Stokes-shifts, long fluorescence lifetimes in organic solvents (which strongly depend on solvent polarity), and high bleaching stability [171]–[173].

The dye used in this study (DBD-6) was synthesized and kindly provided to us by L. John from the group of prof. P. Wessig of the Organic Chemistry Department of University of Potsdam. Photophysical properties of DBD-6 are summarized in

Table 8.

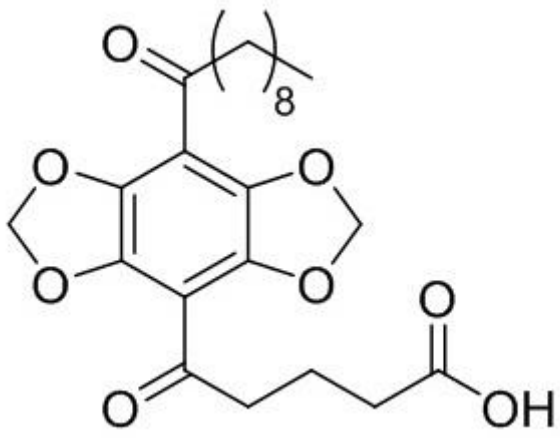

Figure 31. 5-(8-decanoylbenzo[1,2-d:4,5-d′]bis-([1.3]dioxole)-4-yl)-5-oxopentanoic acid (DBD- 6)

Table 8. Photophysical properties of the DBD-6 dye

Solvent	λ_{Abs} [nm]	λ_{Em} [nm]	$\Delta\lambda$ [nm]	τ_F [ns]	ε[$M^{-1}cm^{-1}$]	φF
DCM	435	547	112	26.1	2970	0.66
ACN	422	560	138	21.9	2890	0.51
methanol	436	605	169	4.6	2550	0.08
H_2O	463	557	94	8.1[a]	2530	0.09

[a] $<\tau_F>$, 4.9 ns (35.0 %), 9.0 ns (65.0 %)

4.4.2 Design and Synthesis of Dye-Labeled UCNP

Four types of UCNP were used to study the process and nature of the energy transfer between the UCNP and the DBD-6 dye. The first type of UCNP consisted of active core (AC) $NaYF_4:Yb^{3+},Tm^{3+}$ nanoparticles and contained traces of the internal reference Er^{3+}. The ions of Er^{3+} were not affected by the energy transfer process, and hence provided a reference luminescence band at 550 nm. This applies for all other UCNP samples; thus, it will not be stated explicitly from now on. The AC nanoparticles are known to provide comparatively low upconversion luminescence intensity due to surface quenching, so a protective shell is often used to improve their emission intensity [70].

For the second sample, we used an inert (undoped) $NaYF_4$ shell with a thickness of about 1.2 nm. The shell was added to estimate the influence of surface quenching and the increase of the donor–acceptor distance on the energy transfer (ET) process. The tight control of the experimental conditions discussed in the previous chapter allowed us to synthesize tailored shells with a thickness of only 1–2 nm (see Table 9 and Figure 32 for particle size information). We will refer to these UCNP as active core and inert shell (AC-IS).

In previously described active core and AC-IS particles Tm^{3+} ions are present both on the surface and in the bulk of a nanoparticle, thus, individual donor–acceptor distances depend on the respective location of Tm^{3+} relative to the surface, and a distribution of distance has to be taken into account. To limit the distance between the FRET D-A pairs, we designed two additional kinds of UCNP with no Tm^{3+} ions in the core. These samples consisted of a $NaYF_4:Yb^{3+}$ core and contained Tm^{3+} or both Tm^{3+} and Yb^{3+} ions in a sub-2 nm shell (Table 9, Figure 32). These particles will be referred to as inert core - Tm^{3+} shell (IC-TS) and inert core - Tm^{3+} and Yb^{3+} shell (IC-TYS). The addition of Yb^{3+} in the shell of one of the species was aimed at evaluating the influence of the distance between activator (Tm^{3+}) and sensitizer (Yb^{3+}) ions on the efficiency of upconversion and the subsequent energy transfer process. In the case of the IC-TS UCNP, the surface quenching of the sensitizer Yb^{3+} was also eliminated.

Table 9. Diameters of UCNP in cyclohexane (determined by TEM)

Sample	AC	AC-IS	IC-TS	IC-TYS	IC-TYS@dye
Diameter, nm	6.3±1.4	8.8±1.7	7.7±1.6	9.8±1.5	9.8±1.5

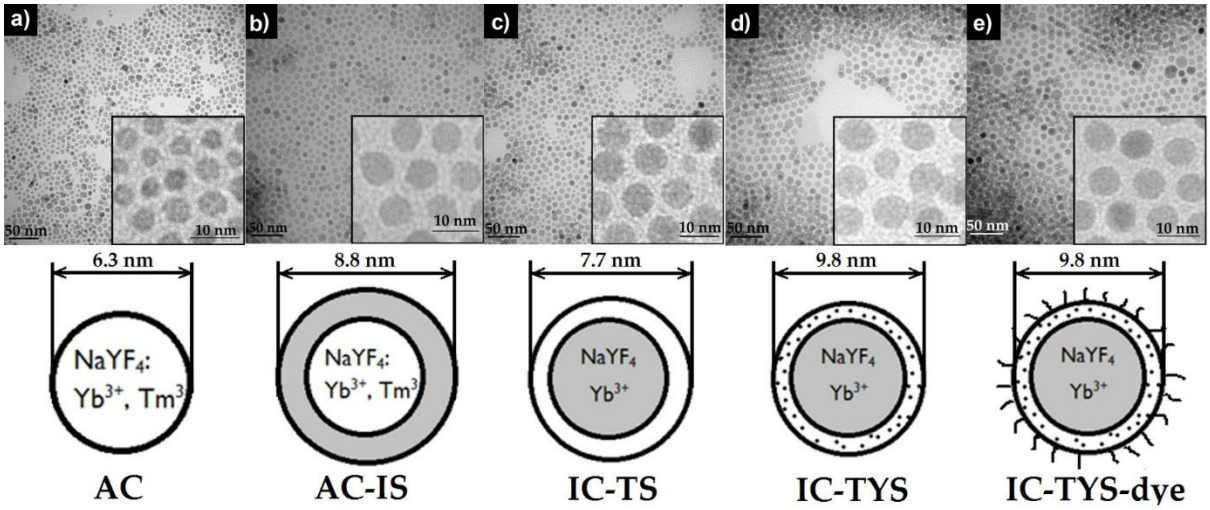

Figure 32. TEM images of $NaYF_4$:Yb^{3+},Tm^{3+} UCNP: (a) active core (AC), (b) active core and inert shell (AC-IS), (c) inert core and Tm^{3+} shell (IC-TS), (d) inert core and Yb^{3+}, Tm^{3+} shell (IC-TYS), (e) inert core and Yb^{3+}, Tm^{3+} shell with dye (IC-TYS@dye). The scale bar is 50 nm (or 10 nm for the inset). Acceleration voltage 200 kV.

The as-synthesized UCNP are usually capped with oleic acid (OA) and soluble in cyclohexane. The DBD-6 dye roughly shares the same solubility characteristics as oleic acid: it has a hydrophilic carboxylic group and a hydrophobic hydrocarbon chain (Figure 31). Therefore, we incubated the OA-capped UCNP with the dye solution under vigorous stirring for 24 hours which led to the replacement of OA molecules by DBD-6 molecules via ligand exchange (vide infra).

As can be seen from TEM micrographs shown in Figure 32, all four samples of UCNP were uniform in size and possessed a hexagonal lattice, which was also proven by XRD and the spectral intensity distribution of the Er^{3+} luminescence in the green spectral region (vide infra) [9]. The addition of the dye to the surface of UCNP did neither change the morphology nor resulted in clustering of UCNP.

To estimate the number of DBD-6 molecules per one UCNP, the dye absorption values of the supernatant solution were measured in samples with a fixed concentration of DBD-6 and decreasing concentrations of the UCNP. The approximate calculation of the number of dye molecules per UCNP revealed the following trend: with the increase of the UCNP concentration, the dye/UCNP number decreased almost tenfold (from 837±93 to 92±22). Based on these numbers, measurements of the dye absorption are an easily accessible parameter to control UCNP concentration in a sample.

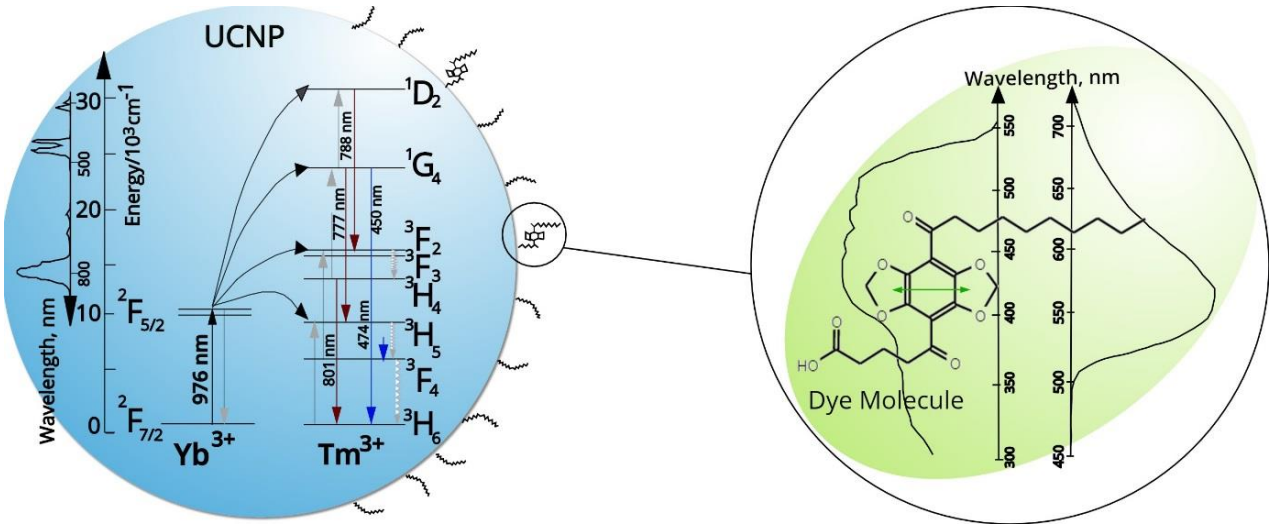

Figure 33. Schematic representation of the ligand exchange and energy transfer process between the DBD-6 dye and oleic acid-capped UCNP (left circle). Dye absorption (left) and emission (right) spectra and (right circle) UCNP emission overview are shown in black on the right side of the image. Transition moments of the DBD are shown as green arrows. Tm^{3+} emission spectra and energy level diagrams are shown on the left. The thickness of OA layer is ~1 nm and the distance between the UCNP surface and the DBD dye is ~0.5±0.2 nm.

We used Equation (17) to calculate the minimum and maximum Förster distance values R_{0min} and R_{0max} for the FRET pair UCNP-DBD-6, taking the overall upconversion luminescence quantum yield as F (estimated as F_{min} = 0.001 and F_{max} =0.01 according to reported literature values), resulting in R_{0min} = 0.11 nm and R_{0max} = 0.16 nm. This corresponds well with the values reported in literature for other UCNP FRET pairs [118], [174], [175].

$$R_0 = 0.02108(\kappa^2 \Phi n^{-4} J)^{1/6} \text{ nm} \quad (17)$$

Here κ^2 = 0.67 is the dipole orientation factor, Φ is the quantum yield of the donor, n = 1.42 is the refractive index of cyclohexane, and J (M^{-1} $cm^{-1}nm^4$) represents the spectral overlap between the area-normalized donor (Tm^{3+}) photoluminescence and acceptor (DBD-6) absorption spectra.

As an example, a calculation of the spectral overlap (J) for AC-IS nanoparticles decorated with DBD is presented in Figure 34, the resulting value $J = 1.91*10^8$ (M^{-1} $cm^{-1}nm^4$).

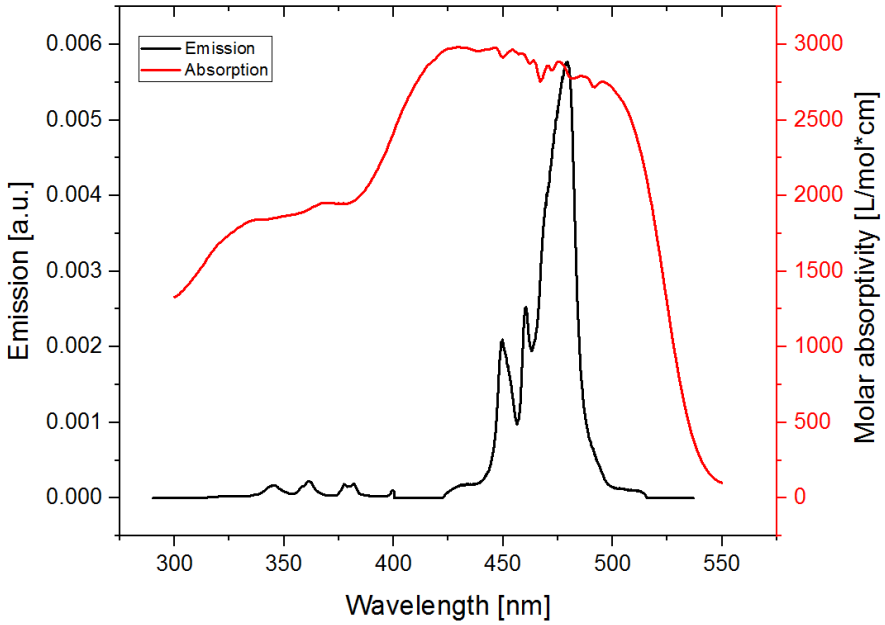

Figure 34. (Right axis) Molar absorptivity, $\varepsilon_A(\lambda)$ of DBD-6. (Left axis) Area-normalized upconversion luminescence intensity spectrum, $F_D(\lambda)$, of the AC-IS nanoparticles. Used to calculate the spectral overlap integral *J*. Both represented as a function of the excitation wavelength λ.

4.4.3 Luminescence emission spectra of Dye-Labeled UCNP

When $NaYF_4:Yb^{3+},Tm^{3+}$ UCNP are excited at 976 nm, $^2F_{7/2}\rightarrow{}^2F_{5/2}$ transition of trivalent ytterbium leads to emission of Tm^{3+} at 451 nm (assigned to $^1D_2\rightarrow{}^3F_4$ transition), at 481 nm ($^1G_4\rightarrow{}^3H_6$), and at 800 nm ($^3H_4\rightarrow{}^3H_6$) [176][12]. The absorption maximum of DBD-6 is in the range of 430–470 nm, which overlaps with Tm^{3+} blue emission peaks at 451 and 481 nm (see Figure 33 and Figure 34), respectively. Furthermore, the emission peak of the DBD-6 dye is quite broad and its maximum can be found around 550 nm (Figure 33).

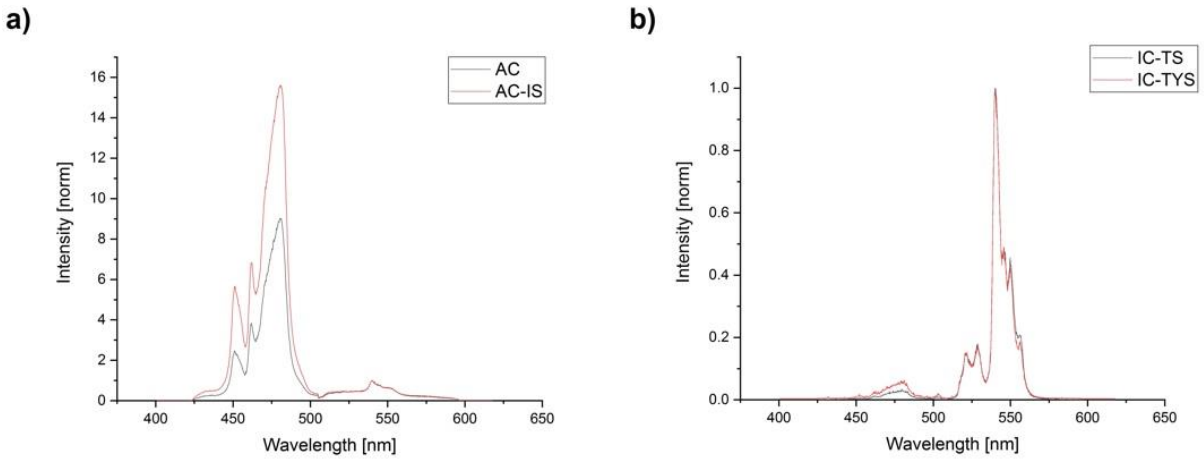

Figure 35. Upconversion photoluminescence spectra (intensity-normalized at 550 nm) of AC and AC-IS (a), IC-TS and IC-TYS (b) upon 976 nm pulsed excitation (laser power 62.1 mW).

Upconversion luminescence spectra of all UCNP species excited at 976 nm were normalized to the erbium reference luminescence band around 550 nm (Figure 35). The strongest blue luminescence (transitions $^1D_2\rightarrow{}^3F_4$ and $^1G_4\rightarrow{}^3H_6$) was observed in AC-IS, which corresponds

to data reported in literature: a passivating shell protects Tm^{3+} ions from being quenched by the solvent [70]. It was followed by AC, where Tm^{3+} ions were equally distributed inside and at the surface of UCNP: ions at the surface were more easily quenched than those in the bulk. IC-TS and IC-TYS have shown almost equally weak blue luminescence, although the luminescence intensity of the species with Yb^{3+} present also in the shell slightly surpassed the intensity of IC-TS. This indicates two points: first, in samples with Tm^{3+} ions only in the outer layer, surface quenching is especially strong for bands with 3- and 4-photon transitions ($^1D_2 \rightarrow {}^3F_4$ and $^1G_4 \rightarrow {}^3H_6$), thus, the intensity of the reference Er^{3+} luminescence band at 550 nm is much stronger. Second, the distance between sensitizer and activator ions plays a role in the upconversion process: the particles with Yb^{3+} ions not only in the core, but also in the shell (IC-TYS) have shown a slight increase in the blue band luminescence intensity compared to IC-TS. The elimination of the surface-related Yb^{3+} quenching does not compensate the decrease in the ETU due to larger distances between activator and sensitizer, especially in case of three- or four-photon-induced processes.

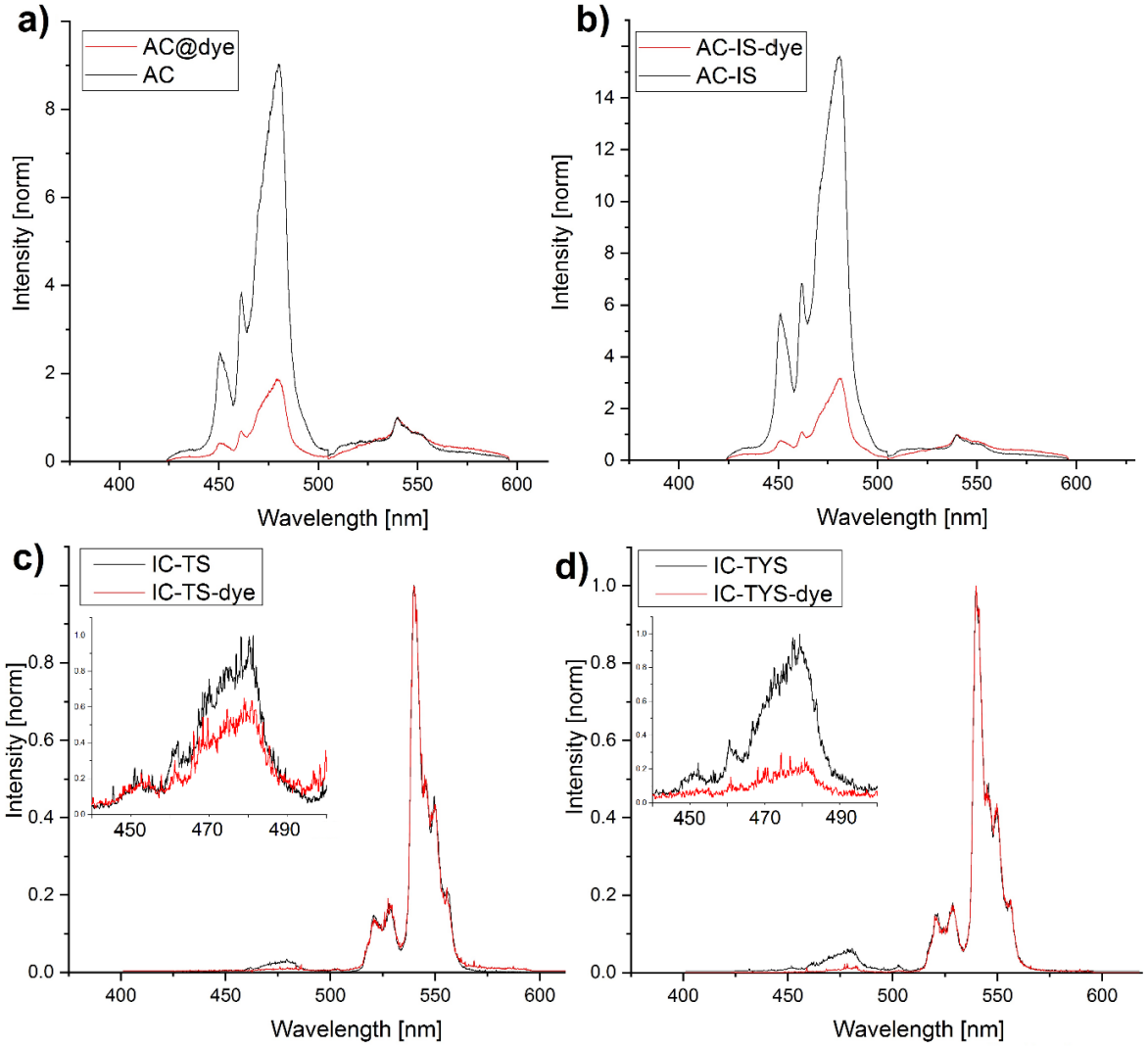

Figure 36. Upconversion photoluminescence spectra (intensity-normalized at 550 nm) of AC (a), AC-IS (b), IC-TS (c) and IC-TYS (d) upon pulsed 976 nm excitation (laser power 57.4 mW). For AC-IS species, the number of DBD-6 molecules per UCNP amounted to 92 ± 22, for IC-TS and IC-TYS-138 ± 39.

A prominent intensity drop of blue emission band was noticed for all UCNP samples labelled with DBD-6 (Figure 36). The selected dye concentrations were motivated, on one hand, by the theoretical prevalence of FRET mechanism over reabsorption, and on the other, by the solubility of the dye in cyclohexane. The blue/reference band ratios dropped up to 83 % (in AC-IS sample, Table 10).

Such significant drops in blue band emission can be attributed to Förster resonance energy transfer (FRET), since inner filter effects would only account for a much smaller drop (no more than 5%) [170]. Besides the highest decrease in the blue band intensity after addition of the dye, AC-IS species also showed the strongest luminescence at 470 nm. It was closely followed by the AC species, which didn't have a protective shell. Both "inert core" species have shown the smallest drops in blue/reference band ratios, although the blue luminescence was extremely weak to begin with. The number of dye molecules per UCNP was also larger in these samples (see Figure 36). Due to the close proximity of all Tm^{3+} ions to the surface in these samples, they were most prone to surface quenching which also might have competed with energy transfer to the dye.

As can be seen from the spectra (Figure 36: a, b), the peak assigned to $^1D_2 \rightarrow {}^3F_4$ transition, which has a better spectral overlap with DBD-6, was more affected by introduction of the dye. Furthermore, in samples labelled with DBD-6 dye a wide peak (around the reference peak) appeared, which was attributed to the dye emission. In reference experiments with samples containing only DBD-6, no dye emission was found for 976 nm excitation.

Table 10. Blue/reference band intensity ratios for all UCNP species with and without DBD-6

UCNP species	**no dye**	**with dye**
AC	5.8	1.1
AC-IS	10.1	1.7
IC-TS	0.15	0.11
IC-TYS	0.13	0.04

In Figure 37, the evolution of the reference band with time is presented. The wide band around 550 nm, which was attributed to the emission of the dye, was better visible in the AC and AC-IS samples, since the relative intensity of the reference band was lower. The luminescence lifetime of the dye hardly reaches 20 ns (when directly excited and measured with time-correlated single photon counting), while the luminescence of UCNP lasts for hundreds of µs. Thus, in the absence of FRET, by increasing the initial delay by tens or hundreds of µs, the dye signal must have already vanished, leaving only the signal from reference Er^{3+} emission. The spectra taken at 1, 25 and 50th steps of the luminescence decay kinetic measurement, corresponding to a delay of 100 ns, 84 µs and 357 µs, respectively, have shown no vanishing

of the broad band, which corresponded to the luminescence of the dye. This serves as direct evidence for the active FRET.

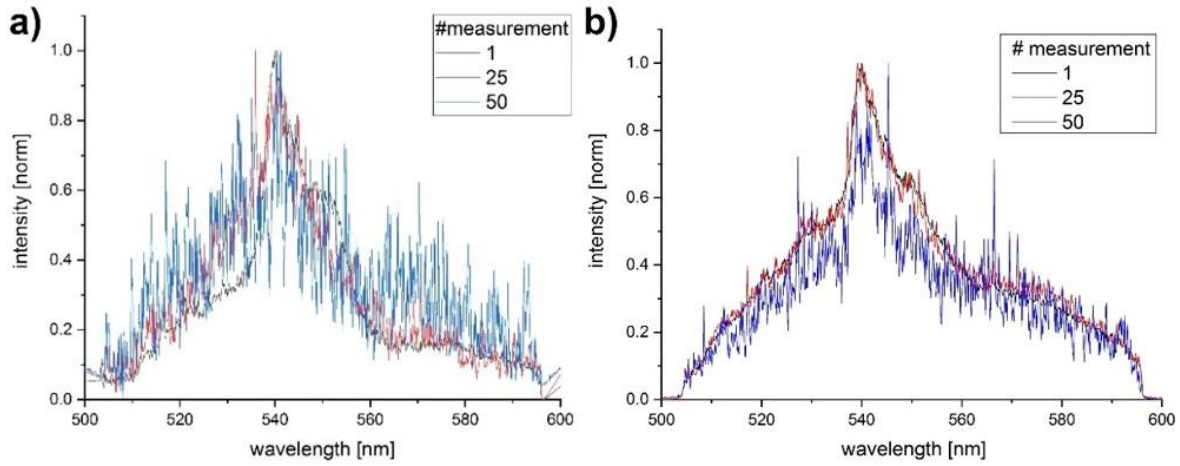

Figure 37. Reference/dye emission peak evolution with time of (a) AC, (b) AC-dye UCNP upon pulsed 976 nm excitation (laser power 59.5 mW).

4.4.4 Luminescence decay kinetics of the dye-labelled UCNP

Luminescence decay kinetics of different UCNP samples were measured for the blue (451 nm and 481 nm) and the reference (550 nm) emission bands upon 976 nm excitation (examples of luminescence decay kinetics are shown in Figure 38). The values of luminescence lifetimes were determined by fitting the decays using a biexponential model (Equation 8).

The short decay component (τ_1) is usually assigned to Tm^{3+} atoms located closer to the surface of the nanoparticles and thus more susceptible to surface quenching by the solvent. The longer decay component (τ_2) is attributed to the Tm^{3+} atoms located deeper in the "bulk". Both values are consistent with those found in literature (tens to hundreds of µs) [177].

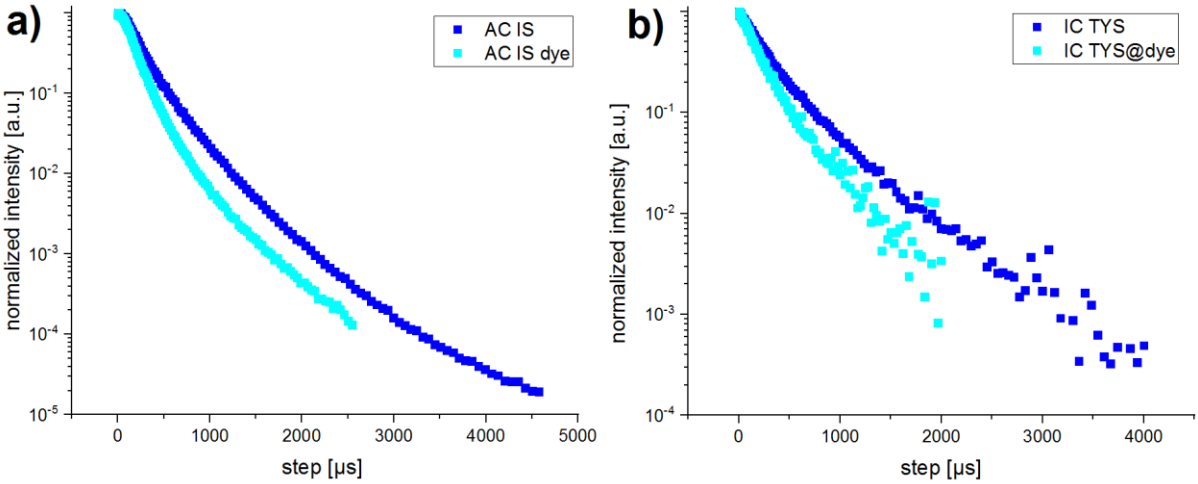

Figure 38. Upconversion luminescence decay of the blue emission bands ($^1D_2 \rightarrow {}^3F_4$ and $^1G_4 \rightarrow {}^3H_6$ transition) of quenched (cyan) and non-quenched (blue) AC (a) and IC TYS (b) UCNP upon pulsed 976 nm excitation.

From Table 11 it can be seen that the short components of photoluminescence decay kinetics of the blue emission band were shorter in dye-labelled samples compared to the samples without DBD-6. As for the reference band, no significant effect was observed (AC and IC-TS were not affected by the presence of DBD-6 dye, while AC-IS and IC-TYS have shown a slight decrease, that can, in fact, be neglected given the margin of error). Since the long components are normally attributed to the luminescence of the Tm^{3+} ions located in the bulk of UCNP, which means that the distance to the DBD-6 (FRET acceptor) is larger, we consider their contribution to FRET rather small and thus, we used only the short luminescence fraction (attributed to the emitting ions on the surface) for further calculations.

Table 11. Luminescence decay times with respective fractions (in parentheses) of AC, AC-IS, IC-TS and IC-TYS UCNP (blue: $^1D_2 \rightarrow {}^3F_4$ and $^1G_4 \rightarrow {}^3H_6$ transition) upon 976 nm excitation (as calculated from PL decay curves, e.g., in Figure 38).

t, µs/ fraction, %		**AC**	**AC @dye**	**AC-IS**	**AC-IS @dye**	**IC-TS**	**IC-TS @dye**	**IC-TYS**	**IC-TYS @dye**
blue (470 nm)	t_1	119 (77%)	84 (77%)	173 (78%)	144 (92%)	228 (65%)	176 (69%)	161 (45%)	79 (65%)
	t_2	308 (23%)	263 (23%)	387 (22%)	483 (8%)	567 (35%)	590 (31%)	582 (55%)	259 (35%)
	$\mathbf{t_{av}}$	**163±26**	**125±9**	**221±30**	**171±33**	**348±71**	**305±93**	**391±44**	**141±30**
reference (550 nm)	t_1	68 (82%)	69 (82%)	132 (84%)	116 (93%)	64 (86%)	61 (78%)	92 (58%)	57 (48%)
	t_2	233 (18%)	225 (18%)	328 (16%)	369 (7%)	214 (14%)	169 (22%)	479 (42%)	338 (52%)
	$\mathbf{t_{av}}$	**98±8**	**97±8**	**164±23**	**135±24**	**85±4**	**85±5**	**254±12**	**204±8**

The FRET efficiency of the UCNP-dye system was calculated using the data from non-labelled UCNP as a reference, *via* the classic equation for single donor-single acceptor pairs [169], [170]:

$$\eta = 1 - \frac{\tau_{with\ dye}}{\tau_{no\ dye}} \tag{18}$$

We used the short components of the blue band to calculate the FRET efficiency. The highest efficiency values were obtained for the sample IC-TYS, which had an inert core and both Tm^{3+} and Yb^{3+} ions in the shell, despite the low overall brightness of such UCNP. This was somewhat expected, since all donor ions of this UCNP species were located close to the surface and the distance between the UC sensitizer and activator ions was shorter. Addition of an inert shell seemed to decrease the FRET efficiency in the sample with active core (although it showed a significant increase of upconversion efficiency), which could be explained by an increase in FRET donor-acceptor distance.

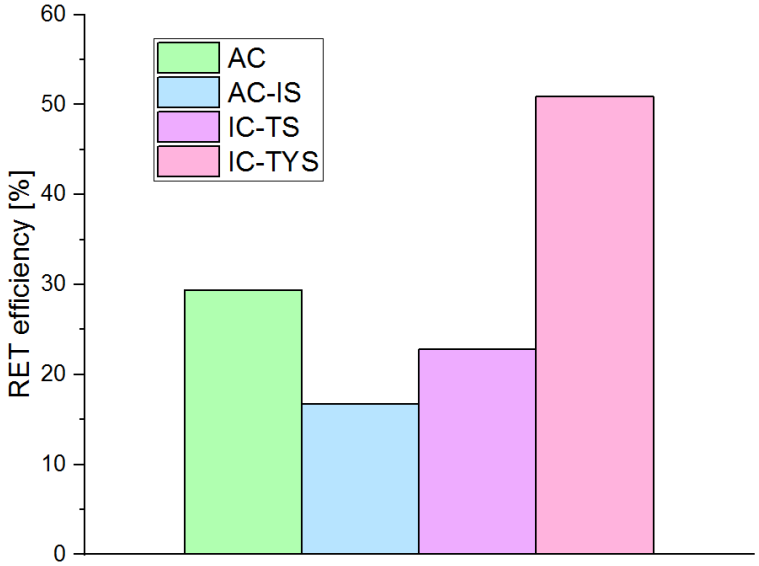

Figure 39. FRET efficiencies calculated from the short components of decay lifetimes of blue emission band of the UCNP-dye system. Equation 18 was used to calculate the efficiencies.

4.4.5 Summary and conclusion

Thus, in these chapters we have optimized and evaluated a new synthesis route with Therminol®66 as a co-solvent, resulting in sub-10 UCNP with better photophysical properties and very precise control over their size. We have shown the advantages of adding a passivating $NaYF_4$ shell to the Tm^{3+}-doped core UCNP and achieved precise control over its thickness as well (less than 2 nm). The photophysical properties of core and core-shell UCNP synthesized by this method were described in detail.

We have also investigated several samples of core-shell and core-only UCNP on the topic of energy transfer to DBD-6, which belongs to the novel class of DBD dyes. This energy transfer pair is particularly interesting, because it does not only consist of the FRET donor and acceptor, but also involves the complex process of energy exchange between the sensitizer and the activator within the nanoparticles as the first step of this energy transfer, increasing its complexity manifold.

Basic investigations of the upconversion behaviour of the four different UCNP species revealed AC-IS particles to be the brightest due to the $NaYF_4$ inert shell protecting Tm^{3+} ions from quenching by environment (this comparison was made at identical measurement conditions with respect to laser excitation and UCNP concentration). UCNP with Tm^{3+} ions only in the shell (IC-TS and IC-TYS) have shown the lowest overall brightness, but their luminescence lifetimes were unexpectedly high. Similar phenomenon was described in [169].

The possibility of FRET between UCNP and the DBD-6 attached to their surface was contemplated, suggested by significant decreases in the blue/reference band ratios in samples labelled with the dye. FRET efficiencies were calculated from luminescence decay data and IC-TYS nanoparticles presented the highest FRET efficiency despite the low brightness of the

sample. The addition of an inert shell decreased the efficiency of the active core UCNP almost in half.

In this study, the DBD-6 dye was designed to substitute OA with minimal effect on the capping agent structure. It is therefore attractive to assume that DBD-6 is oriented parallel to the OA molecules. As a result, the transition dipole moment of the dye (Figure 33) would be placed "tangentially" relative to the UCNP surface, which can explain why the experimentally found FRET efficiency always tends to be smaller than the ones that are calculated based on the photophysical parameters. Besides, a dipole-dipole interaction was assumed when calculating, which is probably not the best approximation for lanthanide ions. Given the complexity of the system discussed above, theoretical calculations are limited by the fact that a number of parameters are not fully known.

4.5 Cell imaging with UCNP

Despite the ever growing interest and amount of research in the field, preparation of small hydrophilic UCNP with reasonably high colloidal stability still presents a challenge [41], [90], [178]–[180]. It has been shown that among other difficulties related to implementing of UCNP in life sciences, the bioapplication of UCNP can be compromised due to their partial dissolution in aqueous solutions including buffers used for biological studies, e.g. PBS [39], [148], [181].

4.5.1 Functionalizing of UCNP with Customized Mussel Protein (CMP)

The UCNP used for further surface modification experiments were $NaYF_4$:Yb^{3+}(19%),Tm^{3+}(1%)@$NaYF_4$ core-shell particles with a diameter of 8.6±1.5 (described in detail in the previous chapter) (Figure 25).

In collaboration with Dr. Leixiao Yu from prof. Haag's group in the Freie University Berlin, we got a customized bioinspired amphiphilic block copolymer ligand that would allow to obtain water-soluble, stable UCNP with a possibility of further labelling. This polymer was inspired by both blood protein adsorption and mussel adhesion. It is reported to form a universal monolayer coating of just several nm that can be applied to substrates of any size, shape or composition [182]. It offers several accessible functionalities for further modification and is inert to the adsorption of multiple polymer layers [182]. The structure of the copolymer, which we will henceforth refer to as customized mussel protein, or, CMP, can be seen in Figure 40.

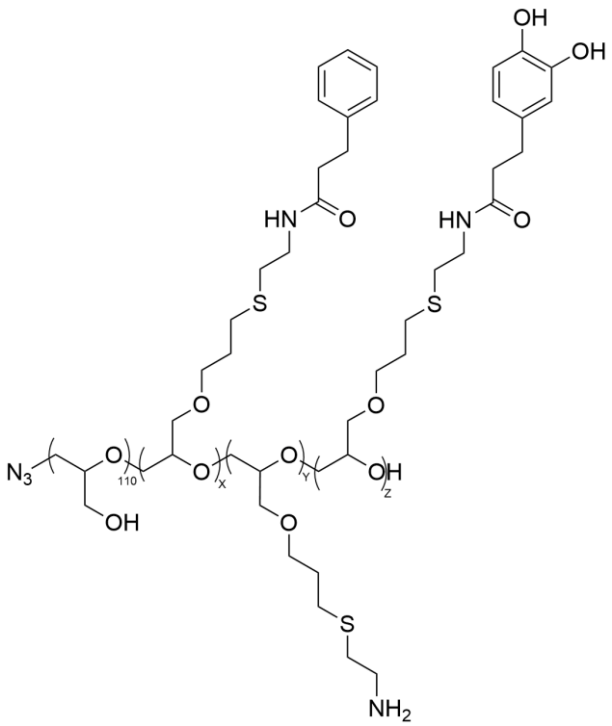

Figure 40. Customised Mussel Protein (CMP). Here, x =5, y = 5, z = 2

In this polymer, the polyglycerol block (which has about 110 repeat units) serves as a hydrophilic domain, the poly(allyl glicydyl ester) (12 repeat units) is the anchor domain, the

catechol groups are involved in hydrogen- or coordinative bonding on polar surfaces, or they can act as hydrophobic domains along with the phenyl groups to anchor on nonpolar surfaces. Amine groups have two functions: displacing the hydrated cations from the mineral surfaces and thus stabilizing the coatings, and increasing the cross-linking efficiency. The N_3-group serves as a functional site for further modification [182].

In order to perform the surface functionalization of UCNP with CMP, first it was necessary to strip off the oleic acid capping from the nanoparticles. For that, they were incubated in MilliQ water with pH 2 for an hour and later repeatedly washed. Afterwards, CMP was bound to the surface of ligand-free nanoparticles by dropwise addition of UCNP in MilliQ water to the CMP solution under stirring and later washed repeatedly to remove the excess polymers.

The resulting CMP-covered nanoparticles (UCNP@CMP) were well soluble in an aqueous buffer (MOPS, pH 7,4), and, despite some inevitable cross-linking of the polymers during the synthesis leading to the formation of minor UCNP@CMP agglomerates, it was possible to store them at 4°C over weeks without further agglomeration (Figure 44, Table 12).

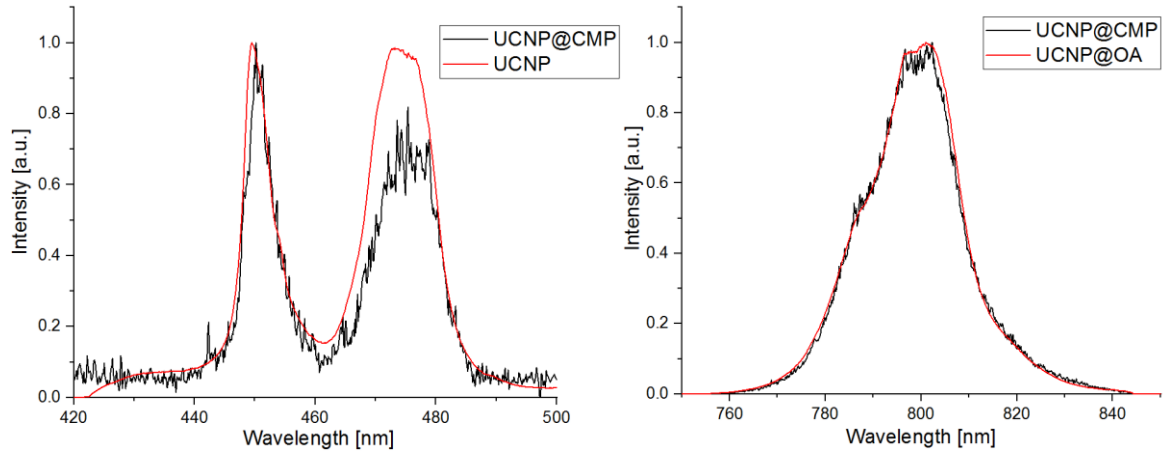

Figure 41. Normalized upconversion emission intensities of $NaYF_4:Yb^{3+},Tm^{3+}$@$NaYF_4$@CMP nanoparticles in MOPS buffer (pH 7.4) and $NaYF_4:Yb^{3+},Tm^{3+}$@$NaYF_4$ in cyclohexane (red), upon pulsed excitation (laser power 54.7 mW) at 976 nm. Blue (B1) and (B2) (left) and near-infrared (NIR) (right) emission bands are shown.

The luminescent properties of CMP-modified UCNP are summarized in Figure 41 and Table 12. It can be seen that the luminescence decay times of the B1 and B2 bands decreased compared to the oleic acid-capped UCNP of the same composition, while the decay time of the NIR band increased. The shapes of UCNP@CMP emission bands resemble those of OA-capped UNCP, although the B1/B2 ratio was slightly higher in hydrophilic UCNP (Table 12). The lower signal-to noise ratio is due to a much lower concentration of UCNP@CMP.

4.5.2 Functionalizing of UCNP with phospholipids

Another method of surface functionalization of UCNP, which proved to be even simpler and faster in preparation, was a protocol of covering the UCNP with phospholipid named 1,2-dioleoyl-sn-glycero-3-phosphocholine (DOPC) (Figure 42). The procedure consisted of drying a small amount of OA-capped UCNP in cyclohexane under a flow of nitrogen, then adding an

aliquot of DOPC in ethanol and diluting with MOPS buffer (pH 7.4) followed by sonication. The resulting phospholipid-modified UCNP (UCNP@PL) are stable in buffer for a couple of days. The agglomeration was also minor (Figure 44).

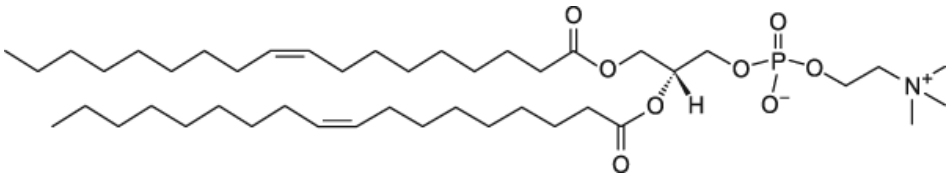

Figure 42. 1,2-dioleoyl-sn-glycero-3-phosphocholine (DOPC)

The properties of the resulting hydrophilic UCNP are summarized in Figure 44 and Table 12. In this sample, the shapes of the emission bands are also similar to those of OA-capped UNCP and UCNP@CMP, with the highest B1/B2 intensity ratio; and the higher noise is also due to a much lower concentration of UCNP@PL.

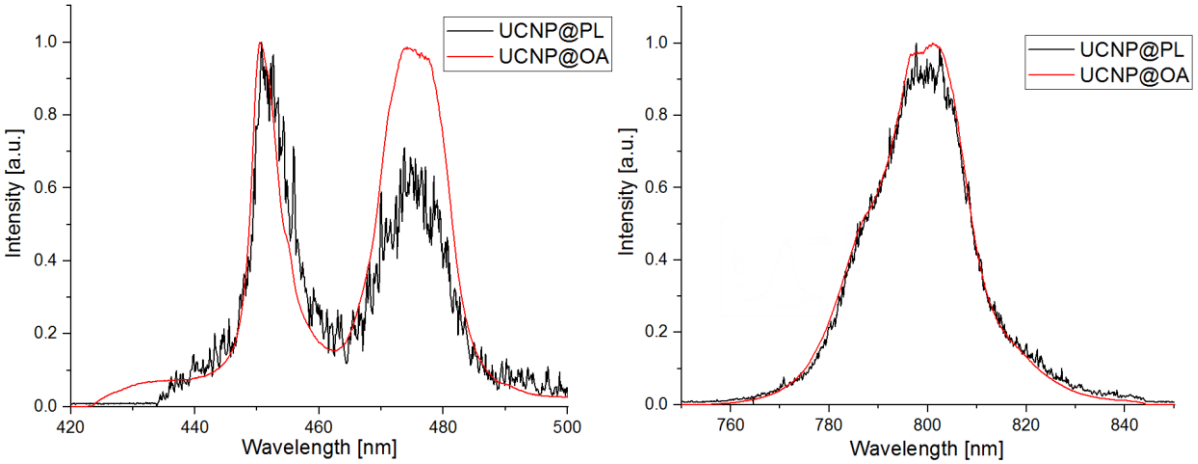

Figure 43. Upconversion emission spectra of $NaYF_4:Yb^{3+},Tm^{3+}$@$NaYF_4$@PL nanoparticles in PBS buffer (pH 7.4) (black), and $NaYF_4:Yb^{3+},Tm^{3+}$@$NaYF_4$ in cyclohexane (red), upon excitation at 976 nm upon pulsed excitation (laser power 52.4 mW) at 976 nm. Blue (B1) and (B2) (left) and near-infrared (NIR) (right) emission bands are shown.

As can be noticed from Table 12, luminescence decay times of both Tm^{3+} blue emission bands have decreased in both hydrophilic UCNP samples. This phenomenon is usually attributed to the water quenching of the UCNP luminescence, although here the NIR bands of both samples have increased compared to UCNP@OA. Overall, UCNP@CMP have shown slightly higher luminescence lifetimes compared to UCNP@PL, which could potentially offer a slight advantage.

TEM investigation of the CMP- and PL-modified UCNP has indicated the preserved structure and size of the nanocrystals (8.1 ± 1 for UCNP@CMP and 10.5 ±1 for UCNP@PL). This corresponds well to the sizes of non-functionalized UCNP (Table 9) and the difference in diameter between the samples is explained by the fact they were taken from different batches. There was an excess of ligands in both cases, but that parameter can be further optimized by altering the ligand to UCNP ratio.

Table 12. Luminescence decay times with respective fractions (in parentheses) of $NaYF_4:Yb^{3+},Tm^{3+}@NaYF_4$ UCNP upon 976 nm excitation in MOPS buffer (pH 7.4) for UCNP@CMP and UCNP@PL and cyclohexane for UCNP@OA (τ_1 is the short component of the luminescence decay time, τ_2 is the long component and τ_{av} is the average time of luminescence decay (Equation 9).

Emission band with respective transition	τ, μs	UCNP@CMP	UCNP@PL	UCNP@OA
451 nm $^1D_2 \rightarrow {}^3F_4$	τ_1	119 (96%)	57 (64%)	126 (80%)
	τ_2	191 (4%)	194 (36%)	477 (20%)
	τ_{av}	**144**	**107**	**197**
481 nm $^1G_4 \rightarrow {}^3H_6$	τ_1	144 (100%)	113 (45%)	215 (61%)
	τ_2	-	330 (55%)	490 (39%)
	τ_{av}	**144**	**232**	**323**
800 nm $^3H_4 \rightarrow {}^3H_6$	τ_1	319 (87%)	233 (83%)	162 (64%)
	τ_2	680 (13%)	540 (17%)	371 (36%)
	τ_{av}	**368**	**283**	**237**
B1/B2 band ratio (area)		**0.68**	**0.97**	**0.51**

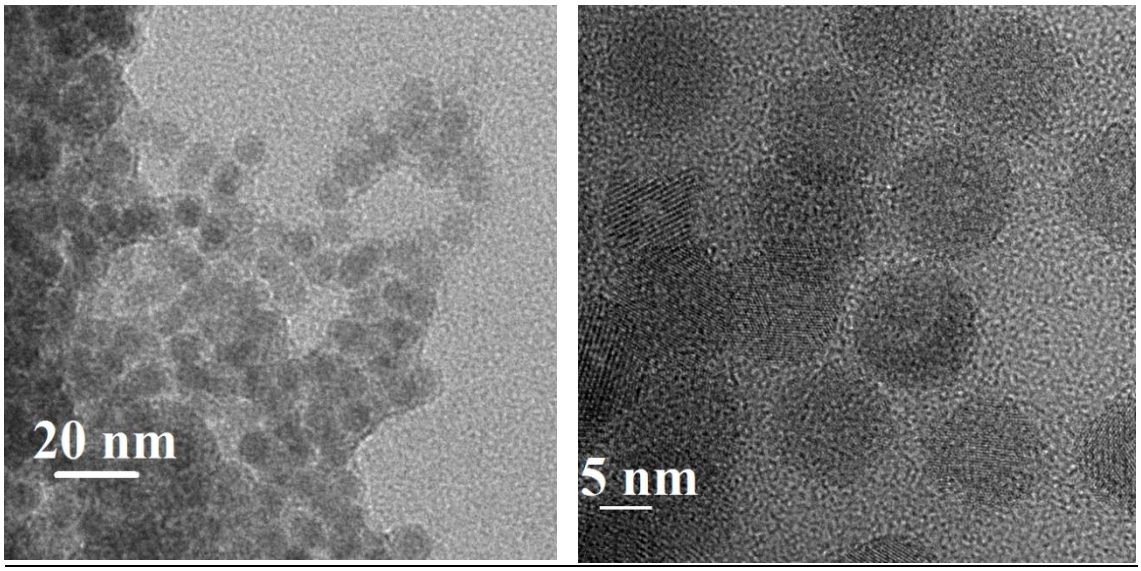

Figure 44. TEM images of $NaYF_4:Yb^{3+},Tm^{3+}@NaYF_4$ UCNP: CMP-functionalized (left), PL-functionalized (right). Acceleration voltage 200 kV.

4.5.3 Synthesis of the liposomes

Before using the upconverting nanoparticles directly in cells, it was necessary to test the linking *via* the copper-free click-chemistry on a model. Copper-free click chemistry, a cycloaddition of an azide group to cyclooctynes, was selected due to its versatility, simplicity, and most importantly, non-toxicity to living cells due to the lack of copper [112]. Customized mussel protein offers a readily reactive azide group, and the phospholipid-modified UCNP were modified to contain an azide group by adding 1% of 18:0 azidoethyl phosphatidylcholine to DOPC solution during preparation.

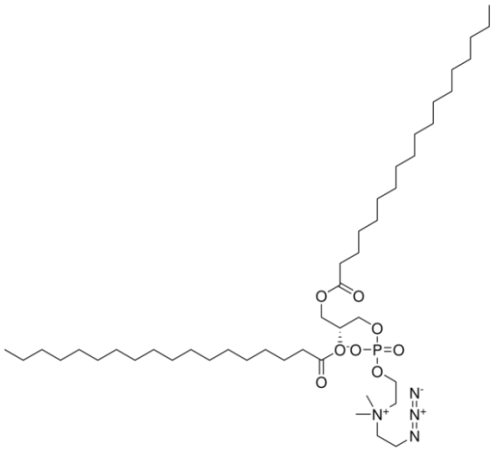

Figure 45. 18:0 azidoethyl phosphatidylcholine

As a model for living cells, we synthesized liposomes that consisted of a chicken egg-derived L-α-phosphatidylcholine (Egg-PC) (98.9%), Vybrant^{TM} DiD Cell-Labeling Solution (DiD dye) (0.1 mol%), and a cyclooctyne-containing 1,2-distearoyl-sn-glycero-3-phosphoethanolamine-N-[dibenzocyclooctyl (polyethylene glycol)-2000] ammonium salt (DSPE-PEG(2000)-DBCO, later in the text we will refer to it as DBCO for shortness) (1%). The control sample didn't contain DBCO and had 99.9% of Egg-PC. The absorption maximum of the DiD dye was at 630 nm and the emission maximum – at 660 nm.

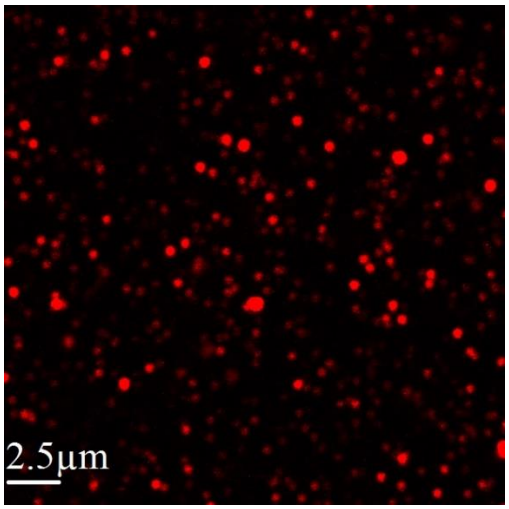

Figure 46. Confocal micrograph of the liposomes. λ_{ex} = 633 nm, λ_{em} = 654 – 740, image width: 24.42 µm.

The resulting liposomes had a diameter of approx. 600 nm, and provided bright emission at wavelengths above 640 nm upon excitation at λ_{ex} = 633 nm (Figure 46).

a)

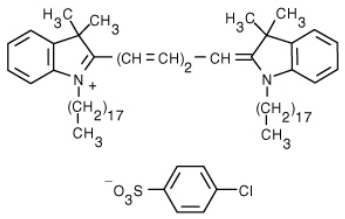

b)

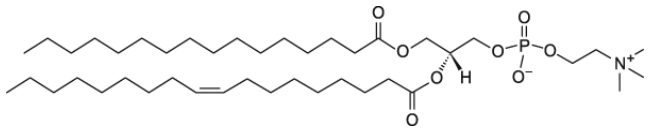

c)

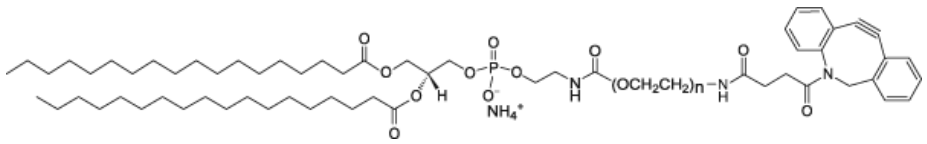

Figure 47. DID-dye (a), Egg-PC (b), DSPE-PEG(2000)-DBCO (c)

4.5.4 Downshifting of UCNP

In order to obtain images of the liposomes and, subsequently, the cells, a confocal microscope with an argon laser (λ_{laser} = 488 nm) was used. As described in literature [183]–[185], Tm^{3+} has been proven effective not only as an activator, but also as a sensitizer, for example, for Gd^{3+}/Eu^{3+} quantum cutting couples (QC, the conversion of a high energy photon into two or more low energy ones) [183]. The potential of Tm^{3+} excitation at 488 nm, which corresponds to the $^3H_6 \rightarrow {}^1G_4$ transition of Tm^{3+}, has also been used in fluorosilicate glasses and Y_2O_3 transparent ceramics, where it was coupled with Yb^{3+} [184], [185]. The phenomenon of downshifting, a process where a photon with higher energy is converted into one photon of lower energy, has also been described for Tm^{3+}-doped materials such as glasses [186], [187] and in UCNP for multimodal imaging [188].

We recorded luminescence spectra of the Tm^{3+}, Yb^{3+}-doped UCNP to test the possibility of exciting them at 488 nm (Figure 48). In the inset the spectrum taken with an initial delay of 500 ns is shown, and it can be seen that there's a big contribution around 600-700 nm from the phosphor screen emission, which is an artefact of the iCCD camera system present a short initial delay times for samples with high scattering background. In order to see the "clean" spectrum (Figure 48), i.e., neutralize the phosphor screen contribution, we installed a 520 nm long pass filter in front of the CCD camera and established a delay of 5 µs in order to remove/reduce the amount of scattered excitation light reaching the detection system.

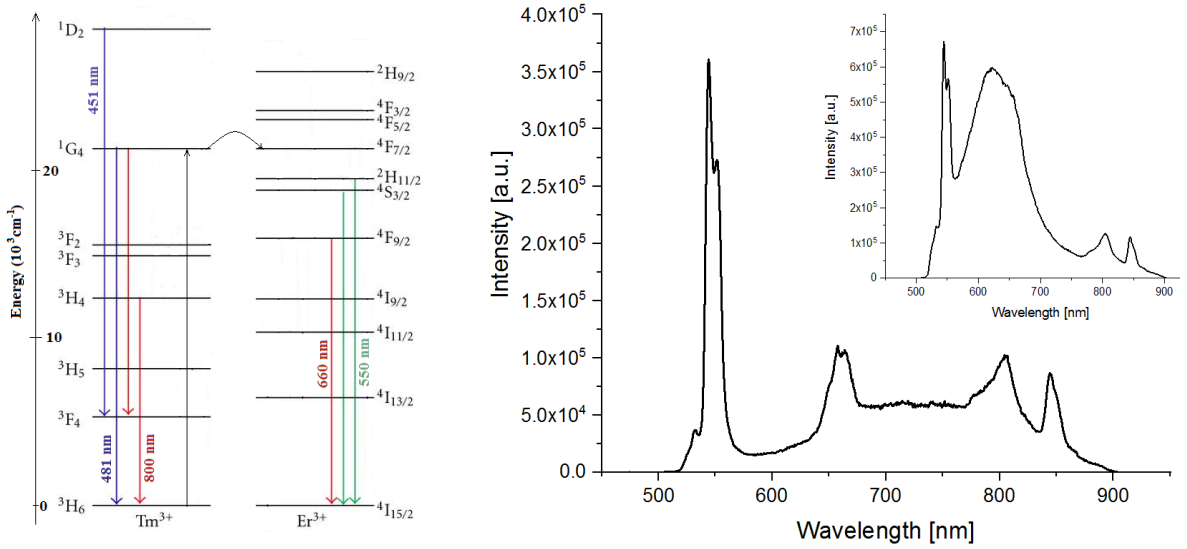

Figure 48. Left: Schematic energy level diagram for the main emission transitions of Tm^{3+} and Er^{3+} upon excitation at λ_{ex} = 488 nm (represented by a straight black arrow). The full lines pointing downwards represent emission, the bent black line represents possible energy transfer from Tm^{3+} to Er^{3+}. Right: Luminescence emission spectra of $NaYF_4$: Yb^{3+}, Tm^{3+}@ $NaYF_4$ nanoparticles in cyclohexane upon excitation at 488 nm upon pulsed excitation (laser power 281 mW). Gate delay is 5 μs (main image) and 500 ns (inset).

As can be seen from the spectra, there are several emission bands: at 550 nm, 660 nm, 800 and 855 nm. The band at 800 nm can be explained by the $^3H_4 \rightarrow {}^3H_6$ transition of Tm^{3+}, and the bands at 550 nm, 660 nm, and 855 nm can be attributed to Er^{3+}'s $^4S_{3/2} \rightarrow {}^4I_{15/2}$, $^4F_{9/2} \rightarrow {}^4I_{15/2}$, and $^4S_{3/2} \rightarrow {}^4I_{13/2}$, respectively. Er^{3+} ions are always present in $NaYF_4$: Yb^{3+}, Tm^{3+} UCNP in trace amounts due to impurities of the Ln^{3+} salts used for the synthesis.

On the schematic energy level diagram presented in Figure 48 the supposed transitions leading to the emission bands observed on the luminescence spectra are shown. Due to the close proximity of $^1G_4$ energy level of Tm^{3+} to the $^4F_{7/2}$, $^2H_{11/2}$, and $^4S_{3/2}$ levels of Er^{3+}, an energy transfer process from the exited Tm^{3+} to Er^{3+} is possible, leading to sensitized emission of Er^{3+}.

This fortunate feature of downshifting in the $NaYF_4$:Yb^{3+},Tm^{3+}@$NaYF_4$ UCNP can be further used for excitation at λ_{ex} = 488 nm and imaging on the standard confocal microscope with argon-ion laser without the need for mounting an additional NIR laser for the preliminary experiments.

Similar phenomena were observed when exciting the UCNP at λ_{ex} = 560 and 633 nm, but the intensity of the emission bands was much lower than that at λ_{ex} = 488 nm. These excitation wavelengths correspond to the $^4S_{3/2} \rightarrow {}^4I_{15/2}$ transition of Er^{3+} (560 nm) and $^4F_{9/2} \rightarrow {}^4I_{15/2}$ transition of Er^{3+} or $^3H_6 \rightarrow {}^1G_4$ of Tm^{3+} (633 nm). The resulting bands could be a result of the direct excitation followed by relaxation of Er^{3+} ions or of the energy transfer between Tm^{3+} and Er^{3+} ions, thus, the brightness could most likely be increased with the increase of Er^{3+} doping concentration.

4.5.5 *Copper-free click-chemistry bonding between the liposomes and UCNP*

One necessary step before introducing the UCNP into living organisms was to test the microscopy setup and the planned bonding reactions on models, in this case dye-labelled liposomes. The characterization was carried out using the confocal microscope (Zeiss LSM780 system) coupled to a 488-nm argon laser and a 561-nm diode laser and a C-Apochromat 40x/1.2 W Korr M27 objective.

The reaction was performed according to the procedure described in [142]. The liposomes containing the DSPE-PEG (2000)-DBCO (the cyclooctyne necessary for the reaction) were incubated with the N_3-labeled UCNP (either functionalized with the CMP or with a lipid layer) for 1 to 2 hours at room temperature under mild shaking (Figure 49). A control experiment with lipid-covered UCNP not containing azide functionalities was performed.

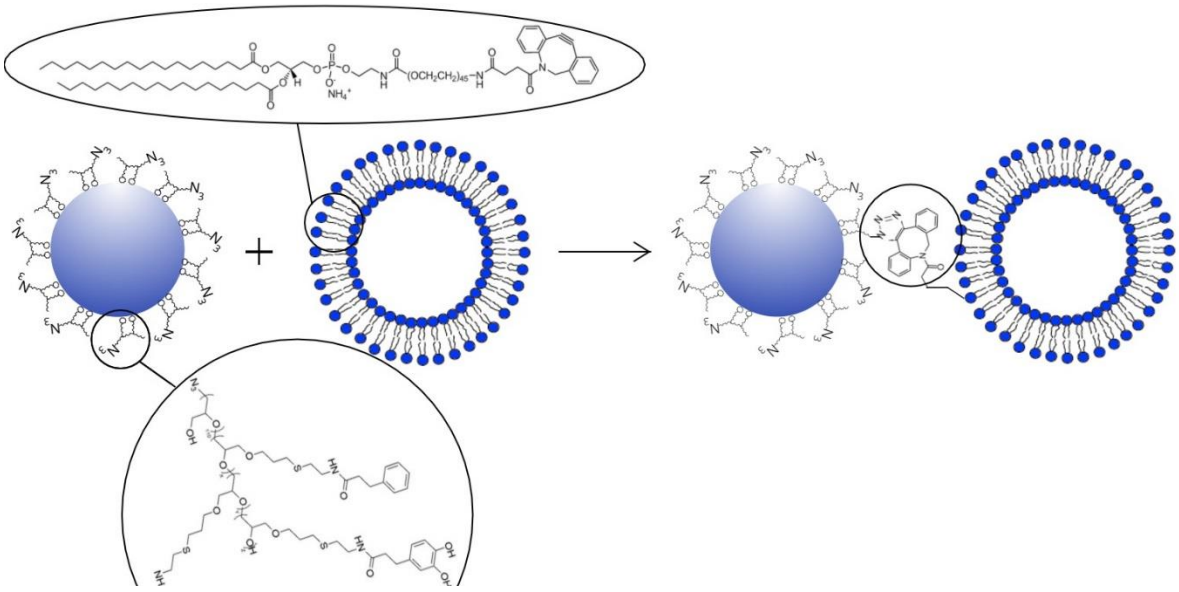

Figure 49. Schematic representation of the copper-free click reaction between the N_3-functionalized UCNP and a DSPE-PEG(2000)-DBCO-containing liposome

After the incubation period, the samples were examined on the confocal microscope and the share of the attached UCNP-liposome pairs was determined and compared. The attachment was considered successful if the UCNP and the liposomes were in very close proximity (touching) or overlapping on the image. The criteria for attachment were kept constant for all the images and the attachment share was calculated based on the analysis of about 20 images for each sample (over 300 UCNP). The rate of attachment was calculated as the ratio of the UCNP attached to the liposomes to the total amount of the UCNP.

An example of a micrograph used for the calculations is presented in Figure 50. The amount of UCNP on the image is significantly smaller than that of the liposomes, thus, we used UCNP as a framework for our calculations.

Our calculations have shown that the ratio of attachment in the sample with liposomes containing DBCO was 55%, while for the control sample is was only 20%. This can be considered a significant difference to assume the success of the click chemistry reaction,

although, elongating the incubation time of the reaction would most likely increase the yield of the reaction.

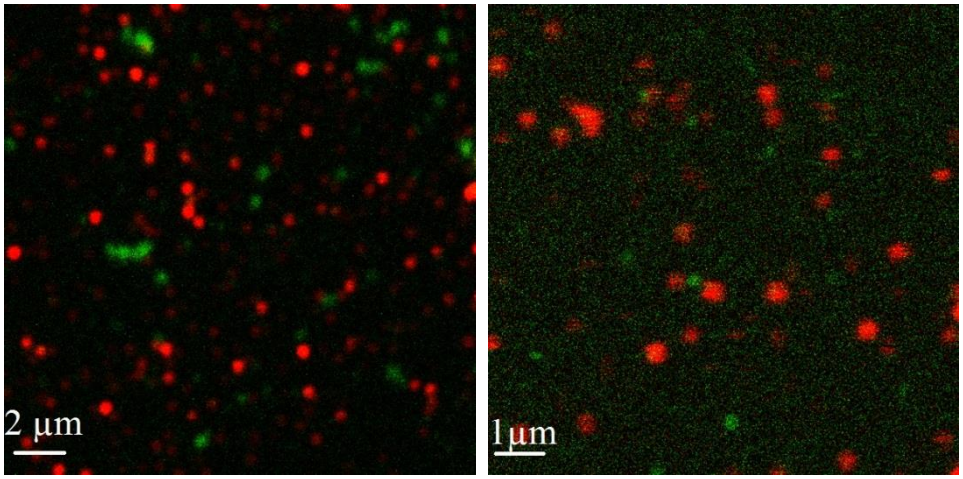

Figure 50. Confocal micrographs illustrating liposome click-chemistry bonding to UCNP@PL. Control sample (liposomes not containing DBCO) is shown on the left, and the sample with DBCO on the right. Liposomes (red) were recorded at λ_{ex} = 633 nm, λ_{em} = 654 – 740, and the UCNP (green) – at λ_{ex} = 488 nm, λ_{em} = 495 – 595 nm. Image sizes are 16.47 µm (left) and 10.79 µm (right).

The same experiment was performed for the CMP-coated UCNP. The N_3-group present in CMP is available for the cycloaddition. The reaction, the measurements and the calculations were performed in the exact same way as for the lipid-functionalized UCNP. Here, the yield in the sample with liposomes containing DBCO was 71%, while for the control sample is was also about 20%. The results are summarized in Table 13.

Table 13. Copper free click-chemistry reaction yields of UCNP@CMP and UCNP@PL and liposomes with (sample) and without (control) DBCO, calculated from micrographs (e.g., Figure 50).

	Control	**Sample**
UCNP@CMP	20%	55%
UCNP@PL	20%	71%

4.5.6 Cell experiments with UCNP

Before performing the bonding experiments between the UCNP and the cells, it was necessary to make sure that the optical settings of the system would allow for a clear distinction between the autofluorescence of the cells and the luminescence coming from UCNP. For that, a series of tests on several cell types were performed and the cells that showed the least autofluorescence in the areas of interest were human embryonic kidney cells grown in tissue culture, or HEK293T. Further experiments were performed on HEK293T.

Since the UCNP have shown emission both under excitation at 488 and 633 nm, and the cells have shown no autofluorescence when excited at 633 nm, it was decided to record the images at both excitation wavelengths to exclude the autofluorescence from the cells.

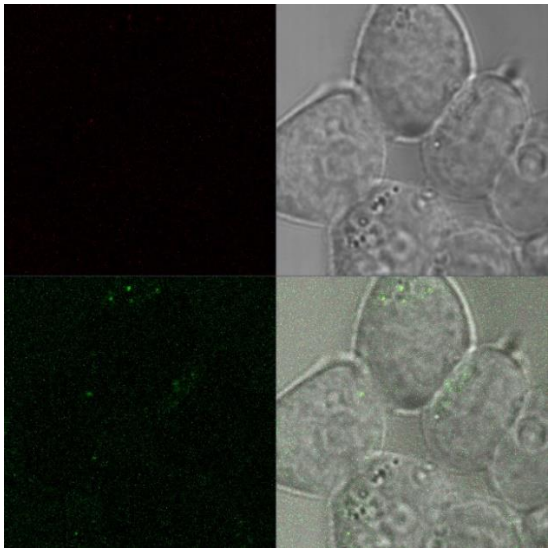

Figure 51. Confocal micrograph of HEK293T cells. Top left: λ_{ex} = 633 nm, λ_{em} = 654–740; top right: bright field image, bottom left: λ_{ex} = 488 nm, λ_{em} = 495–595 nm, bottom right: superposition. Image size 37.51 µm. Height: 6.1 µm.

In Figure 51, a typical image of the HEK293T cells is shown. The average height of the cell is about 10 µm, and the images are taken at the glass surface and then moving up the z axis with an interval of some µm until reaching the surface of the cell. From the Figure 51 it can be seen that some autofluorescence comes from the cells in the green channel (λ_{ex} = 488 nm) but there is no signal coming from the red (λ_{ex} = 633 nm) channel. These conditions allow for further examination of the interaction between the cells and the UCNP on the confocal microscope.

The following step was the introduction of the UCNP functionalized with either lipids or CMP to the cells and the observing of their interaction. The experiment was carried out in MOPS buffer (pH 7.4). After the introduction of the UCNP to the cells, an incubation time of 15-20 minutes was established to assure the possible binding of the UCNP to the cells. About 30 images were analyzed for each UCNP type.

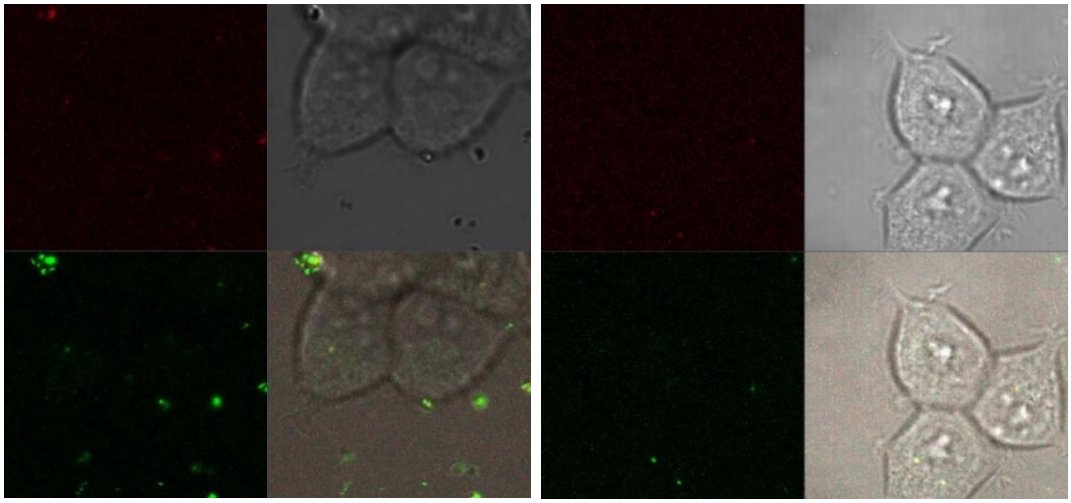

Figure 52. Confocal micrographs of HEK293T cells with UCNP@PL (left image) and UCNP@CMP (right image). On each micrograph: top left: λ_{ex} = 633 nm, λ_{em} = 654–740; top right: brightfield image, bottom left: λ_{ex} = 488 nm, λ_{em} = 495–595 nm, bottom right: superposition. Image size 49.0 µm. Height: 2 µm (left), 0 µm (right).

In Figure 52, a typical micrograph showing UCNP functionalized with lipids and CMP are shown together with cells. UCNP are clearly visible in both red and green channels (λ_{ex} = 633 and 488 nm, respectively), unlike the autofluorescence of the cells. Most of the particles do not interact with the cells or do not have any special affinity to them after the incubation period, the ones that reach the cells generally do not penetrate the membrane. On the image that shows UCNP@CMP interaction, the two UCNP located seemingly inside the cell are most likely underneath it, because the image is taken at the level of the glass. Thus, from examining of the 30 images for each UCNP type, it can be concluded that there is no specific interaction between the HEK293T cells and the UCNP.

4.5.7 Antibody staining of the cells

After confirming the absence of specific interactions between the cells and the UCNP, an experiment on antibody staining was carried out. The final goal of the study was to attach a DBCO-labelled antibody, labelled with a UCNP carrying N_3-functionalities via click chemistry, to the surface of the cells (Figure 53).

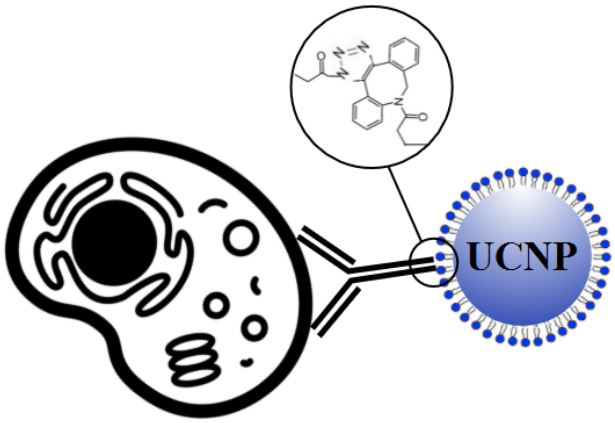

Figure 53. Schematic representation of the desired final product: an antibody (e.g. integrin beta), labelled with a PL-functionalized UCNP via click chemistry, attached to a cell (e.g. MDCK-II).

For testing the principle and making sure the antibody staining really works, first an experiment using a primary and a secondary antibody labelled with a dye (Alexafluor ® 488) was carried out.

The experiment included two primary antibodies (Ab-1): VE cadherin (vascular endothelial cadherin) antibody, and Integrin β1, both mouse monoclonal antibodies specific to proteins on the cell surface. The cells used for the experiment were Madin-Darby Canine Kidney (MDCK-II) cells. The secondary antibody (Ab2), which specifically binds to the primary antibodies, was Goat Anti-Mouse IgG H&L modified with (Alexa Fluor®488) for the detection of the staining on the microscope.

There were also two control samples: one of them contained no antibodies at all (C0), and the other one only the secondary antibody, to exclude any unspecific binding of it to the cells (C2).

About 20 images of each sample were analyzed and an overview example is shown in Figure 54.

From Figure 54 it is easy to see that the control sample with no Ab showed almost no fluorescence, while the C2, with the dye-labelled secondary antibody added to the cells, showed more, but still unspecific, fluorescence under λ_{ex} = 488 excitation. Both samples with Ab-1 and Ab-2 showed bright luminescence coming from the Alexafluor®488 located at the membrane of the cells on all images that were taken. This is a clear indication of a successful antibody staining and the proof that the principle is working and can be taken further to incorporate UCNP-Ab conjunctions into the same experiments.

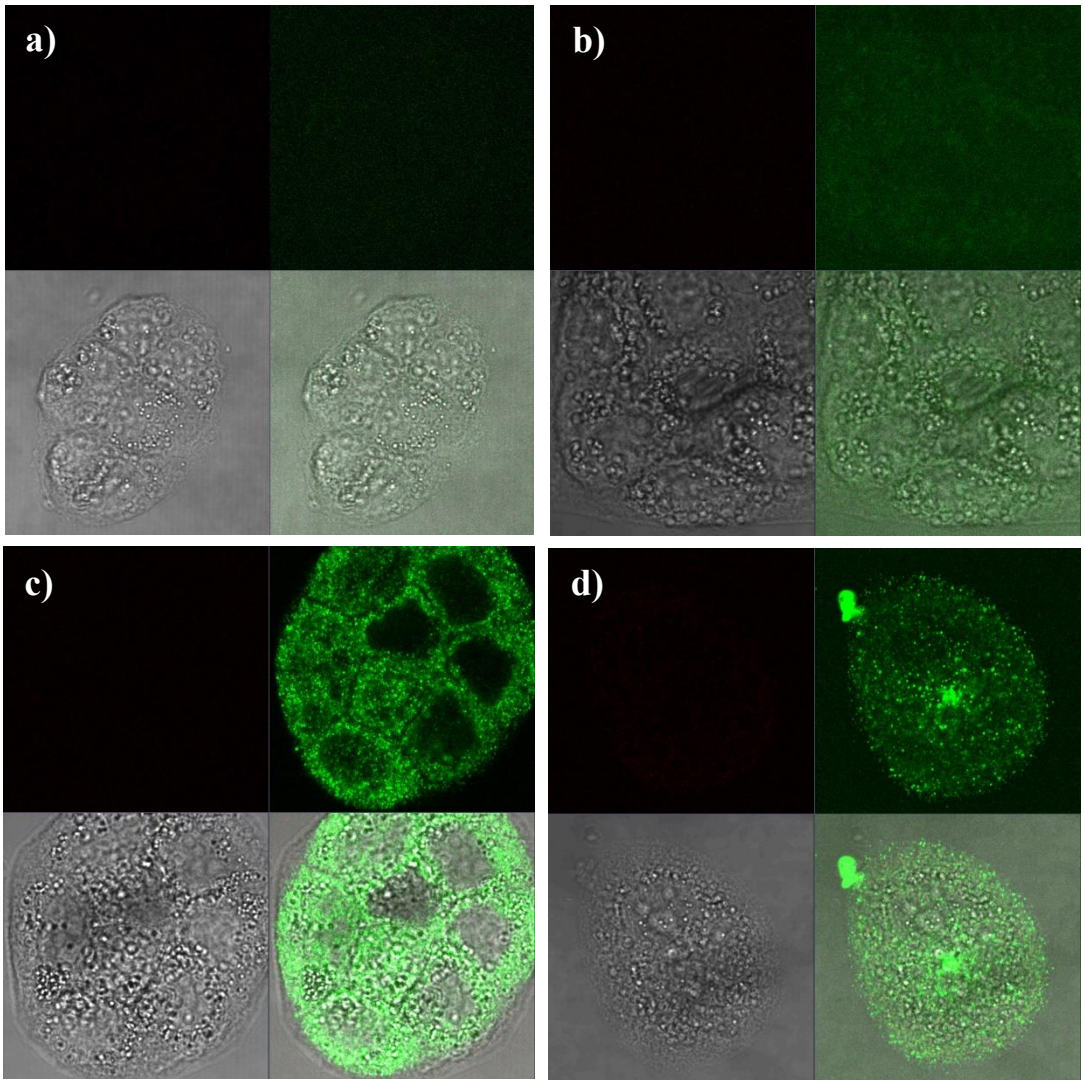

Figure 54. Confocal micrographs of MDCK-II cells after antibody staining. Control without antibodies (a), control with Ab2 (b), VE cadherin + Ab2 (c), Integrin β1 + Ab2. On each micrograph: top left: λ_{ex} = 633 nm, λ_{em} = 654–740; top right: bright field image, bottom left: λ_{ex} = 488 nm, λ_{em} = 495–595 nm, bottom right: superposition. Image size 51.5 µm. Height: 1 µm.

As a conclusion, in this chapter we have prepared the ground for further cell imaging with $NaYF_4$-based UCNP: firstly, we developed two synthesis procedures to hydrophilize the OA-capped UCNP using phospholipids and a polymer. Their photophysical and structural

properties were not affected and their colloidal stability was rather high. Secondly, we have implemented dye-labelled liposomes for the preliminary experiments of copper-free click chemistry and confocal imaging of the UCNP in biological conditions. Thirdly, we described the lesser known downshifting properties of Yb^{3+}, Tm^{3+}-doped UCNP with traces of Er^{3+} and utilized them for on-site imaging on a conventional setup without the need to build new complicated systems for NIR excitation of the UCNP. Lastly, we have looked into the interactions of the water-soluble UCNP with HEK293T cells and tested the principles of the antibody staining using two primary and one dye-labelled secondary antibodies on MDCK-II cells.

As a logical continuation of this work, the further steps would be the modification of the antibody staining experiment, using the DBCO-labelled antibodies connected via click-chemistry to N_3-functionalized UCNP, and mounting of a microscopy system coupled to a 976 nm laser for direct excitation of the UCNP and colocalization experiments. This work will be continued in the nearest future and the results described in this chapter will serve as a solid foundation for the application of the described ideas in the experimental setting.

4.5.8 Summary and conclusion

The use of UCNP for cell and tissue imaging has been reported in literature and the interest has been steady growing over the last decade. Most groups have utilized polymer (usually PEG) [189]–[192] – modified UCNP, silica- [193], or block-copolymer - coated UCNP [194], or oxidized the OA coating [195] for further attachment. The groups who used antibody assays to attach the UCNP to the cells usually take advantage of the EDC/NHS activation, biotin-streptavidin conjugation or use the thiol groups to attach the antibodies to the UCNP [85], [192], [195]. They also usually rely on confocal microscope systems equipped with a 980 nm excitation source which requires technical manipulations and such systems are usually not commercially available. In comparison, the suggested plan includes a novel UCNP ligand (CMP) and functionalization with PL, which to date has been underrepresented in literature. Another aspect that distinguishes the presented procedure is using the copper free click chemistry approach to link antibodies to UCNP, which, to our knowledge, hasn't been done yet, and is described to be non-toxic to living cells and high in yield. And finally, the implication of the downshifting capability of the particles for the on-site imaging before moving to more technically challenging and complicated systems allows for the samples to be easily visualized on virtually any commercially available confocal (or, e.g. TIRF) microscope.

5 Conclusions and perspectives

5.1 ***Summary and Conclusions***

While understanding, integration and application of upconverting nanoparticles (UCNP) in industrial, biomedical and scientific applications has been increasingly broadening and accelerating over the past decades, some questions remain unanswered and some issues unresolved. The motivation for continuing these investigations lays in the promising qualities that UCNP offer. Among those are excitation in the NIR region of the spectra, allowing for deeper tissue penetration, little to no light scattering, and thus a reduced optical background, sharp luminescence bands at tunable wavelengths, possibility for multicolor imaging, no photobleaching, luminescence lifetimes in the µs range, large Anti-stokes shifts, and derivatization flexibility of UCNP surface. For biomedical applications it is extremely important not only to have uniform and regularly sized nanocrystals, but also to provide colloidal stability in aqueous solutions and a possibility for further modification of the UCNP surface.

Current limitations in this field that need to be addressed include the upconversion luminescence efficiency, which usually doesn't exceed 1% for the majority of UCNP, lack of understanding of the processes of energy transfer between the UCNP and other luminescent reporters, numerous functionalization procedures that require organizing and consolidation, as well as the downsides of the existing protocols such as toxicity and agglomeration that have yet to be improved. For *in vivo* studies, the rapid uptake of UCNP by spleen and liver still remains a challenge and the lack of systematic toxicity investigations needs to be addressed. Many of the aforementioned issues are addressed in the presented work.

We have successfully used the solvothermal synthesis method with oleic acid and octadecene as solvents to produce $NaYF_4$: Yb^{3+}, Tm^{3+}, Gd^{3+} upconverting nanoparticles with a varying content of Gd^{3+} (10-50 mol %) and assessed its influence on the structural and luminescence properties. The size and phase-purity of the nanocrystals were studied by transmission electron microscopy (TEM), dynamic light scattering (DLS), and X-ray diffraction (XRD). In-depth photophysical investigation of the nanoparticles was performed via steady-state and time-resolved luminescence spectroscopy, and low-temperature (down to 4 K) studies have been conducted. The ageing (within the period of 24 months) and its effect on structural and photophysical properties of these five UCNP species in cyclohexane has also been studied, which, to our knowledge, has not yet been reported elsewhere. The resulting nanoparticles had a size range of 13-42 nm and showed bright luminescence at 451, 481, and 800 nm upon 976 nm pulsed excitation and luminescence lifetimes in the range from tens to hundreds of µs. While no clear trends of Gd^{3+} contents influence on the properties of UCNP have been detected, the particles have shown their peak size and shape regularity at 30% Gd^{3+}, which also lead to higher luminescence emission intensities and longer luminescence lifetimes. The ageing process has also not shown any drastic effect on the structural and luminescent properties of UCNP, and an occurrence of an Ostwald ripening-like process could be suspected given the increased size gap between the two crystallite subspecies.

The inconclusive influence of Gd^{3+} content on the photophysical properties of the nanoparticles was most likely explained by the insufficient control over such important synthesis parameters as temperature, reaction time and the lack of a fitting solvent, which probably had a larger effect on the resulting UCNP. Thus, an improved synthesis route has been adapted, where Therminol®66, a high-boiling commercially available organic solvent, was used to replace octadecene. The new protocol allowed for production of very regular and homogeneous sub-10 nm UCNP with better photophysical properties and a very precise control over their size. The advantages of adding a passivating sub-2 nm $NaYF_4$ shell to the Tm^{3+}-doped core UCNP were shown, owning to the reduced surface quenching and resulting in much brighter upconversion luminescence.

Förster resonance energy transfer between UCNP and such fluorescent labels as dyes or quantum dots, a process of high interest and a subject of increasing research for applications in biosensing, still requires a deeper understanding of the fundamental processes behind it. Thus, we have investigated the process of FRET between four different species of $NaYF_4$: Yb^{3+}, Tm^{3+} core and core-shell UCNP and a DBD-6, a small organic dye which belongs to a novel class of DBD dyes. This process of energy transfer consists not only of energy transfer between donor and acceptor, but also includes energy exchange between the sensitizer and activator within the UCNP, which makes it extremely complex. The influence of UCNP composition and the proximity of Tm^{3+} ions (donors in the process of FRET) to dye molecules have been assessed. Between the four samples, the brightest UC luminescence was observed in the UCNP with an inert shell around the Tm^{3+}-doped core (AC-IS). UCNP with Tm^{3+} ions only in the shell (IC-TS and IC-TYS) have shown the lowest brightness, while their luminescence lifetimes were unexpectedly high. The possibility of FRET between the UCNP and the dye was suggested by significant decreases in the blue/reference band ratios in samples labelled with the dye. As expected, the highest FRET efficiency was detected in IC-TYS nanoparticles despite the low UCL brightness of the sample. The addition of an inert shell decreased the FRET efficiency of the active core UCNP almost in half.

While the resulting from the improved synthesis procedure UCNP are hydrophobic in nature, it is crucial for biological applications to make them soluble and stable in aqueous solutions. This can be achieved by surface modification processes, which provide UCNP with water dispersibility and at the same time create a platform for further chemical modification possibilities. While the interest and the amount of research in the field is accelerating, preparation of small hydrophilic UCNP with reasonably high colloidal stability remains a challenge. Usually, a polymer (e.g. PEG), silica- or block-copolymer – coatings are used to hydrophilize the UCNP. We have implemented two modification protocols: a quick phospholipid coating of the OA-capped UCNP and a two-step modification with a novel customized block copolymer ligand. The protocols resulted in stable hydrophilic UCNP with no dramatic influence on their luminescent properties.

As a preparation stage for cell experiments, we have performed a series of tests on model liposomes labelled with a fluorescent dye on a confocal microscope system. That was made possible by taking advantage of the lesser known downshifting properties of Yb^{3+}, Tm^{3+}-doped UCNP with traces of Er^{3+}. This process has yet to be studied and described in detail, but it

allows for on-site imaging on a conventional setup without the need to mount new custom-built systems for NIR excitation of the UCNP.

We have tested a non-toxic biocompatible copper-free click reaction between the functionalized UCNP and model liposomes and achieved a statistically significant attachment rate. And finally, we have looked into the interactions of the water-soluble UCNP with HEK293T cells and tested the principles of the antibody staining using two primary and one dye-labelled secondary antibodies on MDCK-II cells. While this work is yet to be continued, we have provided a solid base for future investigations on cell imaging using hydrophilic UCNP with means that have not yet been reported in literature.

5.2 Perspectives

No research is complete without contemplating the possible ways of expansion and development of the studied systems in order to achieve deeper understanding of the indicated problems.

The logical continuation of the studies conducted in this thesis can go two ways: gaining of a deeper fundamental understanding of the photophysical basics of the upconversion and energy transfer processes, and further improvement of the optical systems and UCNP architecture and surface chemistry for applications in bioimaging.

In this work we have done investigations on the influence of the Gd^{3+} content on the photophysical properties of the UCNP, which were somewhat exacerbated by the lack of precision provided by oleic acid – mediated synthesis. In order to make the studies more precise and the results more coherent, the new synthesis protocol with Therminol®66 as a solvent, where a precise control over the UCNP properties is achieved, could be implemented and the experiment repeated. This would require a considerable amount of time and effort and therefore was out of the scope of the presented work, but could be beneficial in the future.

The results obtained by the investigation of the process of FRET could be expanded to the water-soluble dye-labelled UCNP, as FRET is usually used for detection of trace amounts of biochemicals, which requires a transfer of UCNP to aqueous solutions. Here, some complications should be taken in consideration, such as increased Förster distances due to the thickness of the ligand layer, surface quenching, which usually is higher in water-based media, and possible agglomeration due to ligand cross-linking, which is still a problem in most surface-functionalized UCNP. The aforementioned parameters make the system even more complicated and, therefore, signifies a specific need for in-depth investigation of such systems.

The little studied process of downshifting in $NaYF_4$: Yb^{3+}, Tm^{3+} UCNP can be examined in more detail: to understand the underlying processes, a more detailed study of photophysical behavior (e.g., power dependent measurements, decay kinetics, etc.) needs to be performed.

And, finally, in this study we have laid the ground work for the application of UCNP in cell imaging. In order to take this investigation forward, several steps need to be accomplished. Firstly, an optical system combining a TIRF or a confocal microscope and a 980-nm laser excitation source needs to be mounted, which presents a certain challenge given the lack of commercially available solutions for such systems. Secondly, the click-chemistry reaction between the primary antibody and the UCNP has to be carried out and its chemical yield needs to be assessed. In case of the successful labelling of the antibodies with the UCNP, the next step would be the antibody staining of the cells. In case of the successful development of this project, the use of UCNP as biomarkers could be extended to other biological objects, such as viruses or tissues, or used on cell organelles for metabolite detection.

6 Appendix

6.1 Abbreviations

A – acceptor
Ab – antibody
Ab-1 – primary antibody
Ab-2 – secondary antibody
AC – active core UCNP
AC-IS – active core inert shell UCNP
B1 – blue luminescence band of Tm^{3+} at 451 nm ($^1D_2 \rightarrow {}^3F_4$ transition)
B2 – blue luminescence band of Tm^{3+} at 481 nm ($^1G_4 \rightarrow {}^3H_6$ transition)
CMP – customized mussel protein
D – donor
DBCO – DSPE-PEG(2000)-DBCO
DBD – [1,3]dioxolo[4,5-f][1,3]benzodioxole
DiD – 1,1-Dioctadecyl-3,3,3,3-tetramethylindodicarbocyanine
DLS – dynamic light scattering
DNA – deoxyribonucleic acid
DOPC – 1,2-dioleoyl-sn-glycero-3-phosphocholine
E1 – excited metastable level
E2 – upper emitting state
Egg-PC – L-α-phosphatidylcholine
EMCCD – electron multiplying charge coupled device
EMCCD – electron multiplying charge coupled device
ESA – excited state absorption
ET – energy transfer
ETU – energy transfer upconversion
FRET – Förster resonance energy transfer
G – ground level
GSA – ground state absorption
HEK - human embryonic kidney
HIV – human immunodeficiency virus
IC-TS – inert core-Tm^{3+} shell
IC-TYS – inert core-Tm^{3+} and Yb^{3+} shell
IDA – ideal dipole approximation
LbL – layer-by-layer assembly
Ln^{3+} – trivalent lanthanide ion
LRET - luminescence resonance energy transfer
MDCK – Madin-Darby canine kidney
MOPS – 3-(N-morpholino)propanesulfonic acid
MRI – magnetic resonance imaging
NIR – near infra-red
PA – photon avalanche

PAA – polyacrylic acid
PEG – polyethylene glycol
PL – phospholipid
PMA – polymethyl acrylate
QC – quantum cutting
QD – quantum dots
RET – resonance energy transfer
SMCC – sulfosuccinimidyl 4-(N-maleimidomethyl)cyclohexane-1-carboxylate
TAMRA - 5-Carboxytetramethylrhodamine
TEM – transmission electron microscopy
TIRF – total internal reflection fluorescence
UC – upconversion
UCL – upconversion luminescence
UCNP – upconverting nanoparticles
UCNP@CMP – customised mussel protein-covered UCNP
UCNP@PL – phospholipid-covered UCNP
XRD – X-ray diffraction

6.2 ***Nomenclature***

k_D^{NR} – rate of non-radiative decay
k_D^R – rate of radiative decay
A_i – experimental coefficient (amplitude of the fit function)
c_0 – starting concentration of the dye
c_d – concentration of the dye in the supernatant
D – diameter of the nanocrystallite
E – efficiency of energy transfer,
E_D – amplitude of the D electric field
$f_D(\lambda)$ – area-normalized fluorescence spectrum of the D
F_i – coefficient by gate width t_{gate} correction ("true amplitude")
f_i – relative fractions of F_i
$I(t)$ – luminescence intensity in dependence on time t
I_{AD} – luminescence intensity of A in the presence of D
I_D – luminescence intensity of D in the absence of A
I_{DA} – luminescence intensity of D in the presence of A
I_{IR} – excitation power.
I_{uc} – UC luminescence intensity
J – overlap integral
k – shape factor of particle morphology
k_{FRET} – FRET rate
k_i – rate constant
k_T – rate of energy transfer
M_d – molar mass of the dye
n – refractive index
N_a – Avogadro constant ($6.02*10^{23}$)
r – distance or radius
R_0 - Förster distance
R_{0max} – maximum Förster distance
R_{0min} – minimum Förster distance
R_A – radius of the sphere of the group of oscillating charges of the A
R_D – radius of the sphere of the group of oscillating charges of the D
t – time
t_{gate} – detection gate width
t_{gate} – gate width
v – sample volume
W_A – energy of the A dipole
y_0 – offset of the fitting function
Δq – full width at half maximum of the diffraction peaks as a function of q
Δt – gate delay
ε – variations of lattice constant of an infinite number of crystallites
ε_A – molar extinction coefficient of the acceptor

ε_D – molar extinction coefficient of the donor
$\eta_{(UCNP)}$ – number of UCNP
θ – Bragg angle of the diffraction peak
θ_A – angle between the A absorption transition moment and the line that connects D and A
θ_D – angle between transition moment of the D emission and the line that connects D and A
θ_T – angle between the D emission transition moment and the A absorption transition moment
κ^2 – dipole orientation factor
λ - wavelength
ν_A – frequency of the acceptor field
ν_D – frequency of the donor field
ρ – density
τ_{av} – average luminescence decay time
τ_D – luminescence lifetime of D in the absence of A
τ_{DA} – luminescence lifetime of D in the presence of A
τ_i – luminescence decay time of the i component
Φ – quantum yield
Φ_A – quantum yield of A
Φ_D – quantum yield of D in the absence of A
Φ_D – quantum yield of the donor fluorescence in the absence of acceptor
Φ_{DA} – quantum yield of D in the presence of A

6.3 ***Supporting information***

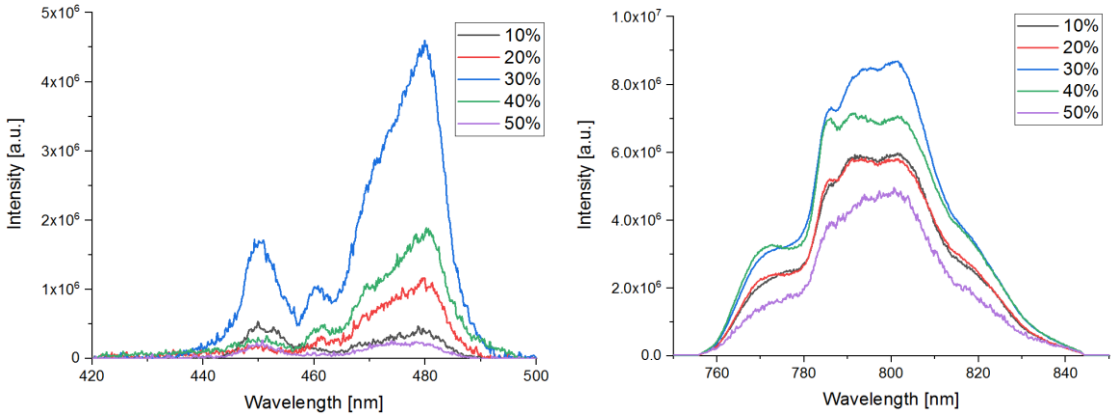

Figure 55. Upconversion emission intensities of $NaYF_4$:Yb^{3+},Tm^{3+},Gd^{3+} (10-50 mol%) UCNP upon pulsed excitation (laser power 66.2 mW) at 976 nm. Blue (B1) and (B2) (left) and near-infrared (NIR) (right) emission bands are shown.

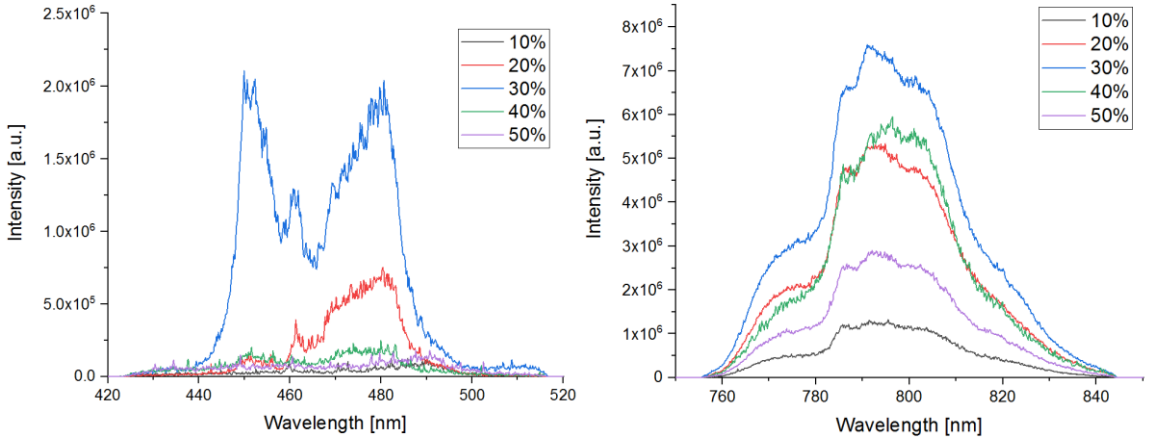

Figure 56. Upconversion emission intensities of 24-month-old $NaYF_4$:Yb^{3+},Tm^{3+},Gd^{3+} (10-50 mol%) UCNP upon excitation at 976 nm upon pulsed excitation (laser power 71.4 mW). Blue (B1) and (B2) (left) and near-infrared (NIR) (right) emission bands are shown.

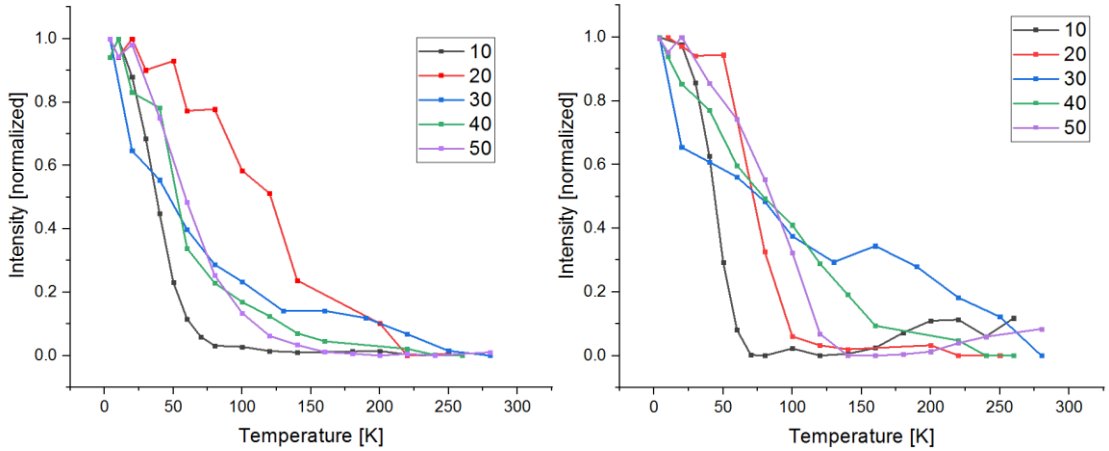

Figure 57. Normalized integrated intensities of blue (B1+B2) (left) and NIR (right) luminescence bands of as-synthesized $NaYF_4$:Yb^{3+},Tm^{3+},Gd^{3+} UCNP (a) 10 mol% Gd^{3+}, (b) 20 mol% Gd^{3+}, (c) 30 mol% Gd^{3+}, (d) 40 mol% Gd^{3+}, (e) 50 mol% Gd^{3+} as a function of temperature. λ_{ex} = 976 nm. Emission spectra were taken every 10 K from 4 to 100 K, and every 20 K from 100 to 280 K. The peaks were integrated within the full width at half maximum range for each measurement point and normalized by the integrated areas for each UCNP species.

7 Bibliography

[1] U. Resch-Genger and H. H. Gorris, “Perspectives and challenges of photon-upconversion nanoparticles - Part I: routes to brighter particles and quantitative spectroscopic studies,” *Anal. Bioanal. Chem.*, vol. 409, no. 25, pp. 5855–5874, 2017.

[2] A. Nadort, J. Zhao, and E. M. Goldys, “Lanthanide upconversion luminescence at the nanoscale: Fundamentals and optical properties,” *Nanoscale*, vol. 8, no. 27. Royal Society of Chemistry, pp. 13099–13130, 2016.

[3] X. Zhu, Q. Su, W. Feng, and F. Li, “Anti-Stokes shift luminescent materials for bio-applications,” *Chem. Soc. Rev.*, vol. 46, no. 4, pp. 1025–1039, 2017.

[4] S. Gai, C. Li, P. Yang, and J. Lin, “Recent progress in rare earth micro/nanocrystals: Soft chemical synthesis, luminescent properties, and biomedical applications,” *Chem. Rev.*, vol. 114, no. 4, pp. 2343–2389, 2014.

[5] H. H. Gorris *et al.*, “Long-wavelength absorbing and fluorescent chameleon labels for proteins, peptides, and amines,” *Bioconjug. Chem.*, vol. 22, no. 7, pp. 1433–1437, 2011.

[6] H. H. Gorris and U. Resch-Genger, “Perspectives and challenges of photon-upconversion nanoparticles - Part II: bioanalytical applications,” *Anal. Bioanal. Chem.*, vol. 409, no. 25, pp. 5875–5890, 2017.

[7] M. Sy, A. Nonat, N. Hildebrandt, and L. J. Charbonnière, “Lanthanide-based luminescence biolabelling,” *Chem. Commun.*, vol. 52, no. 29, pp. 5080–5095, 2016.

[8] A. López de Guereñu, P. Bastian, P. Wessig, L. John, and M. Kumke, “Energy Transfer between Tm-Doped Upconverting Nanoparticles and a Small Organic Dye with Large Stokes Shift,” *Biosensors*, vol. 9, no. 1, p. 9, 2019.

[9] D. T. Klier and M. U. Kumke, “Analysing the effect of the crystal structure on upconversion luminescence in Yb 3+ ,Er 3+ -co-doped NaYF 4 nanomaterials,” *J. Mater. Chem. C*, vol. 3, no. 42, pp. 11228–11238, 2015.

[10] D. Klier and M. U. Kumke, “Upconversion luminescence properties of NaYF4:Yb:Er nanoparticles codoped with Gd3+,” *J. Phys. Chem. C*, vol. 119, no. 6, pp. 3363–3373, 2015.

[11] M. D. Wisser *et al.*, “Enhancing Quantum Yield via Local Symmetry Distortion in Lanthanide-Based Upconverting Nanoparticles,” *ACS Photonics*, vol. 3, no. 8, pp. 1523–1530, 2016.

[12] C. Ma *et al.*, “Optimal Sensitizer Concentration in Single Upconversion Nanocrystals,” *Nano Lett.*, vol. 17, no. 5, pp. 2858–2864, 2017.

[13] B. Zhou, B. Shi, D. Jin, and X. Liu, “Controlling upconversion nanocrystals for emerging applications,” *Nat. Nanotechnol.*, vol. 10, no. 11, pp. 924–936, 2015.

[14] J. Zhao *et al.*, “Upconversion luminescence with tunable lifetime in NaYF4:Yb,Er nanocrystals: Role of nanocrystal size,” *Nanoscale*, vol. 5, no. 3, pp. 944–952, 2013.

[15] J. Shi, F. Tian, J. Lyu, and M. Yang, “Nanoparticle based fluorescence resonance energy transfer (FRET) for biosensing applications,” *J. Mater. Chem. B*, vol. 3, pp. 6989–7005, 2015.

[16] L. Yuan, W. Lin, K. Zheng, and S. Zhu, “FRET-Based Small-Molecule Fluorescent Probes: Rational Design and Bioimaging Applications,” *Acc. Chem. Res.*, vol. 46, no. 7, pp. 1462–1473, 2013.

[17] J. Fan, H. Mingming, Z. Peng, and P. Xiaojun, “Energy transfer cassettes based on organic fluorophores: construction and applications in ratiometric sensing,” *Chem. Soc. Rev.*, vol. 42, pp. 29–43, 2012.

[18] I. H. Stein, C. Steinhauer, and P. Tinnefeld, “Single-Molecule Four-Color FRET Visualizes Energy-Transfer Paths on DNA Origami,” *J. Am. Chem. Soc.*, vol. 133, pp. 4193–4195, 2011.

[19] B. O. Dabbousi *et al.*, “(CdSe)ZnS core-shell quantum dots: Synthesis and characterization of a size series of highly luminescent nanocrystallites,” *J. Phys. Chem. B*, vol. 101, no. 46, pp. 9463–9475, 1997.

[20] M. A. Hines and P. Guyot-Sionnest, “Synthesis and characterization of strongly luminescing ZnS-capped CdSe nanocrystals,” *J. Phys. Chem.*, vol. 100, no. 2, pp. 468–471, 1996.

[21] V. K. A. Sreenivasan, A. V. Zvyagin, and E. M. Goldys, “Luminescent nanoparticles and their applications in the life sciences,” *J. Phys. Condens. Matter*, vol. 25, no. 19, 2013.

[22] F. Wang, D. Banerjee, Y. Liu, X. Chen, and X. Liu, “Upconversion nanoparticles in biological labeling, imaging, and therapy,” *Analyst*, vol. 135, no. 8, pp. 1839–1854, 2010.

[23] V. Biju, “Chemical modifications and bioconjugate reactions of nanomaterials for sensing, imaging, drug delivery and therapy,” *Chem. Soc. Rev.*, vol. 43, no. 3, pp. 744–764, 2014.

[24] A. Gee and X. Xu, “Surface Functionalisation of Upconversion Nanoparticles with Different Moieties for Biomedical Applications,” *Surfaces*, vol. 1, no. 1, pp. 96–121, 2018.

[25] T. Rantanen, M. L. Järvenpää, J. Vuojola, R. Arppe, K. Kuningas, and T. Soukka, “Upconverting phosphors in a dual-parameter LRET-based hybridization assay,” *Analyst*, vol. 134, no. 8, pp. 1713–1716, 2009.

[26] Y. Yuan and Z. Liu, “An effective approach to enhanced energy-transfer efficiency from up-converting phosphors and increased assay sensitivity,” *Chem. Commun.*, vol. 48, no. 60, pp. 7510–7512, 2012.

[27] H. Päkkilä *et al.*, “Quantitative multianalyte microarray immunoassay utilizing upconverting phosphor technology,” *Anal. Chem.*, vol. 84, no. 20, pp. 8628–8634, 2012.

[28] M. V. DaCosta, S. Doughan, Y. Han, and U. J. Krull, “Lanthanide upconversion nanoparticles and applications in bioassays and bioimaging: A review,” *Anal. Chim. Acta*, vol. 832, pp. 1–33, 2014.

[29] L. Xiong, Z. Chen, Q. Tian, T. Cao, C. Xu, and F. Li, “High contrast upconversion luminescence targeted imaging in vivo using peptide-labeled nanophosphors,” *Anal. Chem.*, vol. 81, no. 21, pp. 8687–8694, 2009.

[30] X. F. Yu *et al.*, “Neurotoxin-conjugated upconversion nanoprobes for direct visualization of tumors under near-infrared irradiation,” *Biomaterials*, vol. 31, no. 33, pp. 8724–8731, 2010.

[31] J. C. Zhou, Z. L. Yang, W. Dong, R. J. Tang, L. D. Sun, and C. H. Yan, “Bioimaging and toxicity assessments of near-infrared upconversion luminescent NaYF 4:Yb, Tm nanocrystals,” *Biomaterials*, vol. 32, no. 34, pp. 9059–9067, 2011.

[32] L. Cheng, K. Yang, S. Zhang, M. Shao, S. Lee, and Z. Liu, “Highly-sensitive multiplexed in vivo imaging using pegylated upconversion nanoparticles,” *Nano Res.*, vol. 3, no. 10, pp. 722–732, 2010.

[33] L. Cheng *et al.*, “Multifunctional nanoparticles for upconversion luminescence/MR multimodal imaging and magnetically targeted photothermal therapy,” *Biomaterials*, vol. 33, no. 7, pp. 2215–2222, 2012.

[34] Y. Sun *et al.*, “Fluorine-18 labeled rare-earth nanoparticles for positron emission tomography (PET) imaging of sentinel lymph node,” *Biomaterials*, vol. 32, no. 11, pp. 2999–3007, 2011.

[35] X. Zhu, J. Zhou, M. Chen, M. Shi, W. Feng, and F. Li, “Core-shell Fe 3O 4@NaLuF 4: Yb,Er/Tm nanostructure for MRI, CT and upconversion luminescence tri-modality imaging,” *Biomaterials*, vol. 33, no. 18, pp. 4618–4627, 2012.

[36] T. Zhao, L. Chen, Q. Li, and X. Li, “Near-infrared light triggered drug release from mesoporous silica nanoparticles,” *J. Mater. Chem. B*, vol. 6, no. 44, pp. 7112–7121, 2018.

[37] Q. Liu, Changyou Zhan, and D. S. Kohane, “Phototriggered drug delivery using inorganic nanomaterials,” *Bioconjug Chem.*, vol. 28, no. 1, pp. 98–104, 2017.

[38] L. Zhao *et al.*, “Near-Infrared Photoregulated Drug Release in Living Tumor Tissue via Yolk-Shell Upconversion Nanocages,” *Adv. Funct. Mater.*, vol. 24, no. 3, pp. 363–371, 2014.

[39] A. Gnach, T. Lipinski, A. Bednarkiewicz, J. Rybka, and J. A. Capobianco, “Upconverting nanoparticles: assessing the toxicity,” *Chem. Soc. Rev.*, vol. 44, no. 6, pp. 1561–1584, 2015.

[40] L. Xiong, T. Yang, Y. Yang, C. Xu, and F. Li, “Long-term in vivo biodistribution imaging and toxicity of polyacrylic acid-coated upconversion nanophosphors,” *Biomaterials*, vol. 31, no. 27, pp. 7078–7085, 2010.

[41] J. Zhou and F. Li, “Upconversion nanophosphors for small-animal imaging,” *Chem. Soc. Rev.*, no. 41, pp. 1323–1349, 2012.

[42] C. Piguet, “Extricating erbium,” *Nat. Chem.*, vol. 6, no. 4, pp. 370–370, 2014.

[43] F. Auzel, “Upconversion and Anti-Stokes Processes with f and d Ions in Solids,” *Chem. Rev.*, vol. 104, pp. 139–173, 2004.

[44] J. Zhou, Q. Liu, W. Feng, Y. Sun, and F. Li, “Upconversion luminescent materials: Advances and applications,” *Chem. Rev.*, vol. 115, no. 1, pp. 395–465, 2015.

[45] F. Wang and X. Liu, “Recent advances in the chemistry of lanthanide-doped upconversion nanocrystals,” *Chem. Soc. Rev.*, vol. 38, no. 4, pp. 976–989, 2009.

[46] W. Kaiser and C. G. B. Garrett, “Two-photon excitation in CaF2: Eu2+,” *Phys. Rev. Lett.*, vol. 7, no. 6, pp. 229–231, 1961.

[47] J. F. J. Porter, “Fluorescence Excitation by the Absorption of Two Consecutive Photons,” *Phys. Rev. Lett.*, vol. 7, no. 11, pp. 414–416, 1961.

[48] F. Auzel, “UPCONVERSION PROCESSES IN COUPLED ION SYSTEMS,” *J. Lumin.*, vol. 45, no. 1–6, pp. 341–345, 1990.

[49] F. E. Auzel, “Materials and Devices Using Double-Pumped Phosphors with Energy Transfer,” *Proc. IEEE*, vol. 61, no. 6, pp. 758–786, 1973.

[50] S. Fischer, H. Steinkemper, P. Löper, M. Hermle, and J. C. Goldschmidt, “Modeling upconversion of erbium doped microcrystals based on experimentally determined Einstein coefficients,” *J. Appl. Phys.*, vol. 111, no. 1, 2012.

[51] J. C. G. Bünzli and C. Piguet, “Taking advantage of luminescent lanthanide ions,” *Chem. Soc. Rev.*, vol. 34, no. 12, pp. 1048–1077, 2005.

[52] W. T. Carnall, “The Adsorption and Fluorescence Spectra of Rare Earth Ions in Solution,” in *Handbook on the Physics and Chemistry of Rare Earths*, K. A. J. . Gschneider and L. Eyring, Eds. North-holland Publishing Company, 1979, pp. 171–205.

[53] M. Haase, D. Biner, S. Heer, H. U. Güdel, K. Krämer, and A. Aebischer, “Visible light emission upon near-infrared excitation in a transparent solution of nanocrystalline β-NaGdF4: Yb3+, Er3+,” *Chem. Phys. Lett.*, vol. 407, no. 1–3, pp. 124–128, 2005.

[54] J. F. Suyver, J. Grimm, K. W. Krämer, and H. U. Güdel, “Highly efficient near-infrared to visible up-conversion process in NaYF4:Er3+,Yb3+,” *J. Lumin.*, vol. 114, no. 1, pp. 53–59, 2005.

[55] M. Haase and H. Schäfer, “Upconverting nanoparticles,” *Angew. Chemie - Int. Ed.*, vol. 50, no. 26, pp. 5808–5829, 2011.

[56] A. Aebischer *et al.*, “Structural and spectroscopic characterization of active sites in a family of light-emitting sodium lanthanide tetrafluorides,” *Angew. Chemie - Int. Ed.*, vol. 45, no. 17, pp. 2802–2806, 2006.

[57] K. W. Krämer, D. Biner, G. Frei, H. U. Güdel, M. P. Hehlen, and S. R. Lüthi, “Hexagonal Sodium Yttrium Fluoride Based Green and Blue Emitting Upconversion Phosphors,” *Chem. Mater.*, vol. 16, no. 7, pp. 1244–1251, 2004.

[58] F. Vetrone, J.-C. Boyer, and J. A. Capobianco, “Significance of Yb3+ concentration on the upconversion mechanisms in codoped Y2O3:Er3+, Yb3+ nanocrystals,” *J. Appl. Phys.*, vol. 96, no. 1, pp. 661–667, 2004.

[59] F. Wang *et al.*, “Simultaneous phase and size control of upconversion nanocrystals through lanthanide doping,” *Nature*, vol. 463, no. 7284, pp. 1061–1065, 2010.

[60] D. T. Klier and M. U. Kumke, “ Upconversion NaYF 4 :Yb:Er nanoparticles co-doped with Gd 3+ and Nd 3+ for thermometry on the nanoscale ,” *RSC Adv.*, vol. 5, no. 82, pp. 67149–67156, 2015.

[61] J. Zhang *et al.*, “Monochromatic Near-infrared to near-infrared upconversion nanoparticles for high-contrast fluorescence imaging,” *J. Phys. Chem. C*, vol. 118, no.

5, pp. 2820–2825, 2014.

[62] P. Villanueva-Delgado, K. W. Krämer, R. Valiente, M. De Jong, and A. Meijerink, "Modeling blue to UV upconversion in β-NaYF4:Tm3+," *Phys. Chem. Chem. Phys.*, vol. 18, no. 39, pp. 27396–27404, 2016.

[63] Z. Hua, L. Yujing, L. Yungchen, H. Yu, and D. Xiangfeng, "NIH Public Access," *Nanoscale*, vol. 3, no. 3, pp. 963–966, 2011.

[64] Y. Zhang *et al.*, "Concentration quenching of blue upconversion luminescence in Tm 3+ /Yb 3+ co-doped Gd 2 (WO 4) 3 phosphors under 980 and 808 nm excitation," *J. Alloys Compd.*, vol. 709, pp. 147–157, 2017.

[65] P. Ghosh, J. Oliva, E. De la Rosa, K. K. Haldar, D. Solis, and A. Patra, "Enhancement of Upconversion Emission of LaPO 4 : Er @ Yb Core - Shell Nanoparticles / Nanorods," *J.Phys.Chem.*, vol. 112, pp. 9650–9658, 2008.

[66] L. Prodi, E. Rampazzo, F. Rastrelli, A. Speghini, and N. Zaccheroni, "Imaging agents based on lanthanide doped nanoparticles," *Chem. Soc. Rev.*, vol. 44, pp. 4922–4952, 2015.

[67] X. Chen, D. Peng, Q. Ju, and F. Wang, "Photon upconversion in core-shell nanoparticles," *Chem. Soc. Rev.*, vol. 44, no. 6, pp. 1318–1330, 2015.

[68] Y. F. Wang *et al.*, "Rare-earth nanoparticles with enhanced upconversion emission and suppressed rare-earth-ion leakage," *Chem. - A Eur. J.*, vol. 18, no. 18, pp. 5558–5564, 2012.

[69] Y. Zhong *et al.*, "Elimination of photon quenching by a transition layer to fabricate a quenching-shield sandwich structure for 800 nm excited upconversion luminescence of Nd3+-sensitized nanoparticles," *Adv. Mater.*, vol. 26, no. 18, pp. 2831–2837, 2014.

[70] X. Li *et al.*, "Successive Layer-by-Layer Strategy for Multi-Shell Epitaxial Growth: Shell Thickness and Doping Position Dependence in Upconverting Optical Properties," *Chem. Mater.*, vol. 25, no. 1, pp. 106–112, 2012.

[71] H. Liu *et al.*, "Balancing power density based quantum yield characterization of upconverting nanoparticles for arbitrary excitation intensities," *Nanoscale*, vol. 5, no. 11, p. 4770, 2013.

[72] C. Dong and F. C. J. M. Van Veggel, "Supporting information - Cation Exchange in Lanthanide Fluoride Nanoparticles," *ACS Nano*, vol. 3, no. 1, pp. 8–11, 2009.

[73] N. J. J. Johnson, A. Korinek, C. Dong, and F. C. J. M. Van Veggel, "Self-focusing by Ostwald ripening: A strategy for layer-by-layer epitaxial growth on upconverting nanocrystals," *J. Am. Chem. Soc.*, vol. 134, no. 27, pp. 11068–11071, 2012.

[74] X. Xu *et al.*, "Optimising passivation shell thickness of single upconversion nanoparticles using a time-resolved spectrometer," *APL Photonics*, vol. 4, no. 026104, pp. 1–8, 2019.

[75] S. Fischer, N. D. Bronstein, J. K. Swabeck, E. M. Chan, and A. P. Alivisatos, "Precise Tuning of Surface Quenching for Luminescence Enhancement in Core-Shell Lanthanide-Doped Nanocrystals," *Nano Lett.*, vol. 16, no. 11, pp. 7241–7247, 2016.

[76] C. Wurth, S. Fischer, B. Grauel, A. P. Alivisatos, and U. Resch-Genger, "Quantum

Yields, Surface Quenching, and Passivation E ffi ciency for Ultrasmall Core/Shell Upconverting Nanoparticles," *J. Am. Chem. Soc.*, vol. 140, pp. 4922–4928, 2018.

[77] P.-C. Cheng, "The Contrast Formation in Optical Microscopy," in *Handbook Of Biological Confocal Microscopy (3rd ed.)*, 2006, pp. 162–206.

[78] I. Medintz and N. Hildebrandt, "FRET – Förster Resonance Energy Transfer, From Theory to Applications.," in *Wiley-VCH, Weinheim, Germany*, 2014, p. ch. 5, pp. 105–164.

[79] R. M. Clegg, *Reviews in Fluorescence 2005*, vol. 3. Springer Science Business Media Inc, 2006.

[80] D. L. Dexter, "A Theory of Sensitized Luminescence in Solids," *J. Chem. Phys.*, vol. 21, no. 5, pp. 836–850, 1953.

[81] D. L. Andrews and A. A. Demidov, *Resonance Energy Transfer*. Wiley, 1999.

[82] E. W. Weisstein, "Electric Multipole Expansion -- from Eric Weisstein's World of Physics." .

[83] T. Förster, *Fluoreszenz Organischer Verbindunger*. Vandenhoeck & Ruprecht, 1951.

[84] G. Chen, H. Qiu, P. N. Prasad, and X. Chen, "Upconversion Nanoparticles : Design , Nanochemistry , and Applications in Theranostics," *Chem. Rev.*, vol. 114, pp. 5161–5214, 2014.

[85] A. Sedlmeier and H. H. Gorris, "Surface modification and characterization of photon-upconverting nanoparticles for bioanalytical applications," *Chem. Soc. Rev.*, vol. 44, no. 6, pp. 1526–1560, 2015.

[86] L. Y. Ang, M. E. Lim, L. C. Ong, and Y. Zhang, "Applications of upconversion nanoparticles in imaging, detection and therapy," *Nanomedicine*, vol. 6, no. 7, pp. 1273–1288, 2011.

[87] R. Naccache, F. Vetrone, V. Mahalingam, L. A. Cuccia, and J. A. Capobianco, "Controlled synthesis and water dispersibility of hexagonal phase NaGdF4: Ho 3+/Yb 3+ nanoparticles," *Chem. Mater.*, vol. 21, no. 4, pp. 717–723, 2009.

[88] S. Wilhelm *et al.*, "Water dispersible upconverting nanoparticles: Effects of surface modification on their luminescence and colloidal stability," *Nanoscale*, vol. 7, no. 4, pp. 1403–1410, 2015.

[89] R. A. Sperling and W. J. Parak, "Surface modification, functionalization and bioconjugation of colloidal inorganic nanoparticles," *Philos. Trans. R. Soc. A Math. Phys. Eng. Sci.*, vol. 368, no. 1915, pp. 1333–1383, 2010.

[90] S. Wilhelm *et al.*, "Water dispersible upconverting nanoparticles: effects of surface modification on their luminescence and colloidal stability," *Nanoscale*, vol. 7, pp. 1403–1410, 2015.

[91] S. Jiang, K. Y. Win, S. Liu, C. P. Teng, Y. Zheng, and M. Y. Han, "Surface-functionalized nanoparticles for biosensing and imaging-guided therapeutics," *Nanoscale*, vol. 5, no. 8, pp. 3127–3148, 2013.

[92] Y. Cen, Y. M. Wu, X. J. Kong, S. Wu, R. Q. Yu, and X. Chu, "Phospholipid-modified upconversion nanoprobe for ratiometric fluorescence detection and imaging of

phospholipase D in cell lysate and in living cells," *Anal. Chem.*, vol. 86, no. 14, pp. 7119–7127, 2014.

[93] D. Wang, A. L. Rogach, and F. Caruso, "Semiconductor Quantum Dot-Labeled Microsphere Bioconjugates Prepared by Stepwise Self-Assembly," *Nano Lett.*, vol. 2, no. 8, pp. 857–861, 2002.

[94] G. Decher, "Fuzzy nanoassemblies: Toward layered polymeric multicomposites," *Science (80-.).*, vol. 277, no. 5330, pp. 1232–1237, 1997.

[95] M. Wang, G. Abbineni, A. Clevenger, C. Mao, and S. Xu, *Upconversion Nanoparticles: Synthesis, Surface Modification, and Biological Applications*, vol. 7, no. 6. 2011.

[96] J. M. Goddard and D. Erickson, "Bioconjugation techniques for microfluidic biosensors," *Anal Bioanal Chem*, vol. 394, no. 2, pp. 469–479, 2009.

[97] Z. Li and Y. Zhang, "Monodisperse silica-coated polyvinyl-pyrrolidone/NaYF4 nanocrystals with multicolor upconversion fluorescence emission," *Angew. Chemie - Int. Ed.*, vol. 45, no. 46, pp. 7732–7735, 2006.

[98] S. Sivakumar, P. R. Diamente, and F. C. J. M. Van Veggel, "Silica-coated Ln3+-doped LaF3 nanoparticles as robust down- And upconverting biolabels," *Chem. - A Eur. J.*, vol. 12, no. 22, pp. 5878–5884, 2006.

[99] N. Bogdan, F. Vetrone, G. A. Ozin, and J. A. Capobianco, "Synthesis of ligand-free colloidally stable water dispersible brightly luminescent lanthanide-doped upconverting nanoparticles," *Nano Lett.*, vol. 11, no. 2, pp. 835–840, 2011.

[100] K. E. Sapsford *et al.*, "Functionalizing nanoparticles with biological molecules: Developing chemistries that facilitate nanotechnology," *Chem. Rev.*, vol. 113, no. 3, pp. 1904–2074, 2013.

[101] Z. Chen *et al.*, "Versatile synthesis strategy for carboxylic acid-functionalized upconverting nanophosphors as biological labels," *J. Am. Chem. Soc.*, vol. 130, no. 10, pp. 3023–3029, 2008.

[102] P. Wang and P. Zhang, "Ligase-assisted, upconversion luminescence resonance energy transfer-based method for specific and sensitive detection of V600E mutation in the BRAF gene," *RSC Adv.*, vol. 4, no. 99, pp. 56235–56240, 2014.

[103] M. Kumar and P. Zhang, "Highly Sensitive and Selective Label-Free Optical Detection of Mercuric Ions Using Photon Upconverting Nanoparticles," vol. 25, no. 11, pp. 2431–2435, 2010.

[104] M. Kumar and P. Zhang, "Highly sensitive and selective label-free optical detection of DNA hybridization based on photon upconverting nanoparticles," *Langmuir*, vol. 25, no. 11, pp. 6024–6027, 2009.

[105] S. Cui *et al.*, "Amphiphilic chitosan modified upconversion nanoparticles for in vivo photodynamic therapy induced by near-infrared light," *J. Mater. Chem.*, vol. 22, no. 11, pp. 4861–4873, 2012.

[106] L. Q. Xiong, Z. G. Chen, M. X. Yu, F. Y. Li, C. Liu, and C. H. Huang, "Synthesis, characterization, and in vivo targeted imaging of amine-functionalized rare-earth up-converting nanophosphors," *Biomaterials*, vol. 30, no. 29, pp. 5592–5600, 2009.

[107] L. Wang *et al.*, “Fluorescence resonant energy transfer biosensor based on upconversion-luminescent nanoparticles,” *Angew. Chemie - Int. Ed.*, vol. 44, no. 37, pp. 6054–6057, 2005.

[108] L. Wang and Y. Li, “Green upconversion nanocrystals for DNA detection,” *Chem. Commun.*, no. 24, pp. 2557–2559, 2006.

[109] N. Duan *et al.*, “Dual-color upconversion fluorescence and aptamer-functionalized magnetic nanoparticles-based bioassay for the simultaneous detection of Salmonella Typhimurium and Staphylococcus aureus,” *Anal. Chim. Acta*, vol. 723, pp. 1–6, 2012.

[110] Y. H. Chien *et al.*, “Near-infrared light photocontrolled targeting, bioimaging, and chemotherapy with caged upconversion nanoparticles in vitro and in vivo,” *ACS Nano*, vol. 7, no. 10, pp. 8516–8528, 2013.

[111] H. C. Kolb, M. G. Finn, and K. B. Sharpless, “Click Chemistry: Diverse Chemical Function from a Few Good Reactions,” *Angew. Chemie - Int. Ed.*, vol. 40, no. 11, pp. 2004–2021, 2001.

[112] J. M. Baskin *et al.*, “Copper-free click chemistry for dynamic in vivo imaging,” *PNAS*, vol. 104, no. 43, pp. 16793–16797, 2007.

[113] J. C. Jewett and C. R. Bertozzi, “Cu-free click cycloaddition reactions in chemical biology,” *Chem Soc Rev.*, vol. 39, no. 4, pp. 1272–1279, 2010.

[114] G. H. Hur *et al.*, “Crosslinking Studies of Protein-Protein Interactions in Nonribosomal Peptide Biosynthesis,” *Chem. Biol.*, vol. 16, no. 4, pp. 372–381, 2009.

[115] M. A. Nessen *et al.*, “Selective enrichment of azide-containing peptides from complex mixtures,” *J. Proteome Res.*, vol. 8, no. 7, pp. 3702–3711, 2009.

[116] A. B. Neef and C. Schultz, “Selective fluorescence labeling of lipids in living cells,” *Angew. Chemie - Int. Ed.*, vol. 48, no. 8, pp. 1498–1500, 2009.

[117] W. M. Hoskins and R. Craig, “Uses of Bioassay in Entomology,” *Annu. Rev. Entomol.*, vol. 7, no. 1, pp. 437–464, 1962.

[118] L. Mattsson, K. D. Wegner, N. Hildebrandt, and T. Soukka, “Upconverting nanoparticle to quantum dot FRET for homogeneous double-nano biosensors,” *RSC Adv.*, vol. 5, pp. 13270–13277, 2015.

[119] F. Van De Rijke *et al.*, “Up-converting phosphor reporters for nucleic acid microarrays,” *Nat. Biotechnol.*, vol. 19, no. 3, pp. 273–276, 2001.

[120] S. Wu *et al.*, “Simultaneous detection of enterovirus 71 and coxsackievirus A16 using dual-colour upconversion luminescent nanoparticles as labels,” *Chem. Commun.*, vol. 48, no. 40, pp. 4866–4868, 2012.

[121] Y. Wang, L. Bao, Z. Liu, and D. W. Pang, “Aptamer biosensor based on fluorescence resonance energy transfer from upconverting phosphors to carbon nanoparticles for thrombin detection in human plasma,” *Anal. Chem.*, vol. 83, no. 21, pp. 8130–8137, 2011.

[122] R. S. Niedbala *et al.*, “Detection of analytes by immunoassay using Up-Converting Phosphor Technology,” *Anal. Biochem.*, vol. 293, no. 1, pp. 22–30, 2001.

[123] K. Kuningas *et al.*, “Upconversion fluorescence resonance energy transfer in a

homogeneous immunoassay for estradiol," *Anal. Chem.*, vol. 78, no. 13, pp. 4690–4696, 2006.

[124] L. Wang and Y. Li, "Luminescent nanocrystals for nonenzymatic glucose concentration determination," *Chem. - A Eur. J.*, vol. 13, no. 15, pp. 4203–4207, 2007.

[125] C. Zhang, Y. Yuan, S. Zhang, Y. Wang, and Z. Liu, "Biosensing platform based on fluorescence resonance energy transfer from upconverting nanocrystals to graphene oxide," *Angew. Chemie - Int. Ed.*, vol. 50, no. 30, pp. 6851–6854, 2011.

[126] S. Wu, N. Duan, Z. Wang, and H. Wang, "Aptamer-functionalized magnetic nanoparticle-based bioassay for the detection of ochratoxin A using upconversion nanoparticles as labels," *Analyst*, vol. 136, no. 11, pp. 2306–2314, 2011.

[127] O. Barbier, L. Arreola-Mendoza, and L. M. Del Razo, "Molecular mechanisms of fluoride toxicity," *Chem. Biol. Interact.*, vol. 188, no. 2, pp. 319–333, 2010.

[128] M. A. Perazella, "Current status of gadolinium toxicity in patients with kidney disease," *Clin. J. Am. Soc. Nephrol.*, vol. 4, no. 2, pp. 461–469, 2009.

[129] X. Liu *et al.*, "Probing the nature of upconversion nanocrystals: Instrumentation matters," *Chem. Soc. Rev.*, vol. 44, no. 6, pp. 1479–1508, 2015.

[130] O. Plohl *et al.*, "Optically detected degradation of NaYF4:Yb,Tm-based upconversion nanoparticles in phosphate buffered saline solution," *Langmuir*, vol. 33, no. 2, pp. 553–560, 2017.

[131] D. Lisjak, O. Plohl, J. Vidmar, B. Majaron, and M. Ponikvar-Svet, "Dissolution Mechanism of Upconverting AYF4:Yb,Tm (A = Na or K) Nanoparticles in Aqueous Media," *Langmuir*, vol. 32, no. 32, pp. 8222–8229, 2016.

[132] R. Abdul Jalil and Y. Zhang, "Biocompatibility of silica coated NaYF4 upconversion fluorescent nanocrystals," *Biomaterials*, vol. 29, no. 30, pp. 4122–4128, 2008.

[133] M. Yu *et al.*, "Laser scanning up-conversion luminescence microscopy for imaging cells labeled with rare-earth nanophosphors," *Anal. Chem.*, vol. 81, no. 3, pp. 930–935, 2009.

[134] P. Rodríguez-Sevilla *et al.*, "Thermal Scanning at the Cellular Level by an Optically Trapped Upconverting Fluorescent Particle," *Adv. Mater.*, vol. 28, no. 12, pp. 2421–2426, 2016.

[135] P. Rodríguez-Sevilla *et al.*, "Assessing Single Upconverting Nanoparticle Luminescence by Optical Tweezers," *Nano Lett.*, vol. 15, no. 8, pp. 5068–5074, 2015.

[136] J. Jin *et al.*, "Polymer-coated NaYF4:Yb3+, Er3+ upconversion nanoparticles for charge-dependent cellular imaging," *ACS Nano*, vol. 5, no. 10, pp. 7838–7847, 2011.

[137] J. Peng *et al.*, "Polyphosphoric acid capping radioactive/upconverting NaLuF4: Yb,Tm,153Sm nanoparticles for blood pool imaging invivo," *Biomaterials*, vol. 34, no. 37, pp. 9535–9544, 2013.

[138] S. Wang, A. Bi, W. Zeng, and Z. Cheng, "Upconversion nanocomposites for photo-based cancer theranostics," *J. Mater. Chem. B*, vol. 4, no. 32, pp. 5331–5348, 2016.

[139] Y. N. Konan, R. Gurny, and E. Allémann, "State of the art in the delivery of photosensitizers for photodynamic therapy," *J. Photochem. Photobiol. B Biol.*, vol. 66,

no. 2, pp. 89–106, 2002.

[140] Q. Liu, W. Feng, and F. Li, “Water-soluble lanthanide upconversion nanophosphors : Synthesis and bioimaging applications in vivo,” *Coord. Chem. Rev.*, vol. 273–274, pp. 100–110, 2014.

[141] H. I. Yoon *et al.*, “Bioorthogonal Copper Free Click Chemistry for Labeling and Tracking of Chondrocytes In Vivo,” *Bioconjug. Chem.*, vol. 27, no. 4, pp. 927–936, 2016.

[142] J. M. Eeftens, J. van der Torre, D. R. Burnham, and C. Dekker, “Copper-free click chemistry for attachment of biomolecules in magnetic tweezers,” *BMC Biophys.*, vol. 8, no. 1, pp. 1–7, 2015.

[143] W. Hou *et al.*, “Real-time analysis of quantum dot labeled single porcine epidemic diarrhea virus moving along the microtubules using single particle tracking,” *Sci. Rep.*, vol. 9, no. 1, pp. 1–10, 2019.

[144] A. Geßner, “Lanthanoid-dotierte mikro- und mesoporöse Feststoffe Charakterisierung von Ion-Wirt-Wechselwirkungen, Speziesverteilung und Lumineszenzeigenschaften mittels eitaufgelöster Lumineszenzspektroskopie.,” University of Potsdam, 2010.

[145] L. E. Mackenzie, J. A. Goode, A. Vakurov, P. P. Nampi, G. Jose, and P. A. Millner, “The theoretical molecular weight of NaYF 4 : RE upconversion nanoparticles,” *Sci. Rep.*, vol. 8, pp. 1106–1114, 2018.

[146] J. Zhang, C. Mi, H. Wu, H. Huang, C. Mao, and S. Xu, “Synthesis of NaYF4:Yb/Er/Gd up-conversion luminescent nanoparticles and luminescence resonance energy transferbased protein detection,” *Anal Biochem.*, vol. 83, no. 2, pp. 1–29, 2012.

[147] A. D. Ostrowski *et al.*, “Controlled synthesis and single-particle imaging of bright, sub-10 nm lanthanide-doped upconverting nanocrystals,” *ACS Nano*, vol. 6, no. 3, pp. 2686–2692, 2012.

[148] D. Lisjak, O. Plohl, M. Ponikvar-Svet, and B. Majaron, “Dissolution of upconverting fluoride nanoparticles in aqueous suspensions,” *RSC Adv.*, vol. 5, no. 35, pp. 27393–27397, 2015.

[149] S. Lahtinen *et al.*, “Disintegration of hexagonal NaYF4:Yb3+,Er3+ upconverting nanoparticles in aqueous media: The role of fluoride in solubility equilibrium,” *J. Phys. Chem. C*, vol. 121, no. 1, pp. 656–665, 2017.

[150] F. Chen *et al.*, “Positive and negative lattice shielding effects Co-existing in Gd (III) ion doped bifunctional upconversion nanoprobes,” *Adv. Funct. Mater.*, vol. 21, no. 22, pp. 4285–4294, 2011.

[151] W. Xie *et al.*, “Tunable phase and upconverting luminescence of Gd 3+ co-doped NaErF 4 :Yb 3+ nanostructures,” *Mater. Res. Bull.*, vol. 95, no. November, pp. 509–514, 2017.

[152] G. Chen, H. Ågren, T. Y. Ohulchanskyy, and P. N. Prasad, “Light upconverting core-shell nanostructures: Nanophotonic control for emerging applications,” *Chem. Soc. Rev.*, vol. 44, no. 6, pp. 1680–1713, 2015.

[153] L. Li, N. Zhao, L. Fu, J. Zhou, X. Ai, and J. Zhang, “Temperature modulation of

concentration quenching in lanthanide-doped nanoparticles for enhanced upconversion luminescence," *Nano Res.*, vol. 11, no. 4, pp. 2104–2115, 2018.

[154] C. T. Xu *et al.*, "Upconverting nanoparticles for pre-clinical diffuse optical imaging, microscopy and sensing: Current trends and future challenges," *Laser Photonics Rev.*, vol. 7, no. 5, pp. 663–697, 2013.

[155] L. H. Fischer, G. S. Harms, and O. S. Wolfbeis, "Upconverting nanoparticles for nanoscale thermometry," *Angew. Chemie - Int. Ed.*, vol. 50, no. 20, pp. 4546–4551, 2011.

[156] W. T. Carnall, P. R. Fields, and B. G. Wybourne, "Spectral intensities of the trivalent lanthanides and actinides in solution. I. Pr3+, Nd3+, Er3+, Tm3+, and Yb8+ 1," *J. Chem. Phys.*, vol. 42, no. 11, pp. 3797–3806, 1965.

[157] T. V. Gavrilović, D. J. Jovanović, V. Lojpur, and M. D. Dramićanin, "Multifunctional Eu3+- and Er3+/Yb3+-doped GdVO4 nanoparticles synthesized by reverse micelle method," *Sci. Rep.*, vol. 4, pp. 1–9, 2014.

[158] J. Hesse *et al.*, "Rapid Synthesis of Sub-10 nm Hexagonal NaYF4-Based Upconverting Nanoparticles using Therminol® 66," *ChemistryOpen*, vol. 7, no. 2, pp. 159–168, 2018.

[159] S. Asokan *et al.*, "The use of heat transfer fluids in the synthesis of high-quality CdSe quantum dots, core/shell quantum dots, and quantum rods," *Nanotechnology*, vol. 16, no. 10, pp. 2000–2011, 2005.

[160] W. Y. Lynn Ko, H. G. Bagaria, S. Asokan, K. J. Lin, and M. S. Wong, "CdSe tetrapod synthesis using cetyltrimethylammonium bromide and heat transfer fluids," *J. Mater. Chem.*, vol. 20, no. 12, pp. 2474–2478, 2010.

[161] H. Mai *et al.*, "High-Quality Sodium Rare-Earth Fluoride Nanocrystals : Controlled Synthesis and Optical Properties," *J. Amer. Chem. Soc.*, vol. 128, pp. 6426–6436, 2006.

[162] J. Boyer and F. C. J. M. Van Veggel, "Absolute quantum yield measurements of colloidal NaYF 4 : Er 3 + , Yb 3 + upconverting nanoparticles †," *Nanoscale*, vol. 2, pp. 1417–1419, 2010.

[163] M. S. Mejer *et al.*, "Absolute upconversion quantum yields of blue-emitting LiYF4 :Yb3+ ,Tm3+ upconverting nanoparticles †," *Phys. Chem. Chem. Phys*, vol. 20, pp. 22556–22562, 2018.

[164] R. Heim and R. Y. Tsien, "Engineering green fluorescent protein for improved brightness , longer wavelengths and fluorescence resonance energy transfer," *Curr. Biol.*, vol. 6, pp. 178–182, 1995.

[165] W. Zheng, P. Huang, D. Tu, E. Ma, H. Zhu, and X. Chen, "Lanthanide-doped upconversion nano-bioprobes: electronic structures, optical properties, and biodetection," *Chem. Soc. Rev.*, vol. 44, no. 6, 2015.

[166] Y. Wang *et al.*, "Critical Shell Thickness of Core/Shell Upconversion Luminescence," *J. Phys. Chem. Lett.*, vol. 2, pp. 2083–2088, 2011.

[167] S. Lahtinen, Q. Wang, and T. Soukka, "Long-Lifetime Luminescent Europium(III) Complex as an Acceptor in an Upconversion Resonance Energy Transfer Based

Homogeneous Assay," *Anal. Chem.*, vol. 88, pp. 653–658, 2016.

[168] V. Muhr *et al.*, "Particle-Size-Dependent Fo¨rster Resonance Energy Transfer from Upconversion Nanoparticles to Organic Dyes," *Anal. Chem.*, vol. 89, pp. 4868–4874, 2017.

[169] S. Bhuckory, E. Hemmer, Y.-T. Wu, A. Yahia-Ammar, F. Vetrone, and N. Hildebrandt, "Core or shell? Er3+ FRET donors in upconversion nanoparticles," *Eur. J. Inorg. Chem.*, no. 1, pp. 5186–5195, 2017.

[170] O. Dukhno, F. Przybilla, M. Collot, A. Klymchenko, and Y. Mély, "Nanoscale Quantitative assessment of energy transfer in upconverting nanoparticles grafted with organic dyes," *Nanoscale*, vol. 9, pp. 11994–12004, 2017.

[171] P. Wessig, R. Wawrzinek, K. Möllnitz, E. Feldbusch, and U. Schilde, "A new class of fluorescent dyes based on 1 , 3-benzodioxole and [1 , 3] -dioxolo [4 . 5- f] benzodioxole," *Tetrahedron Lett.*, vol. 52, no. 46, pp. 6192–6195, 2011.

[172] R. Wawrzinek *et al.*, "Bioorganic & Medicinal Chemistry Letters DBD dyes as fluorescent probes for sensing lipophilic environments b a r t i c l e i n f o OH a i s i," *Bioorg. Med. Chem. Lett.*, vol. 22, no. 17, pp. 5367–5371, 2012.

[173] R. Wawrzinek *et al.*, "DBD Dyes as Fluorescence Lifetime Probes to Study Conformational Changes in Proteins," *Chem. Eur. J.*, vol. 19, pp. 17349–17357, 2013.

[174] A. Bednarkiewicz, M. Nyk, M. Samoc, and W. Strek, "Up-conversion FRET from Er 3 + / Yb 3 + : NaYF 4 Nanophosphor to CdSe Quantum Dots," *J.Phys.Chem.*, vol. 114, pp. 17535–17541, 2010.

[175] M. Kaiser, C. Würth, M. Kraft, I. Hyppänen, T. Soukka, and U. Resch-Genger, "Power-dependent upconversion quantum yield of NaYF4:Yb3+,Er3+ nano- and micrometer-sized particles – measurements and simulations," *Nanoscale*, vol. 9, pp. 10051–10058, 2017.

[176] L. M. Jin, X. Chen, C. K. Siu, F. Wang, and S. F. Yu, "Enhancing Multiphoton Upconversion from NaYF4:Yb/Tm@NaYF4 Core−Shell Nanoparticles via the Use of Laser Cavity," *ASC Nano*, vol. 11, pp. 843–849, 2017.

[177] R. Arppe *et al.*, "Quenching of the upconversion luminescence of NaYF4:Yb3+,Er3+ and NaYF4:Yb3+,Tm3+ nanophosphors by water: the role of the sensitizer Yb3+ in non-radiative relaxation," *Nanoscale*, vol. 7, pp. 11746–11757, 2015.

[178] Y. Liu, D. Tu, H. Zhu, and X. Chen, "Lanthanide-doped luminescent nanoprobes: Controlled synthesis, optical spectroscopy, and bioapplications," *Chem. Soc. Rev.*, vol. 42, no. 16, pp. 6924–6958, 2013.

[179] M. Buchner *et al.*, "Photosensitiser functionalised luminescent upconverting nanoparticles for efficient photodynamic therapy of breast cancer cells," *Photochem. Photobiol. Sci.*, vol. 18, no. 1, pp. 98–109, 2019.

[180] E. Andresen, U. Resch-Genger, and M. Schäferling, "Surface Modifications for Photon-Upconversion-Based Energy-Transfer Nanoprobes," *Langmuir*, vol. 35, no. 15, pp. 5093–5113, 2019.

[181] E. Hemmer, T. Yamano, H. Kishimoto, N. Venkatachalam, H. Hyodo, and K. Soga, "Cytotoxic aspects of gadolinium oxide nanostructures for up-conversion and NIR

bioimaging," *Acta Biomater.*, vol. 9, no. 1, pp. 4734–4743, 2013.

[182] L. Yu *et al.*, "Bioinspired Universal Monolayer Coatings by Combining Concepts from Blood Protein Adsorption and Mussel Adhesion," *ACS Appl. Mater. Interfaces*, vol. 9, no. 7, pp. 6624–6633, 2017.

[183] P. S. Peijzel, W. J. M. Schrama, and A. Meijerink, "Thulium as a sensitizer for the Gd3+/Eu3+ quantum cutting couple," *Mol. Phys.*, vol. 102, no. 11-12 SPEC. ISS., pp. 1285–1290, 2004.

[184] H. Lin *et al.*, "Down-Conversion From Blue to Near Infrared in Tm3+ – Yb3+ Codoped YPOQ Transparent Ceramics," *IEEE Photonics Technol. Lett.*, vol. 22, no. 12, pp. 866–868, 2010.

[185] Z. Pan, R. Akrobetu, and S. H. Morgan, " Spectrum upconversion and downconversion in (Tm 3+ ,Yb 3+) and (Tb 3+ ,Yb 3+) co-doped fluorosilicate glass ," *Next Gener. Photonic Cell Technol. Sol. Energy Convers. IV*, vol. 8824, p. 88240Z, 2013.

[186] J. Liu, E. Quinteiro González, A. M. Kaczmarek, and R. Van Deun, "Dual-mode upconversion and downshifting white-light emitting Ln3+:Gd2W2O9 materials," *New J. Chem.*, vol. 42, no. 4, pp. 2393–2400, 2018.

[187] O. Maalej, J. Merigeon, B. Boulard, and M. Girtan, "Visible to near-infrared down-shifting in Tm3+ doped fluoride glasses for solar cells efficiency enhancement," *Opt. Mater. (Amst).*, vol. 60, pp. 235–239, 2016.

[188] C. Cao, Q. Liu, M. Shi, W. Feng, and F. Li, "Lanthanide-Doped Nanoparticles with Upconversion and Downshifting Near-Infrared Luminescence for Bioimaging," *Inorg. Chem.*, vol. 58, no. 14, pp. 9351–9357, 2019.

[189] H. He *et al.*, "Bispecific Antibody-Functionalized Upconversion Nanoprobe," *Anal. Chem.*, vol. 90, no. 5, pp. 3024–3029, 2018.

[190] H. L. Jo *et al.*, "Fast and background-free three-dimensional (3D) live-cell imaging with lanthanide-doped upconverting nanoparticles," *Nanoscale*, vol. 7, no. 46, pp. 19397–19402, 2015.

[191] S. Hu *et al.*, "Upconversion NaYF4 nanoparticles for size dependent cell imaging and concentration dependent detection of rhodamine B," *J. Nanomater.*, vol. 2015, 2015.

[192] Y. Shi *et al.*, "Stable Upconversion Nanohybrid Particles for Specific Prostate Cancer Cell Immunodetection," *Sci. Rep.*, vol. 6, no. November, pp. 1–11, 2016.

[193] A. Hlaváček *et al.*, "Competitive Upconversion-Linked Immunosorbent Assay for the Sensitive Detection of Diclofenac," *Anal. Chem.*, vol. 88, no. 11, pp. 6011–6017, 2016.

[194] F. Wang *et al.*, "Microscopic inspection and tracking of single upconversion nanoparticles in living cells," *Light Sci. Appl.*, vol. 7, no. 4, pp. 18006–18007, 2018.

[195] G. Yang *et al.*, "Application of a double-colour upconversion nanofluorescent probe for targeted imaging of mantle cell lymphoma," *Oncotarget*, vol. 9, no. 24, pp. 16758–16774, 2018.

8 Publications, Communications and Awards

Publications:

A. López de Guereñu, P. Bastian, P. Wessig, L.John, M. U. Kumke, Energy Transfer between Tm-Doped Upconverting Nanoparticles and a Small Organic Dye with Large Stokes Shift. Biosensors 2019, 9, 9; doi:10.3390/bios9010009

S. Schimka, D. T. Klier, A. López de Guereñu, P. Bastian, N. Lomadze, M. U. Kumke, S. Santer. Photo-isomerization of azobenzene containing surfactants induced by near-infrared light using upconversion nanoparticles as mediator. J. Phys.: Condens. Matter 31 (2019) 125201 (9pp); doi: 10.1088/1361-648X/aafcfa

Oral communications:

Bunsentagung 2019 - 118th General Assembly of the German Bunsen Society for Physical Chemistry. *Evaluation of the Resonance Energy Transfer between Tm^{3+} - doped Upconverting Nanoparticles (UCNP) and Organic Dyes.* Jena, Germany. 30 May – 1 June 2019.

Poster communications:

2nd Conference and Spring School on Properties, Design and Applications of Upconversion Nanomaterials. *Yb^{3+}, Tm^{3+} - based upconverting nanoparticles (UCNP) for bioimaging.* Valencia, Spain. 2 - 6 April 2018.

Bunsentagung 2015 - 114th General Assembly of the German Bunsen Society for Physical Chemistry. *Luminescence upconversion nanoparticles for biosensing: synthesis, characterization and application.* Bochum, Germany. 14-16 May 2015.

Scholarships and fellowships:

Fellowship from School of Analytical Sciences Adlershof (SALSA), Humboldt University, 2014 – 2017

PhD completion Scholarship from the University of Potsdam Graduate School, 2020

9 Acknowledgement

I would like to thank my supervisor Prof. Dr. Michael U. Kumke for providing me with constant support, encouragement, patience and valuable advice, for allowing a great degree of freedom to pursue my own scientific interests, for giving me an opportunity to be a part of interesting and challenging scientific projects, and to take on more responsibility along the way. I can not imagine a better "scientific father" and for that I am extremely grateful.

I want to thank Prof. Dr. Hans-Gerd Löhmannsröben for giving me the opportunity to work in his group, and for creating a unique, friendly and playful atmosphere which made working here a great pleasure. Excellent technical equipment, many colleagues with different scientific backgrounds, and an environment of complete respect, support, and acceptance, created unmatched working conditions.

To Prof. Dr. Salvatore Chiantia and his group for his supervision and attention in the final part of my thesis, for giving me the opportunity to broaden my research fields and for always being there to help and answer my questions. To Prof. Dr. Andreas Herrmann, for his supervision, continuous collaboration and exchange of ideas, and for providing the necessary information and means to start the biological investigations.

I would also like to thank my colleagues from University of Potsdam, for the friendly and cheerful environment that made it a pleasure to come to work every day, for always making me feel welcome and accepted, for helping me in so many ways, and for introducing me to new ways of seeing things both in science and life. Especially Dennis T. Klier, for being so patient and supportive during my first steps in the group and for teaching me so many things about the subject, and to Philipp U. Bastian, for helping me with the spectroscopy and being a great friend and office mate.

Thank you to Dr. C. Günter for helping with the XRD measurements, to the group of Prof. Wessig for the collaboration on the energy transfer project, to Marcus Mildner and Petra Schrade for helping with the TEM measurements, to the group of Prof. Dr. Santer for our azide-UCNP collaboration, and probably many more people who contributed along the way and made this thesis possible.

I would like to thank SALSA for their financial and overall support throughout all those years, and to BAM, PoGS, and University of Potsdam for supporting parts of this research financially.

My family and friends contributed by keeping my life in balance and supporting me through some rougher patches, without them this wouldn't be possible either.

Declaration

Hiermit versichere ich, dass ich die hier vorgelegte Dissertation selbstst¨andig verfasst und keine anderen als die angegebenen Quellen und Hilfsmittel verwendet habe.

Ich versichere, dass diese Arbeit noch nicht an anderer Stelle zur Erlangung des Doktorgrades eingereicht worden ist.

Potsdam, April 2020

(Anna López de Guereñu)